Master of Science Thesis

Force Generation of Bio-Inspired Hover Kinematics

An experimental campaign

Ruben Vandenheede

June 18, 2012

Faculty of Aerospace Engineering · Delft University of Technology

Aerodynamics

TU Delft

Force Generation of Bio-Inspired Hover Kinematics

An experimental campaign

Master of Science Thesis

For obtaining the degree of Master of Science in Aerospace Engineering at Delft University of Technology

Ruben Vandenheede

June 18, 2012

Faculty of Aerospace Engineering · Delft University of Technology

Delft University Of Technology
Department Of
Department of Aerodynamics

The undersigned hereby certify that they have read and recommend to the Faculty of Aerospace Engineering for acceptance a thesis entitled **"Force Generation of Bio-Inspired Hover Kinematics"** by **Ruben Vandenheede** in partial fulfillment of the requirements for the degree of **Master of Science**.

Dated: June 18, 2012

Head of department: _____
Prof.dr.ir.drs. H. Bijl

Academic Supervisor: _____
Dr.ir. B.W. van Oudheusden

Company Supervisor: _____
Prof. L.P. Bernal

Reader: _____
M. Perçin, MSc

Summary

The field of remote sensing and information gathering is being revolutionized by the recent developments in Micro Air Vehicles, MAVs. The need for maneuverability and flight in confined spaces has directed the focus of research towards flapping flight.

Biological flapping flyers exhibit all the characteristics that are desired by MAVs. Biological flyers are able to hover, make rapid changes in their attitude, and navigate through very narrow spaces. For the purpose of this Master thesis the hawkmoth was used as a starting point and source of inspiration. First and foremost the hawkmoth is a fairly large insect, with a wingspan of roughly 10 cm. The larger scale of the insect will translate to an easier design in terms of the scalability of structural and electronic components. Furthermore, the hawkmoth displays consistent and simple kinematics.

The complex aerodynamics are not fully understood, it is still unclear how we can design flapping kinematics that will lead to an optimum performance with respect to maneuverability, speed, and energy efficiency and are feasible to manufacture. The problem is tackled through an experimental campaign in a water channel. The kinematics investigated are two pitch-plunge motions based on the hawkmoth and a third purely sinusoidal motion. The Reynolds number is $4,800$ and the reduced frequency is 0.38, similar to the hawkmoth. The kinematics are subjected to force data acquisition, flow visualization, and particle image velocimetry. The results are compared to flapping experiments and calculations using computational fluid dynamics and an unsteady vortex model.

The results show that the effect of the elevation angle is very important when looking at the details of the force development. A strong correlation between the strength of the leading and trailing edge vortex and the forces was found. The force data acquired during the experiments compares well to the to the CFD calculations. The calculated force coefficients are between 82 and 87 % of the magnitude measured during the experiments. The bias towards a lower value can be explained partially by the assumptions of the CFD model and the presence of blockage effects during the experiments. Comparison with the unsteady aerodynamic vortex model suggests that the dominant force generating mechanisms are the leading and trailing edge vortices. The impact of spanwise flow and tip vortices on the overall magnitude of the forces is not as significant. The comparison

of pitch-plunge experiments with flapping experiments showed a good agreement as well. The force coefficients measured during flapping are about 50 % smaller compared to the pitch-plunging case. The difference is attributed due to the fundamental difference in kinematics and the definition of the reference velocity. The agreement of the shape of the time history of the forces suggests that the underlying flow topology is analogues in both cases. It remains to be evaluated if the spanwise flow component is also present and whether the evolution of the tip vortices is comparable.

The application of advanced and delayed rotation proved to have dramatic effects on the force generation. Delayed rotation is detrimental to the force production, thrust produced was 60 % less compared to the baseline cases. Advanced rotation yields an increase in thrust of 34 to 47 % with a reduction of up to 20 % in efficiency. The flow topology was remarkably similar to the baseline kinematics with a slight shift in phase. Both the application of advanced and delayed rotation provides a large potential in maneuverability. An increase in reduced frequency to a value of 0.7 lead to an increase in the thrust produced. A qualitative study of the flow topology showed that the vortical structures were similar to the baseline cases. A small decrease in efficiency was measured for the bio-inspired cases and a small increase for the harmonic motion. It might thus be favorable for roboflyers to flap at higher reduced frequencies.

Acknowledgments

No thesis is ever the product of one person's efforts, and this one was no different. This thesis would never have become reality without the help and suggestions of many supportive friends and colleagues. I am very grateful for all the support I have received.

First and foremost I would like to thank my supervisor Prof. L.P. Bernal for providing me with the opportunity to perform research at the University of Michigan. He has been great and I am very thankful for his guidance and advice. Furthermore I would like to thank Ir. C.L. Morrison for the many discussions we had and for the experimental data he shared with me, Dr.ir. C. Kang for bouncing of ideas and his CFD work, and Dr.ir. A. Gogulapati for the unsteady vortex model calculations, sharing ideas and providing feedback. I am also very grateful to Dr.ir. M.V. Ol and Dr.ir. K. Grunland for their support.

Furthermore I am very grateful for the support I have received from the people in Delft. I would like to thank Prof.dr.ir.drs. H. Bijl and Dr.ir. B.W. van Oudheusden for their guidance throughout the writing of my thesis. I would also like to thank M. Perçin, MSc, for his time and efforts in reading my report and being part of my exam committee.

Lastly, a special thanks goes out to my family and friends for their unconditional support throughout my journey in the Netherlands and the United States, especially to the people at home for not letting me down even when I was more than $6,000\,km$ apart.

Thank you all.

Ruben Vandenheede
Delft, The Netherlands
June 18, 2012

Contents

List of Figures

List of Tables

Nomenclature

Latin Symbols

$(F_i)_{viscous}$	Viscous shear in i-direction
$\mathbf{V}$	Three component velocity vector
$\mathbf{D}$	Displacement vector in three dimensions
$\mathbf{d}$	Displacement vector with respect to the interrogation window
$\mathbf{s}$	Separation vector in the correlation plane
$\mathbf{X_i}$	Particle position in three dimensional space
$\mathbf{x_i}$	Particle position with respect to the interrogation window
A	Area swept by the wing
a_I	interrogation area
AR	Aspect ration
b	Wing span
c	Chord length
C_L	Lift coefficient
c_m	Mean chord length
c_r	Root chord length
C_T	Thrust coefficient
E	Young's modulus
f	Flapping frequency
f_i	Body forces acting on the fluid in i-direction
f_n	Natural frequency

$F_{lateral}$	Force lateral to the plunge motion
h	Plunge position
h_0	Plunge amplitude
h_s	Wing thickness
I	Image intensity
I_B	Mass moment of inertia
k	Reduced frequency
L	Lift force
L_{ref}	Reference length
M	Figure of merit
M	Magnification factor
m	Mass
M_z	Moment around the z-axis
P	Power
P_{ideal}	Ideal power (momentum theory)
q	Dynamic pressure
R	Semi-span
r_c	Vortex core size
R_I	Autocorrelation function
R_{II}	Cross-correlation function
Re	Reynolds number
S	Projected wing area
St	Strouhal number
T	Period of the motion
T	Thrust force
t	Time
t	Wing thickness
t^*	Time non-dimensionalized with the period
u	Velocity component in x-direction
U_∞	Free stream velocity
u_i	Velocity in i-direction
U_{ref}	Reference velocity
v	Velocity component in y-direction
V_0	Transfer function given the light energy and its conversion into an electric signal
w	Velocity component in z-direction
w^0	Displacement in z-direction

p	Pressure

Greek Symbols

$\mathcal{O}$	Big O Landau
∇	Del operator
α	Feathering angle
Γ	Position vector of the ensemble of all particles
δ	Pitch angle
θ	Elevation angle
ν	Poisson ratio of the material
Π_1	Effective stiffness parameter
Π_2	Effective rotational inertia
Π_3	Frequency ratio
$\bar{\rho}$	Non-dimensinalized density
ρ	Density of the fluid
ρ_s	Density of the wing
τ	Gaussian image intensity for the point spread of a particle
ν	Viscosity of the fluid
Φ	Flapping amplitude
ϕ	Flapping angle
ω	Vorticity

Abbreviations

3AXM	Third Steering Muscle
CCD	Charge-Coupled Device
CFD	Computational Fluid Dynamics
DLM	Dorsal Longitudinal Muscle
DNS	Direct Numerical Simulation
DOF	Degrees Of Freedom
DVM	Dorsal Ventral Muscle
FFT	Fast Fourier Transform
HM1	Hover Motion One
HM2	Hover Motion Two
KD*P	Potassium Dideuterium Phosphate
LASER	Light Amplification by Stimulated Emission of Radiation

LEV	Leading Edge Vortex
LE	Leading Edge
MAVs	Micro Air Vehicles
Nd:YAG	Neodymium-doped Yttrium Aluminum Garnet
PIV	Particle Image Velocimetry
RANS	Reynolds Averaged Navier Stokes
RMS	Root Mean Square
TEV	Trailing Edge Vortex
TE	Trailing Edge

Chapter 1

Introduction

Recent developments in micro air vehicles (MAVs) are revolutionizing remote sensing and information gathering. For very small vehicles, flapping wings have unique characteristics that could provide exceptional capabilities in maneuverability, hover performance, as well as in their ability to operate in confined spaces. These performance characteristics are observed in insects and small birds motivating studies of the aerodynamics of flapping wings of biological flyers [39].

Understanding the aerodynamics of biological flyers can provide insights useful for the design of flapping wing MAVs. A very well studied example of a biological flapping flyer is the hawkmoth [56]. Hawkmoths are large moths with wing span that can exceed $10\,cm$, and they operate in a higher Reynolds number regime more akin to small birds than to most insects. Hawkmoths show consistent wing beat parameters, for an individual moth as well as for comparing different moths. Also the main features, dominant in general flapping insect flight, are present in the stroke of the hawkmoth, without the complications of extra mechanisms present in a number of other insects, e.g. exaggerated ventral flexion.

The wings of insects produce more lift than predicted with conventional aerodynamic theory, i.e. compared to the steady motion at the same velocity and angle of attack. Aerodynamic studies of hawkmoths and other small insects have shown relevant flow phenomena in the generation of force, e.g. leading edge vortex formation [10]. The leading edge vortex (LEV) can account, in part, for the quantitative disagreement with the forces predicted by conventional aerodynamic theories [13]. The LEV generates a lower pressure area at the leading edge resulting in a large force production. Other mechanisms have been identified to further enhance performance, including clap & fling and wake capture.

Recently the aerodynamics of pitching and plunging airfoils has received considerable attention (e.g. Yeon et al [8], Granlund et al [19] and Rausch et al [33]). Granlund et al [19] considered the aerodynamics of a flat plate that is free to pivot about the leading edge between $\pm 45°$ incidence limiters and the translation is a prescribed sinusoidal function.

For an aspect ratio of 3.4 they found that the stroke to chord ratio is the main factor affecting the thrust production, with small stroke to chord ratios evincing the lowest thrust. The results are insensitive to changes in Reynolds number, within the $5,000$ to $20,000$ range. Furthermore no evidence of wake capture was found in these experiments.

In this context a new experimental study on the unsteady aerodynamics for pitch-plunge kinematics in hover is explored, with the intent of application to flapping flight in a later stage. The goal of the research described in this thesis can be summarized as follows:

> *To gain a better understanding of the unsteady aerodynamics in flapping, hovering flight by generating a bio-inspired pitch-plunge kinematic and investigating it in great detail.*

The present work extends the pitch-plunge studies by considering the aerodynamics of an elliptical flap plate wing with bio-inspired hover motions. The kinematics are derived from the hover kinematics of the hawkmoth. It is not possible to capture all features from a three degree of freedom flapping motion into a two degree of freedom pitch-plunge motion. Therefore two main kinematics and a third purely sinusoidal motion are investigated.

Figure 1.1: Hummingbird hawkmoth in hover

The experimental campaign is initially conducted at the Reynolds number and reduced frequency of the hawkmoth in hover, $4,800$ and 0.38 respectively. The campaign includes force data acquisition to obtain the time history of the forces and the cycle average force. From the force measurement the power input can be deduced and hence a figure merit for the propulsive efficiency of the stroke. Furthermore particle image velocimetry (PIV) is used to get a detailed qualitative and quantitative understanding of the flow topology. The results complement current related studies on the effects of flapping reported by Morrison et al [30] and Yeo et al [57].

The thesis includes several chapters, the journey starts with an overview of biological flapping flight in Chapter 2. Here the historical overview, mechanics of flapping flight,

scaling and aerodynamic principles are presented. The experiments are scaled to match the flight regime of a hawkmoth in hover, the dynamic scaling method is discussed in Chapter 3. Chapter 4 presents the kinematics used in the experiments. All experiments were conducted at the Aerospace Engineering department of the University of Michigan. A full description of the facilities, instrumentation and applied methods is presented in Chapter 5. Subsequently a detailed discussion of the results is presented in Chapter 6. The thesis is concluded in Chapter 7 by summarizing the most pertinent findings and stating recommendations for future research.

Chapter 2

Biological Flapping Flight

To gain a better understanding of the unsteady aerodynamics in flapping flight of insects, a general overview is provided in Section 2.1. First, a brief historic overview of the evolution of flight and the different mechanisms to achieve flapping flight is given. Next, we will look at flapping flight from a design perspective and discuss the relevant scaling laws and the aerodynamics that enable flapping flight.

The hawkmoth is an example of a fairly high Reynolds number flapping flyer, with length scales similar to a hummingbird. The hawkmoth is a large moth, which is very agile and has the ability to hover. It is an excellent starting point for scaling down electronics and use a large-to-small approach. Section 2.2 will discuss the general characteristics of the hawkmoth.

2.1 General Insect Flight

2.1.1 Brief historic overview

Insects are one of the oldest groups of living species in the world, the oldest insect fossils found are roughly $396 - 407$ million years old [14]. The number of insects is vast, the number of named insect species alone is approximately $925,000$, a typical garden contains at least $1,500$ species. The estimation of the total number of insect species remains very controversial and varies widely from roughly 2 million to 30 million species.

It is still unclear when insects first started to conquer the sky. Fossils found from the earliest insects suggest that wings may have evolved already at that time, approximately $396 - 407$ million years ago. This new morphological evolution provided a boom for insect development. From now on insects were able to relocate to a different environment, this meant that they could go and look for a more suitable habitat and escape predators by simply flying away. Due to the higher geographical spread of different insects, flying has

increased the genetic diversity considerably, leading to a faster development.

The refinement of flight ensured that insects have made significant derived advancements. Due to the development of the neural capacity needed for the control of their bodies in the highly three dimensional environment of flight, insects evolved advanced, sophisticated sensory and integrated neural systems. That is, they have acquired acute and efficient sense of smell (olfaction) and vision. Furthermore, some insect species have progressed to the extent that they could be called intelligent, i.e. they have the capability to learn [20].

Genetic and fossil evidence suggests that it is likely that insect flight evolved only once. It is however still unclear exactly how insects developed the ability to fly. There are a number of different theories on how insect flight came about. The two mainstream theories are the paranotal lobe theory and the exite theory.

Paranotal lobes are fixed extensions of the thoracic terga, the paranotal lobe theory postulates that wings developed from these fixed extensions. Originally these lateral extensions of the thorax were not articulated and seemingly used for parachuting and gliding. At first this would have been passively stabilized gliding and it is plausible that evolving muscles and joints for active control have led to the development of actual insect flight. Scientists are still looking for supportive evidence, e.g. paranotal lobes with vein patterns found on the prothoracic segments of some paleozoic insects, and the fossils displaying the evolution of joints and muscle structures needed to advance from parachuting to flying.

The second main stream theory, the exite theory, proposes that wings evolved as an adaptation of endites and exites. Exites and endites are primitively annulated outpouchings in the dorsal area, which are moved from their bases by extrinsic leg muscles of the neighboring segments and do not carry intrinsic musculature. Exite lobes articulate dorsolaterally, whereas endite lobes articulate medioventrally [49]. Accordingly, suggesting that insect wings are serially homologous with the movable abdominal gills on mayflies. The gill is a modified exite of a hypothetical basal leg podite, the articulating exite of this leg segment over time evolved into gills and legs. Figure 2.1 shows the gills of immature mayflies, resembling tiny wings, and according to the exite theory these are serially homologous with insect wings.

Regardless of the evolutionary background of flying insects, their anatomy is especially adapted to allow flapping flight.

2.1.2 Mechanisms for flapping flight

Compared to fixed wings, flapping flight is more complex due to structural movement and resulting unsteady aerodynamics. Flapping wings typically have 3 angular degrees of freedom, as defined in Chapter 4. For insects all actuation of the wing is carried out at the wing root [5], some insects do not move their wings in a direct manner, instead they

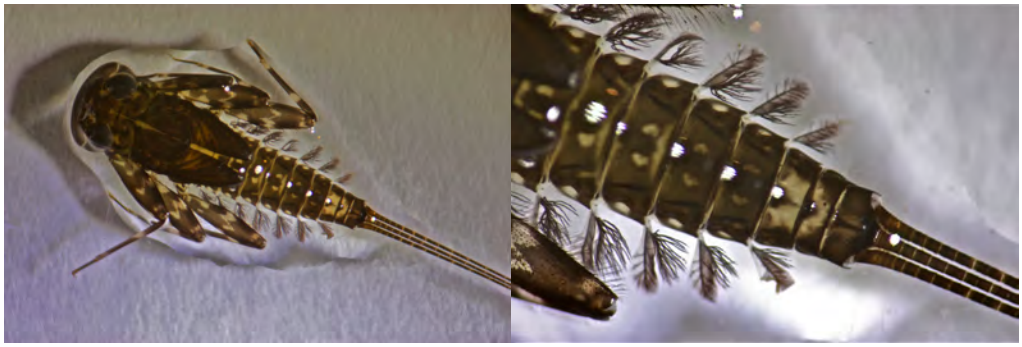

(a) Mayfly with gills on the abdominal segments

(b) Close up of the gills of a mayfly nymph, note the "feathery" fibers behind each gill, called fibrilliform

Figure 2.1: Gills on the abdominal segments 1 through 7 of a mayfly, Heptagenia, nymph [1]

have indirect flight muscles. The indirect flight muscles take in almost all the space in the pterygote thorax, and change the overall shape of the entire thorax. When the flight muscles contract they deform the thorax pointing the wing downwards (downstroke), and the elastic energy stored because of the thorax deformation causes the upstroke [20]. Some insects, including the hawkmoth, will use a combination of indirect and direct flight muscles to exert control over the kinematics [52].

Insects control these muscles, and therefore the wing beat, through neural stimulation. The neural stimulation of the muscles providing the wing beat can differ depending on the flapping frequency. For insects with a low flapping frequency the muscles are controlled with one signal per contraction, also known as synchronous flight muscles. The modulation of the flapping and feathering angle occurs by regulating the timing of the muscle contraction. Conversely asynchronous flight muscles are muscles controlled with an on/off signal, these are used when the flapping frequency is high and exceeds the "sampling" frequency of their brain.

Flapping frequencies in insect flight range from 5 to 200 Hz, decreasing with increasing insect size and weight, cf. Section 2.1.3. In this frequency range there is a need for high speed photography to determine the kinematics. Consequently only recently have detailed accounts of kinematics been published [52, 56].

For the purpose of this study we will restrict ourselves to insects with one pair of wings, or wings that can be considered to act as one, i.e. they move in near unison. In one flapping cycle four kinematic portions can be identified, there are two translational phases, upstroke and downstroke, and two rotational phases, pronation and supination. Pronation and supination is the rotation that occurs at stroke reversal preceding downstroke and upstroke respectively. The path described by the wing tips during a stroke is similar to a figure eight on a spherical surface. The flapping amplitude of insects ranges from about 1.5 to 2.5 radians, and the tip travels between 3 and 7 chord lengths.

Figure 2.2: Hawkmoth in hover during feeding, an example of an insect using the hovering stroke

The hovering capabilities of insects are limited by size, moments of inertia of the wing, degrees of freedom in the movement of the wings, and the shape of the wing [39]. In hover the duration of the downstroke and the upstroke tend to be roughly the same. Two distinctly different kinematics are observed for hovering insects, the symmetric hovering stroke and the asymmetric hovering stroke [53].

In the asymmetric hovering stroke, also known as the ”avian” stroke, the wings are flexed back in one part of the stroke to reduce the amount of drag produced, and the other part of the stroke produces the majority of the thrust. Generally this hovering method is used in larger species and is sustained for only short periods of time [7].

In symmetric hovering flight, using the ”hovering” stroke, the wing beat is relatively symmetric and both up and downstroke produce a significant portion of the lift. This hovering stroke is used in all small insects as well as in some larger species, e.g. the hawkmoth (Figure 2.2).

2.1.3 Scaling

Insects can be categorized in many ways, and for the purpose of a general understanding of small flapping vehicles we borrow from aircraft design. Traditionally the conceptual design of airplanes uses dimensional analysis and scaling laws based on a limited number of variables including geometry, weight and velocity range [47, 34, 45]. Bejan (2006) showed that for biological locomotion similar scaling rules can be applied [9], and these can be extended to the subsection of insect flight.

General animal locomotion

When comparing the gait of a human with the wing stroke of a hawkmoth it seems as if both motions are completely uncorrelated. In general running, flying and swimming animals are very contrasting. There is a distinct difference in the physical mechanisms used, and the media in which they occur are very different.

Looking from an energy perspective however it can be shown that in theory all these motions are correlated by the fact that all flow systems evolve to optimize the use of energy, also known as the unifying constructal theory [9]. This minimal energy perspective on biological systems reveals scaling relations between body mass, speed, force output and frequency of the flap, stride, or stroke. The theory predicts that swimming, and flapping will only occur at Reynolds numbers higher than 30 and that all animal locomotion will have a Strouhal number which is more or less constant. Furthermore it is shown that both animal movement (running, flying, and swimming) and fluid eddy movement is a form of optimized intermittent movement, i.e. both eddies and animals are the 'construct' that travels through the medium with the least amount of useful energy expenditure per distance traveled.

The scaling relations of general animal locomotion for velocity, frequency, and force output with respect to the animal mass are visualized in Figure 2.3. They show clear and distinct proportionality laws with respect to the body mass. Hence a rough sizing estimate for insect flight and MAV development can be done purely on a dimensional and scaling basis.

Flapping flight

When analyzing and designing a flapping wing vehicle, biological or artificial, there are a vast number of parameters and variables to take into account. These can be divided into two categories. First, there are parameters and variables related to the medium in which the vehicle or organism moves and second the ones related to the vehicle or organism itself.

The fluid parameters are the density of the fluid, ρ, and the viscosity of the fluid, ν. These two parameters will drive the fluid behavior. The fluid motion is governed by the Navier-Stokes equations, shown in equations 2.1 through 2.4 for a Cartesian reference frame [22].

$$\frac{\partial \rho}{\partial t} + \nabla \cdot (\rho \mathbf{V}) = 0 \tag{2.1}$$

$$\frac{\partial \rho u}{\partial t} + \nabla \cdot (\rho u \mathbf{V}) = -\frac{\partial p}{\partial x} + \rho f_x + (F_x)_{viscous} \tag{2.2}$$

$$\frac{\partial \rho v}{\partial t} + \nabla \cdot (\rho v \mathbf{V}) = -\frac{\partial p}{\partial y} + \rho f_y + (F_y)_{viscous} \tag{2.3}$$

$$\frac{\partial \rho w}{\partial t} + \nabla \cdot (\rho w \mathbf{V}) = -\frac{\partial p}{\partial z} + \rho f_z + (F_z)_{viscous} \tag{2.4}$$

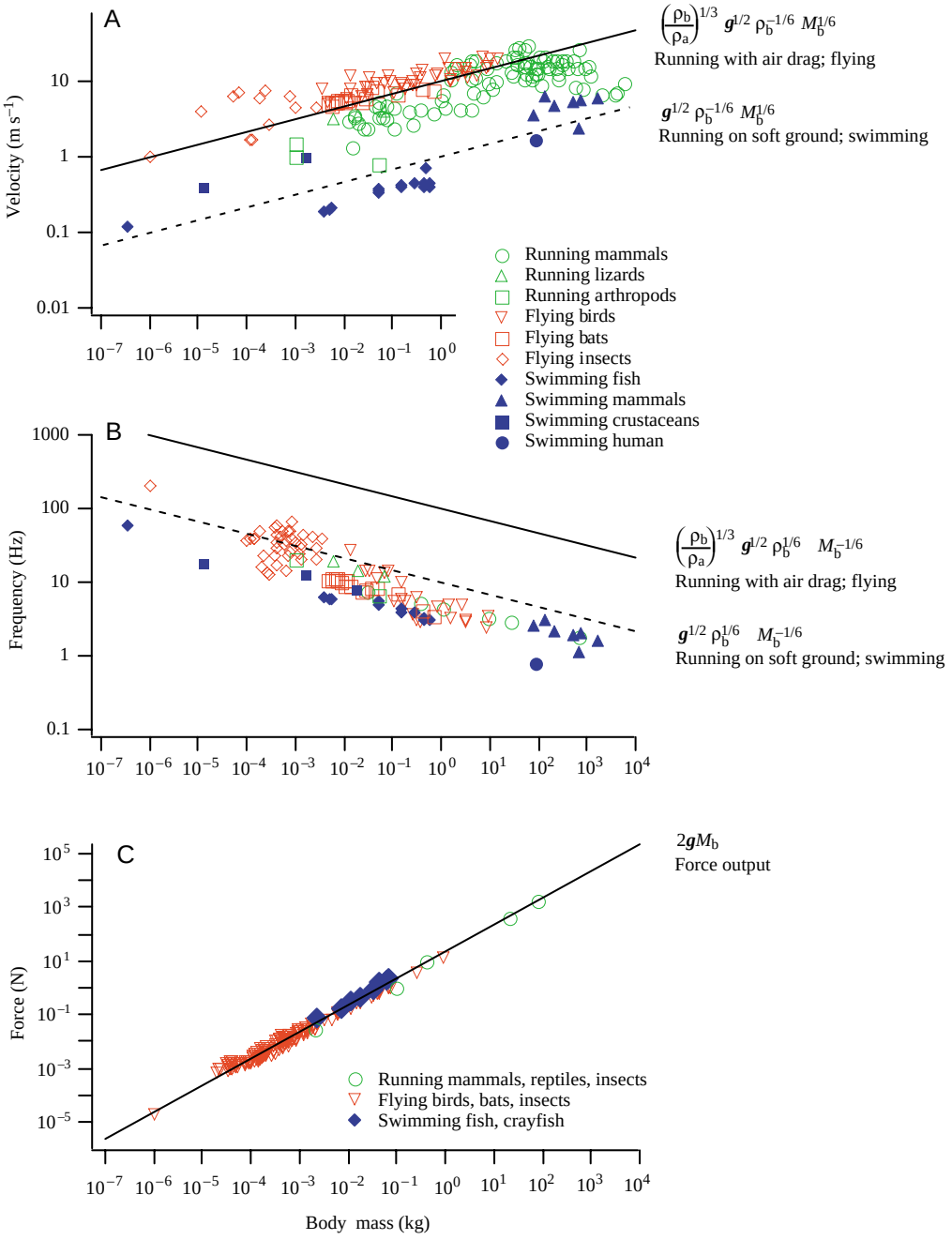

Figure 2.3: Comparison of the relation between body mass and speed (A), stroke frequencies (B), and force outputs (C) with theoretical predictions for a wide variety of animals [9]

Where ∇ is the del operator, $\mathbf{V}$ is the three component velocity vector consisting of the velocity in x, y and z direction, u, v and w respectively. The symbol p denotes the pressure, f_i denotes the body forces acting on the fluid in i-direction and similarly $(F_i)_{viscous}$ denotes the i-component of the viscous shear. Equation 2.1 is commonly referred to as the continuity equation and ensures conservation of mass. Equations 2.2 through 2.4 are the momentum equations and ensure conservation of momentum, equivalent to Newtons 2^{nd} law. On the left hand side the momentum of the fluid is represented and on the right hand side the forces acting on the fluid are shown.

The Navier-Stokes equations are inherently complex and they are not easily solvable. Analytical solutions only exist when simplifying the equations, simplifications include the assumption of an incompressible fluid, an inviscid fluid etc. For most practical applications the equations are solved numerically, direct numerical simulations (DNS) are possible, but computationally expensive. For most cases in Computational Fluid Dynamics (CFD) simplified forms of the Navier-Stokes equations are solved, e.g. Reynolds Averaged Navier-Stokes (RANS). This also reveals one of the benefit of using experiments as a validation tool, since they inherently 'solve' the complete set of equations the validity of the assumptions can be assessed.

The parameters related to the vehicle are more numerous. The first group are the morphological parameters. There is the total mass of the system, typically denoted by m. The total mass can be segmented into the structural mass of the system, the mass related to the propulsion (energy storage and motor or muscles), the mass of avionics, control systems, and the payload.

The geometry of the wing is driven by the wing span, typically denoted by the symbol b or R, the projected wing area, S, chord length, c, and the wing thickness, t. The definition of the span can vary, typically b denotes the tip-to-tip length, however in some cases it is also used to denote the semi-span, i.e. the distance from the root to the tip of a single wing. Similarly for the chord length two different reference lengths are used, the root chord c_r and the mean chord length, c_m. Derived from the geometry and the density distribution of the wing structure the wing mass and its moments of inertia can be determined.

Using these parameters and equations, scaling laws can be derived similar to the law's presented in Figure 2.3. The wing loading, L/S, will be used as an example. It can be shown that an expression for lift, L, can be obtained using the Buckingham π theorem [22].

$$L = \frac{1}{2}\rho U^2 C_L S \tag{2.5}$$

Where ρ is the density of the fluid, U denotes the freestream velocity and C_L is a the lift coefficient. For flight in a steady state the lift is equal to the weight of the vehicle

$W = L$, hence equation 2.5 can be rewritten.

$$\frac{W}{S} = \frac{\rho U^2}{2} C_L \tag{2.6}$$

Equation 2.6 clearly shows that the wing loading is directly related to freestream velocity, i.e. the flight speed [45]. Similarly proportionality, analogous to the unifying constructal theory [9], can be found between the mass of the vehicle and its cruise speed. These relations for a range of both biological and man-made flyers are shown in Figure 2.4.

The flapping flyer interacts with the fluid through the wing kinematics. The kinematics of the wing are governed by the flapping frequency (f), the flight speed and the variation in time of angular motion of the wing. The angular motion of the wing is represented by three time-dependent angles as described in Chapter 4, the flapping angle ϕ, elevation angle θ, feathering angle α.

We can now combine parameters to clearly identify properties of the entire system. As we shall see, certain combinations of parameters become more dominant under given flight conditions.

The Strouhal number, St, is the ratio between the flapping and the forward velocities, it gives an indication of how fast vorticity is transported downstream. The Strouhal number thus characterizes the vortex dynamics of the wake and shedding behavior of vortices in forward flapping flight, and is defined as follows [37].

$$St = \frac{f L_{ref}}{U_{ref}} = \frac{f R \Phi}{U_\infty} = \frac{f AR\, c_m \Phi}{2 U_\infty} \tag{2.7}$$

The reference velocity is commonly chosen to be the freestream velocity. The reference length in this case is the arc described by the tip of the wing, $R\Phi$. Where Φ is the flapping amplitude and R can be expressed in function of the aspect ratio and the mean chord, i.e. $R = AR\, c_m$.

The Strouhal number is typically used for characterization of unsteady aerodynamic flow phenomena. A variation of the Strouhal number for swimming and flying animals is shown in Figure 2.5. On the far right of Figure 2.5 we see that dolphins swim at a Strouhal number of approximately 0.3. Most larger birds fly at a Strouhal number of about 0.2, in contrast insects and moths generally fly at a Strouhal number that is around 0.3. The general trend is a Strouhal number between 0.2 and 0.4 for both aquatic and flying animals. For forward flight it seems that this range of Strouhal number provides the animals with the highest propulsive efficiency [44].

Derived from the Navier-Stokes equations an important dimensionless parameter can be defined, the Reynolds number. The Reynolds number is the ratio of viscous forces and

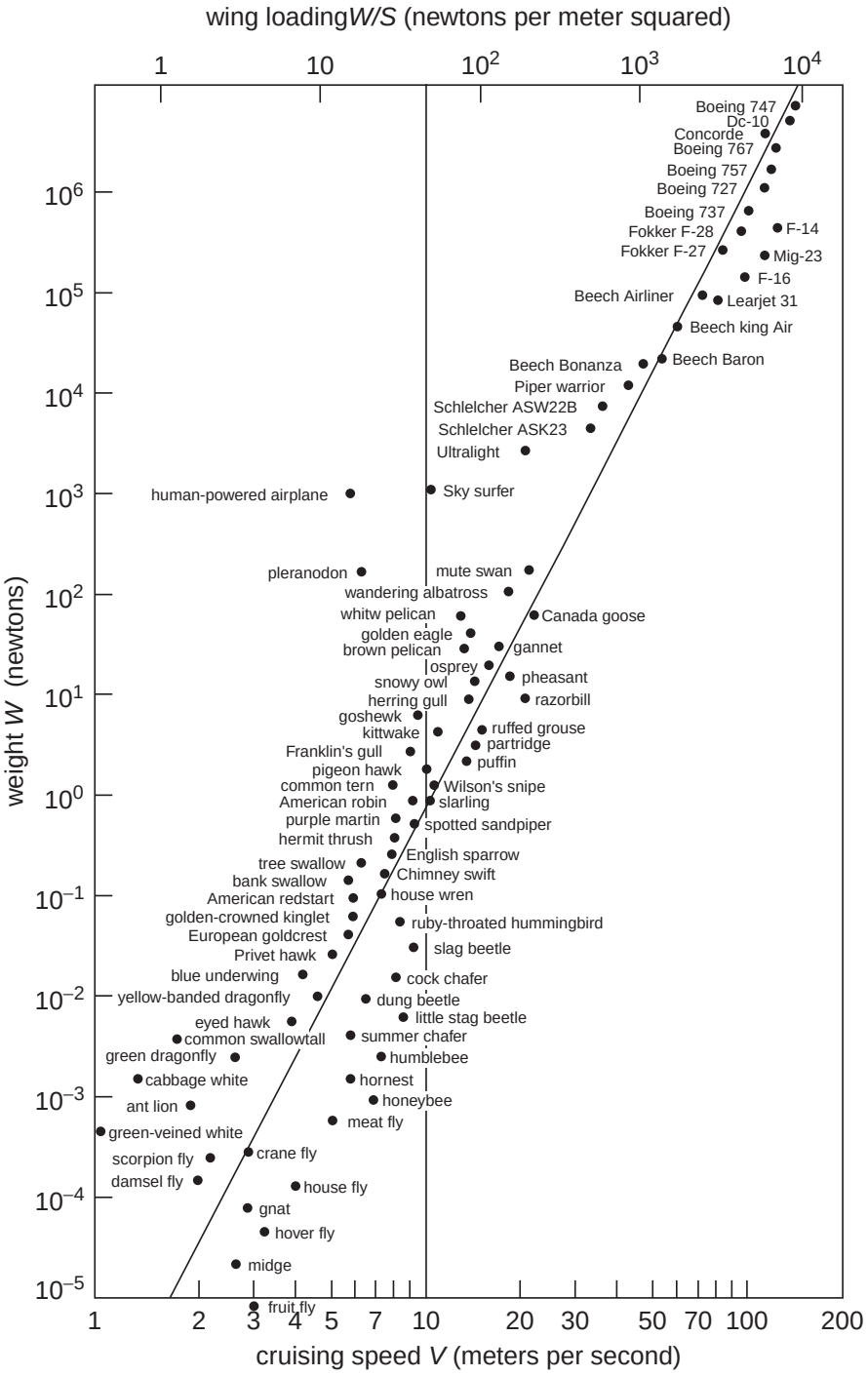

Figure 2.4: The Great Flight Diagram, a relation between weight cruise speed and cruise speed [45]

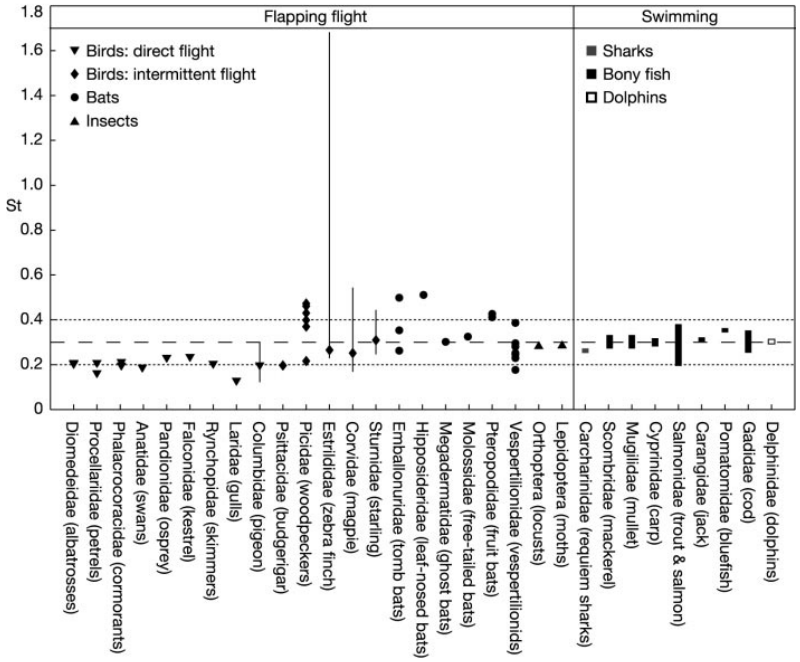

Figure 2.5: The range of Strouhal numbers for flying and swimming animals [44]

inertial forces exerted by the fluid, shown in equation 2.8.

$$Re = \frac{\rho_f L_{ref} U_{ref}}{\mu} = \frac{L_{ref} U_{ref}}{\nu_f} \tag{2.8}$$

Where ρ_f is the density of the fluid, L_{ref} is a reference length scale, U_{ref} is the reference velocity, and ν_f is the viscosity of the fluid. The reference length scale can be chosen arbitrary, but must be a consistent choice if one wants to compare the Reynolds numbers of two different flows. Typically the chord of the airfoil is used, $L_{ref} = c_m$. The reference velocity has two different definitions depending on the flight condition. For forward flight the freestream velocity, U_∞, is used and hence the Reynolds number becomes.

$$Re = \frac{U_\infty c_m}{\nu_f} \tag{2.9}$$

In hover the freestream velocity is zero and hence a different velocity is used to characterize the inertial forces. The average tip velocity is chosen as a reference, $U_{ref} = U_{tip}$, and can the Reynolds number be expressed as a function of the aspect ratio, the flapping amplitude (Φ), the flapping frequency, and the chord length.

$$Re = \frac{AR\,\Phi f c_m^2}{\nu_f} \tag{2.10}$$

The reduced frequency, k, compares the period of the wing motion with a relevant flow time scale. Similar to the Strouhal number the reduced frequency provides a good measure

of the unsteadiness of the flow. The reduced frequency is defined as follows.

$$k = \frac{\pi f c_m}{U_{ref}} \tag{2.11}$$

In forward flight the reference velocity for flapping flight is simply the forward flight speed.

$$k = \frac{\pi f c_m}{U_\infty} \tag{2.12}$$

For flapping hover flight the reference velocity is generally chosen to be the average tip speed.

$$k = \frac{\pi}{\Phi AR} \tag{2.13}$$

Thus the reduced frequency is an adequate parameter to be used for comparison of the unsteadiness in both hover and forward flight. Therefore the reduced frequency is more meaningful than the Strouhal number, which is a purely kinematic parameter for flapping flight.

Assuming an isotropic flat plate for the wing it is also convenient to define a non-dimensional density, the ratio of the structural density and the fluid.

$$\bar{\rho} = \frac{\rho_s}{\rho_f} \tag{2.14}$$

The effective stiffness can then be defined as follows [37].

$$\Pi_1 = \frac{E h_s^3}{12(1-\nu^2)\rho_f U_{ref}^2 c_m^3} \tag{2.15}$$

Where E is the Young's modulus of the structure, h_s is the thickness, and ν is the Poisson ratio of the material. The effective stiffness denotes ratio between elastic bending forces and aerodynamic forces. Similarly the effective rotational inertia, for an isotropic shear deformable plate is defined by [37].

$$\Pi_2 = \frac{I_B}{\rho_f c_m^5} \tag{2.16}$$

Where I_B is the mass moment of inertia. The effective rotational inertia denotes the ratio between rotational inertial forces and aerodynamic forces.

Consider the mean wing tip velocity of the flapping wing as the velocity scale and an isotropic flat plate as the wing structure, than the Navier-Stokes Equations for a constant-density fluid can be non-dimensionalized, shown in equation 2.17, and the out of plane motion of wing is governed by equation 2.18 [37].

$$\frac{k}{\pi}\frac{\partial \bar{u_i}}{\partial t} + \frac{\partial \bar{u_j}\bar{u_i}}{\partial \bar{x_j}} = -\frac{\partial \bar{p}}{\partial \bar{x_i}} + \frac{1}{Re}\frac{\partial^2 \bar{u_i}}{\partial \bar{x_i}^2} \tag{2.17}$$

$$\Pi_1 \left(\frac{\partial^4 \bar{w}^0}{\partial \bar{x_s}^4} + \frac{2\partial^4 \bar{w}^0}{\partial \bar{x}^2 \partial \bar{y}^2} + \frac{\partial^4 \bar{w}^0}{\partial y_s^4} \right) - \bar{\rho}\bar{h_s} \left(\frac{k}{\pi} \right) \frac{\partial^2 \bar{w}^0}{\partial \bar{t}^2} = \bar{f_p} \tag{2.18}$$

Looking at equation 2.17, it becomes clear that for a higher value of the reduced frequency, the unsteady term ($\frac{k}{\pi}\frac{\partial \bar{\mathbf{V}}}{\partial \bar{t}}$) will have a higher influence. Similarly if we focus at the viscous term ($\frac{1}{Re}\bar{\nabla}^2\bar{\mathbf{V}}$) we see that viscous effects will become more dominant as the Reynolds number decreases.

To summarize Table 2.1 gives an overview of the dimensionless numbers and their dependence on size and flapping frequency for both hovering and forward flapping flight [38]. In this table the frequency ratio Π_3 is equal to the ratio of the natural frequency of the structure and the flapping frequency $\frac{f_n}{f}$. Π_3 is influential for wing deformations when wing excitation frequency comes close to its resonance frequency.

Table 2.1: Dimensionless parameters and scaling dependency for flapping wings, hover and forward flight comparison [38]

Dimensionless Parameter	Hover, based on wing tip velocity		Forward flight, based on cruising speed	
	length	frequency	length	frequency
Reynold number	c_m^2	f	c_m	*independent*
Strouhal number	*independent*	*independent*	c_m	f
Reduced frequency	*independent*	*independent*	c_m	f
Π_1	c_m^{-2}	f^{-2}	*independent*	*independent*
Π_2	c_m^{-1}	*independent*	c_m^{-1}	*independent*
Frequency ratios Π_3	c_m^{-1}	f^{-1}	c_m^{-1}	f^{-1}

2.1.4 Aerodynamics of flapping flight

The aerodynamics of flapping flight are governed by the equations for fluid motion named after Claude-Louis Navier and George Gabriel Stokes, equation 2.17. Examining the Navier-Stokes equations a little closer a number of assumptions can be made. First, it can be said that the flow can be considered to be incompressible. Second, the flow is expected to be laminar in most cases and thus turbulent effects will be negligible in these cases. Third, the flow will be highly unsteady, and hence forces will significantly differ from steady state predictions.

Insect flight occurs mostly at low Reynold numbers, $\mathcal{O}(10^1)$ to $\mathcal{O}(10^4)$. The Strouhal number of forward insect flight varies roughly between 0.2 and 0.4. The highly unsteady flow can be characterized by the reduced frequency, for insects typically in the 0.17 to 0.4 range. For a number of selected biological flyers in hover their parameters are summarized

in Table 2.2.

Dynamic scaling, achieved by matching the aforementioned parameters, allows scientists to compare flapping flight of various insects. Furthermore it permits researchers to investigate resulting flow patterns around robotic flappers and relate the results to insects on the basis of similarity. This has led to the identification and classification of several unsteady mechanisms in insect flight.

Understanding is always achieved through simplification, to develop mental constructs facilitating comprehension. Hence some of the aerodynamic mechanisms discussed below may not (yet) be the full theory providing complete or sufficient understanding of flapping flight at low Reynolds numbers, they will however provide useful insight, a way of thought, and communication regarding flapping flight.

Table 2.2: Morphological, flight, scaling, and non-dimensional parameters of selected biological flyers in hover ($U_\infty = 0$) [37]

Parameter	Chalcid Wasp	Fruit Fly	Honeybee	Hawkmoth	Rufous Hummingbird
Mean chord length $[mm]$	0.33	0.78	3.0	18.3	12
Semi-span $[mm]$	0.70	2.39	10.0	48.3	54.5
Aspect ratio $[-]$	4.24	6.12	6.65	5.3	9
Total mass $[g]$	$2.6e^{-}7$	$0.96e^{-3}$	0.1	1.6	3.4
Flapping frequency $[Hz]$	370	218	232.1	26.1	41
Flapping amplitude $[rad]$	2.09	2.44	1.59	2.0	2.02
Mean wing tip velocity $[m/s]$	1.08	2.54	7.38	5.04	8.66
Reynold number $[-]$	23	126	1412	5885	6628
Reduced frequency $[-]$	0.355	0.212	0.297	0.296	0.172

The Wagner effect

Consider a wing at an angle of attack or with a certain camber impulsively started from rest, there will be a finite length of time before the airfoil reaches its steady state condition. In particular the value of the lift coefficient will gradually grow until it reaches its steady state value [21, 36].

The delay in reaching its steady state value is due to two physical processes. First, there is a latency in the corresponding viscous effects that take place on the airfoil. The initial stagnation point will not correspond to the stagnation point in steady state conditions, and a finite time is needed to fulfill the Kutta condition. The second reason is related to the velocity field induced by the shed vorticity at the trailing edge. The shed vorticity will reduce the lift force of the airfoil. The effect will attenuate as the distance between the shed vortex and the airfoil grows.

The lift for impulsively started airfoils can be approximated by Wagner's indicial lift function. The Wagner effect will introduce an overprediction of the forces acting on the airfoil when the force of impulsively started wings is predicted using quasi-steady models. There is an ongoing discussion in the community to what extent the Wagner effect impacts the flow around flapping wings at low Reynolds number, the effect however will be present.

Leading edge vortex

Flapping wings are relatively thin and generally translate at very high angles of attack, this causes the flow to separate at the leading edge. When the flow reattaches before the trailing edge, a leading edge vortex (LEV) forms. The LEV is generated from the balance between the pressure gradient, the centrifugal force and the Coriolis force in the momentum equation [40]. The LEV induces an area of low pressure resulting in large suction on the upper surface of the wing [13], and hence the LEV serves as a high lift mechanism. The combination of the lower pressure region acting mostly normal to the wing surface and the airfoil being at a high angle of attack also leads to an increase in drag. It has been shown extensively that the LEV is common to flapping wing aerodynamics at Reynolds numbers $\mathcal{O}(10^4)$ or lower, i.e. the flight regime of insects.

In the presence of the leading edge vortex the Kutta condition is maintained and a substantial enhancement of lift is achieved. Considering an LEV in a two dimensional flow, the LEV tends to grow in size until the Kutta condition breaks down, at this point the flow is no longer able to reattach and the airfoil will stall. This phenomenon is called delayed stall since the development of the stalled condition takes a finite amount of time to develop. During the delayed stall high lift coefficients can be reached. At low Reynolds numbers, relevant for most insects, the breakdown of the Kutta condition is preceded by the growth of a trailing edge vortex. As the trailing edge vortex detaches it is shed into the wake and a new LEV is formed, this process is periodic and the wake can be identified as a 'von Karman vortex street'.

The first direct evidence that insects are able to leverage the LEV mechanism was obtained by Ellington 1996 [13]. Using smoke visualization around a real hawkmoth Ellington showed that a leading edge vortex existed and in the studied cases the LEV was not shed but remained attached during the stroke. Subsequent experiments were performed around a mechanical model similar to the hawkmoth, producing similar findings. A recent study, using particle image velocimetry on tethered hawkmoths, revealed that the leading edge vortex is not necessarily limited to one wing and can extend across the thorax [11].

High axial flow was also observed and this transport of momentum in the spanwise direction prevents the LEV growth beyond a threshold size such that the fluid remains able to reattach before the trailing edge. The axial flow plays a dominant role in the stabilization of the leading edge vortex. Analogously, stability of leading edge vortices on a delta wing with a high angle of attack is ensured by an axial flow generated by the sweep of such wings [36]. For this stable form of the leading edge vortex, the creation of vorticity at the

leading edge is matched perfectly by the convection and diffusion of the vorticity into the wake.

Recent findings through computational fluid dynamics across an intermediate range of Reynolds numbers, from $\mathcal{O}(10^1)$ to $\mathcal{O}(10^4)$, suggests that although LEV's may occur across this flight regime the physical mechanisms may differ [40].

At higher Reynolds numbers, the vorticity is concentrated into an intense, conically shaped vortex and breaks down at roughly 70 - 80% of the span in the mid-late downstroke, cf. Figure 2.6a. This leads to a complicated region at the tip where the vorticity is very three dimensional [26, 51]. In this Reynolds number regime, $\mathcal{O}(10^3)$ and higher, the LEV contains a high axial flow that stabilizes the vortex, however the LEV tends to break down in the spanwise region between three quarter chord and the tip. Furthermore the LEV of a hawkmoth starts to break down after the first half of the downstroke [40].

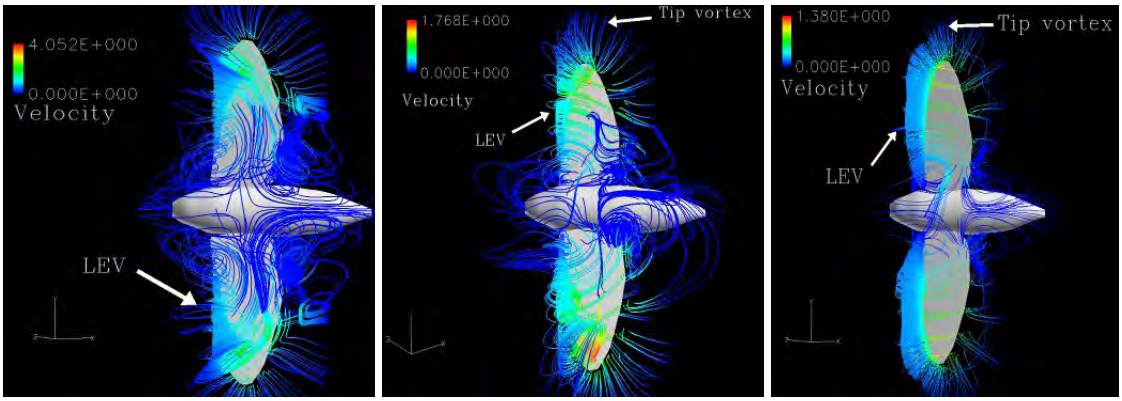

(a) Hawkmoth, $Re = 6000$ (b) Fruit fly, $Re = 120$ (c) Thrips, $Re = 10$

Figure 2.6: Numerical results of leading-edge vortex structures at different Reynolds numbers [40]

For low Reynolds numbers, e.g. fruit fly and thrips, the leading edge and trailing edge vortex become weaker but more stable. As a result the vortex structure becomes more two dimensional, i.e. we see more planar vortex rings at the down and upstroke [26]. At a Reynolds number of 120, the spanwise flow is considerably less, $2 - 5\,\%$ of the averaged tip velocity [40]. In contrast to flapping flight at higher Reynolds number the LEV does not break down near the tip, and is instead connected with the tip vortex, Figure 2.6b. A further reduction of the Reynolds number to a value of 10, shown in Figure 2.6c, leads to a vortex ring connecting the LEV, the tip vortex, and the trailing edge vortex.

There is significant variation in spanwise lift distribution in three dimensional cases. Some cases will have suppressed tip vortices, and some will have prominent tip vortices affecting the lift distribution, hence correlating weakly to the two dimensional cases [48].

The leading edge vortex and the associated delayed stall (formation and evolution) are strongly impacted by the angle of attack, angular velocity, translational velocity, and

translational acceleration of the wing [48]. The LEV is very likely responsible for the majority of the force generation independent of Reynolds number. The Reynolds number will however influence the formation and evolution in terms of stability and three dimensional effects.

The tip vortex

Tip vortices in fixed finite wings are associated with a decrease in lift and induced drag.

Conversely in unsteady flows they create a low-pressure area near the wing tip and interact with the leading edge vortex. Tip vortices can stabilize the flow and exhibit nonlinear interactions with the shed vorticity. A stronger influence of the downwash from the tip vortex will result in reduced lift for lower aspect ratios plates [41].

For flapping wings the tip edge vortex could either promote or have little impact on the lift of low aspect ratio flapping flat plates.

Clap and fling

The clap and fling mechanism, first proposed by Weis-Fogh 1973 [54], is found in a number of small insects, e.g. the chalcid wasp. The leading edges of the wings touch dorsally before they pronate at the end of the upstroke, after which the trailing edges will close in at each other until they meet (clap). During the pronation at the beginning of the downstroke the leading edges will separate first and later the trailing edges (fling).

During the clap the vorticity around both airfoils will counter act each other and no 'stopping' vortex will occur, the trailing edge vorticity will therefore not be present in the downstroke and thus the Wagner effect will be absent or extremely weak. A secondary effect is the jet expelled from the clapping motion of the airfoil providing an extra boost in the momentum of the wake. The fling generates an extra low-pressure region between the airfoils accelerating the buildup of circulation around both wings.

The entire clap and fling method is believed to increase the performance in flapping flyers. Since the effectiveness of the clap and fling mechanism depends on the extent the Wagner effect impacts the motion, there remains some controversy on how pronounced the benefits of incorporation of clap and fling are.

Rapid pitch rotations, the Kramer effect

In insect wing kinematics, the wings will be rotating and translating simultaneously; due to this added angular velocity the flow around the wing deviates from the Kutta condition and the stagnation region moves away from the trailing edge. The unsatisfied Kutta condition will cause sharp dynamic gradients at the trailing edge, generating shear flows. The flow will react to the rotation by generating a rotational circulation until the Kutta

condition is restored [36, 5, 39]. In other words, the wings own rotation serves as a source of circulation.

The extra circulation is proportional to the angular velocity of rotation. The net effect can either be detrimental or beneficial to the lift production depending on the orientation of the rotation with respect to the stroke. The shape and size of these force peaks can be controlled by the timing of the pronation and supination. Many insects have evolved to leverage these effects rendering them extremely maneuverable.

Wing-wake interaction

When a flapping motion is established the fluid around the wing will no longer be quiescent. During the translation the wing will leave a wake behind, at stroke reversal the wing will move into its own wake. The effect is especially pronounced at low flying speeds or when hovering, due to the lack of a freestream velocity carrying the wake further downstream.

The wake from the previous stroke contains energy in the form of momentum; the wing will move through this region in the next stroke, passage through this wake could potentially be a way of recovering some of this energy. It has also been postulated that the initial force peak is due to the acceleration of the wing rather than through a reuse or capturing of the energy from the previous stroke.

It is very likely that wing-wake interaction will be reflected in the time history of the force coefficients, especially right after stroke reversal, although it might be challenging to quantify the effects of the interaction.

Gusts and time scales

Wing beat frequencies are higher than environmental perturbations, thus can be modeled as a constant freestream for most practical applications. The gust response depends on its strength, orientation, and the kinematics of the insect [48].

Furthermore because the characteristic time scales of insects are much shorter than that of typical gusts, they are much more stable in a gusting environment [38].

Flexibility

Insects actuate their wings from the root of the wing, all wing deformations are therefore passively achieved through fluid-structure interaction. The passive pitching and bending due to inertial and fluid forces can potentially enhance lift production. Flexibility effects will become more pronounced at flapping frequencies near the natural structural frequencies of the wing.

2.2 Hawkmoth

One family of insects, Lepidoptera, comprises mainly very large insects. The Lepidoptera family contains roughly 174,000 species and can be roughly divided into three categories: butterflies, skipper butterflies, and moths. The latter contains the subspecies Sphingidae, also known as hawkmoths, and contains about 1,450 varieties [31].

The hawkmoth is a very large moth, with a wingspan in the range of 35 - 150 mm. In Figure 2.7 a picture of a group of Privit hawkmoths (Sphinx ligustri) on the hands of people is shown, which gives a good indication of its size.

Figure 2.7: A group of Privit hawkmoths (Sphinx ligustri) sitting on the hands of a person

Adult hawkmoths have evolved to feed on the nectar of flowers, and the ingested sugars are rapidly converted into fat [23]. To accommodate this diet hawkmoths have evolved the capability to hover in front of flowers. Whilst hovering in front of a flower they use a proboscis, an elongated tubular appendage from their head, to feed.

Hawkmoths are some of the fastest insects, they are able to fly in all directions: forward, backward, up, down, and side to side. The latter has been observed in hover as a defense mechanism against predators. They can lift up to 1.4 times their body mass [52].

The nominal forward flight speed of a hawkmoth is about 5 m/s with a wing loading of 9. The Reynolds number typically ranges around 4200 - 5300 [39], this is within the transition range from laminar to turbulent, and measurements of the wake have shown a transition of the wake from laminar to turbulent after a certain distance in hover [50].

The body position and its stroke plane angle vary throughout the flight regime, as the moth transitions to forward flight and its forward speed increases the stroke plane angle increases and there is a decrease in the body angle with respect to the motion [56]. The

wing beat kinematics contain the main kinematic elements that have been consistently observed in other insect species. The wing beat, although variant from individual to individual, is remarkably consistent and there is little variation between successive wing beats or between different insects of the same species [56].

The flight of hawkmoths in forward flight and hover has been studied meticulously. Although they feed upon floral nectars, and thus adults consume a diet that consists primarily of water and sugars, the principal fuel for flight is fat. During pre-flight warm-up fat is supplemented with carbohydrate fuels [23].

The three primary flight muscles are the dorsal longitudinal muscle (DLM), the dorsal ventral muscle (DVM) , and a third steering muscle (3AXM). The DLM and DVM are both indirect flight muscles. The third muscle (3AXM) is a direct muscle used for the active control in free flight maneuvers [23].

The dominant mechanism for lift production in hawkmoths has been found to be the leading edge vortex. Experiments with real moths, tethered, in forward flight have revealed the presence of a significant LEV towards the end of the downstroke. Figure 2.8 shows the flow visualization of a female hawkmoth and the presence the LEV in the downstroke at different flight speeds. Peak forces correspond with the presence and strength of the LEV, and the LEV continues over the thorax and the centerline of the insect [11].

Further experiments observed large axial flow velocity component, with a maximum axial velocity of the same order of magnitude as the mean tip speed [51]. It is believed that the spanwise flow redistributes energy by the convection and diffusion of the vorticity into the wake, preventing the LEV from growing too large and detaching. The leading edge vortex is found to separate at approximately 75 % of the wing length, connecting to a large, tangled tip vortex.

The hawkmoth is an excellent starting point for research into the development of bio-inspired micro air vehicles. The length scales are small enough to leverage the benefits of flapping flight at insect scale, allowing high maneuverability, hover, and stable forward flight. At the same time the length scales are large enough to be able to develop an initial, complete design of the structure and electronics needed. The kinematics of the hawkmoth include the general features akin to insect flapping flight, and at the same time the kinematics are relatively simple.

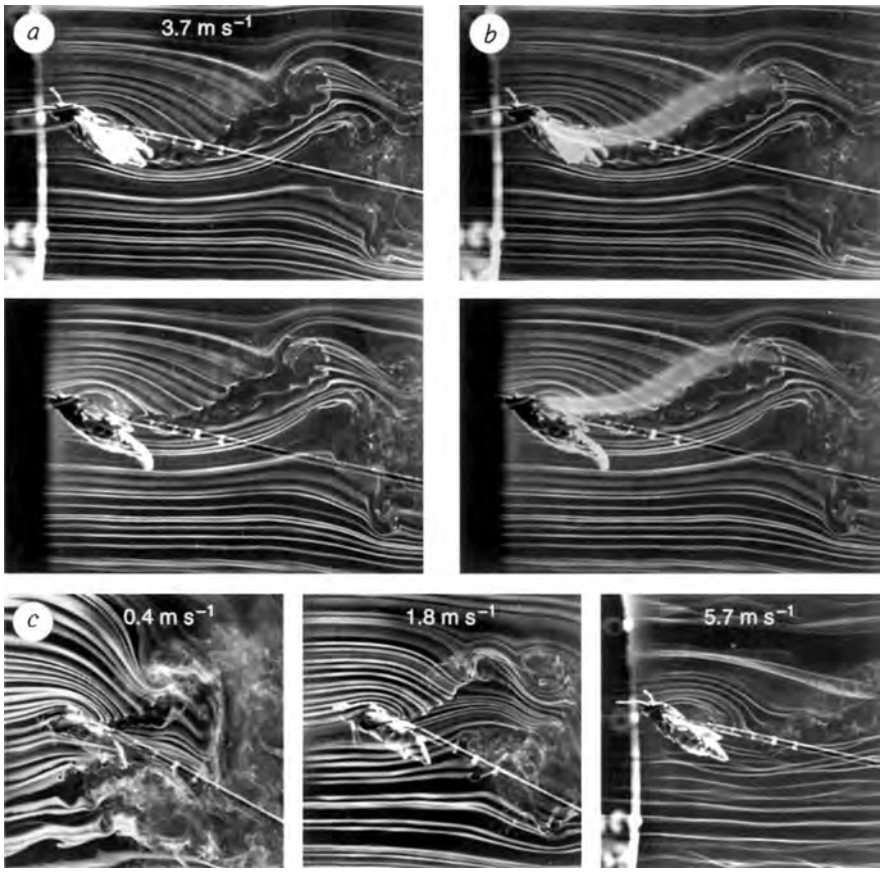

Figure 2.8: Flow visualization around a female hawkmoth in the late downstroke. a, Stereo pair at $3.7\,m/s$; b, stereo drawing superimposed on 'a' to trace the main vortex structures; the top and bottom images correspond to the right and left-hand views. c, Changes in the size of the leading edge vortex at other flight speeds, 0.4, 1.8, and $5.7\,m/s$ respectively [13]

Chapter 3

Experiment Dimensionless Parameters and Scaling

The hover kinematics used in the present research are mainly inspired by the hawkmoth wing kinematics. As a starting point for determining the relevant scaling and non-dimensional parameters, the values of the Agrius Convolvuli are used.

3.1 Hawkmoth, Agrius Convolvuli

The Agrius Convolvuli is a subspecies of the hawkmoth, Sphingidae, common in Europe, Africa, and Australia. It is a large species with a wingspan of about 80 - 105 mm. Similarly to hummingbirds, they have evolved to feed on nectar while hovering in front of a flower. This capability makes them an excellent study object for flapping hovering flight.

The kinematics of this moth in hovering flight are well known, cf. Chapter 4.1. The motion is relatively simple and does not include a clap and fling mechanism. The Agrius Convolvuli is four-winged, but the motion of the wings on both sides in hover is in near unison and can be assumed to act as one wing. The wing planform of both wings together is similar to the Zimmerman planform and will be modeled as such.

The parameters determining the dynamics are presented in Table 3.1. In all equations the subscript m denotes that the parameter is a value of the moth. The flapping frequency and amplitude shown, are those of the moth in hover.

In order to calculate the relevant dimensionless parameters for hover, a reference point on the wing needs to be chosen. In general the wing tip is used for this purpose [37], however since the objective is to capture the most relevant phenomena and try to represent these in a pitch-plunge motion, the tip velocity is an upper bound of the wing speed and will make

Table 3.1: Agrius Convolvuli parameters in hover and experiment parameters

Parameter	Value Agrius convolvuli	Value Experiment
Mean chord length c	$18.3\,mm$	$62.4\,mm$
Semi-Span R	$50.5\,mm$	$241.3\,mm$
Aspect ratio AR	2.76	3.87
Flapping frequency	$26.1\,Hz$	$0.15\,Hz$
Flapping amplitude Φ / h	$2\,rad$	$129.1\,mm$

the scaling parameters too large. A reasonable approximation is to use three quarters of the span ($L_{ref} = 0.75R_m$) as the reference radius.

$$U_{ref} = 2\Phi f_m L_{ref} \tag{3.1}$$

Now the Reynolds number can be determined, a dimensionless number that indicates the ratio of the timescale for viscous transport and convective transport in the flow. The Reynolds number will be based on the mean chord length and the reference velocity, and can thus be rewritten as follows.

$$Re = \frac{U_{ref} c_m}{\nu_a} = \frac{2\Phi f_m L_{ref} c_m}{\nu_a} \tag{3.2}$$

In turn the reduced frequency, equation 3.3, is based on the same reference velocity.

$$k = \frac{\pi f_m c_m}{U_{ref}} = \frac{\pi c_m}{2\Phi L_{ref}} \tag{3.3}$$

With the reference velocity based on three quarters of the span, the Reynolds number and reduced frequency are $4,800$ and 0.38 respectively.

3.2 Relevant Parameters Experiment

The experimental campaign consist of pure pitch-plunge motions of a Zimmerman wing with the parameters given in Table 3.1 The physical dimensions of the Zimmerman wing were determined from consideration of the force sensor and PIV instrumentation requirements. The reference velocity, equal to the average tip velocity, depends only on the plunge amplitude, h_0, and frequency of the motion, f. The result is shown below.

$$U_{ref} = 4 f h_0 \tag{3.4}$$

Substitution of the reference velocity, equation 3.4, leads to the following expression for the reduced frequency of the experiment. Note that in the pitch-plunge case, for a certain wing, the reduced frequency is solely dependent on the amplitude of the motion.

$$k = \frac{\pi c}{4}\frac{1}{h_0} \tag{3.5}$$

Treating the reduced frequency as a constant, i.e. using the value of the Agrius Convolvuli, and using the model mean chord yields an expression for the amplitude of the motion.

$$h_0 = \frac{\pi c}{4k} = 129.1mm \tag{3.6}$$

Similarly, using the same reference velocity, the Reynolds number can be written as.

$$Re = \frac{4c}{\nu_w} f h_0 \tag{3.7}$$

Using the Reynolds number of the moth, an expression for the frequency of the experiment can be obtained.

$$f = \frac{Re\,\nu_w}{4ch_0} \tag{3.8}$$

This equation can be used directly to determine the frequency. However it is convenient to further develop the equation in a slightly different form. First, substitution of equation 3.6 yields.

$$f = Re\frac{\nu_w k}{\pi c^2} \tag{3.9}$$

Secondly, using equation 3.3, we obtain.

$$f = Re\frac{\nu_w}{\pi c^2}\frac{\pi c_m}{2\Phi R_m} \tag{3.10}$$

Third, substitution of equation 3.2 leads to the following expression,

$$f = \frac{2\Phi f_m R_m c_m}{\nu_a c^2}\frac{\nu_w c_m}{2\Phi R_m} \tag{3.11}$$

which simplifies to.

$$f = f_m \left(\frac{c_m}{c}\right)^2 \frac{\nu_w}{\nu_a} \tag{3.12}$$

Hence, from equation 3.12 it can be seen that the frequency of the experiment depends solely on the flapping frequency of the moth, the ratio of the mean chords squared and the ratio of the kinematic viscosities. The frequency of the experiment in water using the Zimmerman wing is $0.15Hz$.

$$f = 0.57\% f_m = 0.15Hz \tag{3.13}$$

Chapter 4

Kinematics

The goal of this thesis is to gain a better understanding of the unsteady aerodynamics of flapping, hovering flight by generating a bio-inspired pitch-plunge kinematics and to investigate them in great detail. In this chapter the bio-inspired kinematics for the experiment will be developed.

4.1 Hover Motions based on the Agrius Convolvuli

The goal is to perform a pitch-plunging motion in a water channel. The kinematics of the experiment are inspired on the kinematics of the hawkmoth.

4.1.1 Coordinate system Agrius Convolvuli

The coordinate system used to describe the motion is shown in Figure 4.1a. Three angles are used to describe the position of the wing [56]: the flapping angle ϕ, the feathering angle α and the elevation angle θ.

The flapping angle is defined as the angle between the normal projection of the leading edge of the wing on the flapping plane and a reference line. The elevation angle is the angle between the leading edge and the stroke plane and can be interpreted as a measure of the out of (stroke) plane movement of the wing. The feathering angle is the angle the chord makes with a line perpendicular to the stroke plane. The elevation and flapping angle are defined positive as shown in Figure 4.1a and the feathering angle, α, is negative in Figure 4.1a.

4.1.2 Hover kinematics Agrius Convolvuli

The kinematics of the Agrius Convolvuli are described by the three kinematic angles. For the hover-case, the time history of these angles is shown in Figure 4.1b [6].

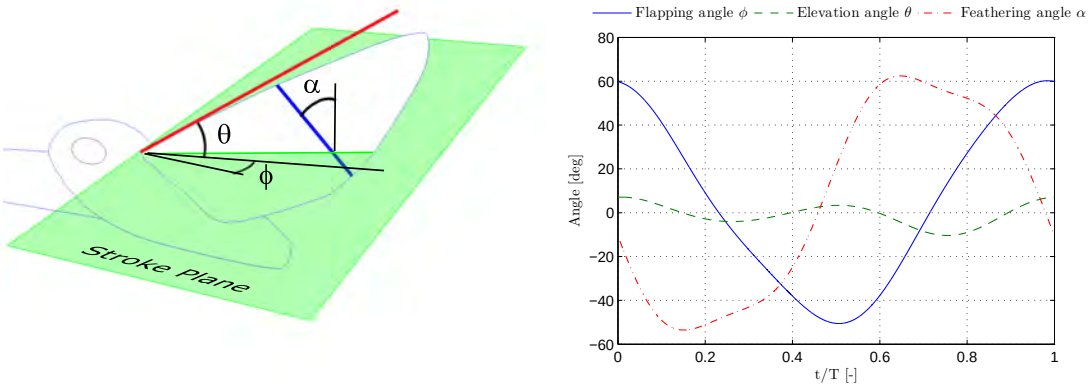

(a) Coordinate system for the motion kinematics

(b) Representation of the kinematic angles

Figure 4.1: Representation of the Agrius Convoluli kinematics

It can be seen that the motions are not perfectly symmetric in shape and that the duration of up and downstroke is different.

4.1.3 Making the motion symmetric

For the present research the three dimensional hover motion of the Agrius Convolvuli is made symmetric in order to convert it to a pure pitch-plunge motion at a later stage. This is done while capturing the most important features during hover, e.g. phase shift of feathering and flapping motions.

Flapping angle

The flapping angle has an average angle of about 4.0°. First the data is shifted to yield a mean angle of 0°. This is justified since this is just a matter of shifting the reference point.

Second, the downstroke duration is 2.3% longer than the upstroke duration, this small difference will be neglected, i.e. the upstroke will be slightly stretched in time to match the downstroke. The resulting angles are shown in Figure 4.2a, observe the small difference between downstroke angle and the upstroke here shown inverted to highlight the differences.

In a last step both half periods are averaged to make the motion completely symmetric, resulting in the averaged flapping angle in Figure 4.2a.

Feathering angle

A similar procedure is applied to the feathering angle. In this case there is no difference in duration of the up and downstroke. The values are shifted by 4.8° to obtain a 0° mean

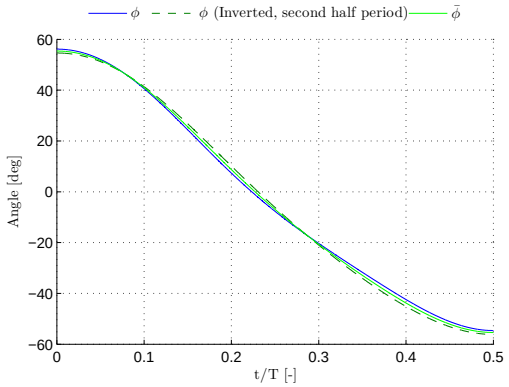

(a) Adjustments of the flapping angle ϕ

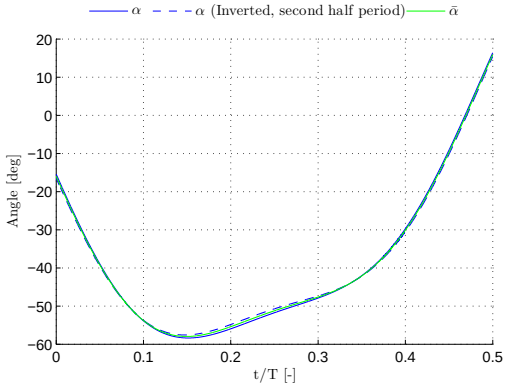

(b) Adjustments of the feathering angle α

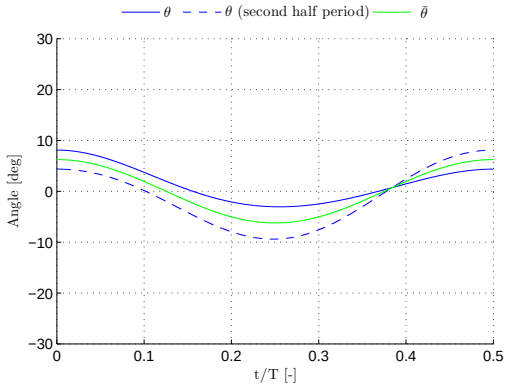

(c) Adjustments of the elevation angle θ

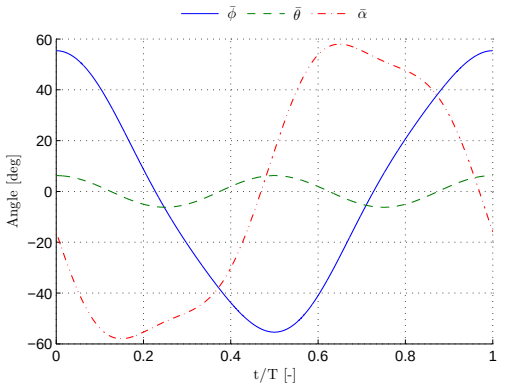

(d) Agrius Convoluli hover kinematics made symmetric

Figure 4.2: Making the motion symmetric

value. After this procedure the feathering angles during upstroke are nearly the same to the angles during downstroke. Both up and downstroke are averaged, the result is shown in Figure 4.2b.

Elevation angle

The elevation angle is also made symmetric, using the same procedure as for the feathering angle. The mean is shifted from about $-1.0°$ to $0°$ and both half periods are then averaged, shown in Figure 4.2c. Note that in Figure 4.2c the y-scale is exactly half of the scale corresponding to Figure 4.2a.

Adjusted kinematic angles

A summary of the resulting, symmetric angles after adjustment is shown in Figure 4.2d.

4.1.4 Hover kinematics experiment

There are a number of different ways to convert the hawkmoth kinematics to the pitch-plunge kinematics for the experiment. The main goal is to preserve the most important features in the conversion from flapping motion to a pure pitch-plunge motion. For instance the phase lag between feathering angle and flapping angle is assumed to be important and has been retained. To examine the effect of other parameters two different motions are investigated.

Ignoring the elevation angle

The first way of determining the kinematics would be to simply ignore the elevation angle and using the feathering angle and the flapping angle.

The flapping angle translates to a plunging motion, $h(t)$, as follows.

$$h(t) = \frac{\bar{\phi}(t)}{\Phi} h_0 \tag{4.1}$$

The pitch angle, $\delta(t)$, is equal to the feathering angle. The rotation axis for this case coincides with the leading edge at the root of the airfoil.

$$\delta(t) = \bar{\alpha}(t) \tag{4.2}$$

Compensating feathering and flapping angle for the loss of elevation angle

Instead of ignoring the elevation angle, it can also be incorporated in the pitch-plunge motion by changing the reference frame, i.e. computing the effective pitch angle relative to the direction of motion. This process is illustrated in Figure 4.3.

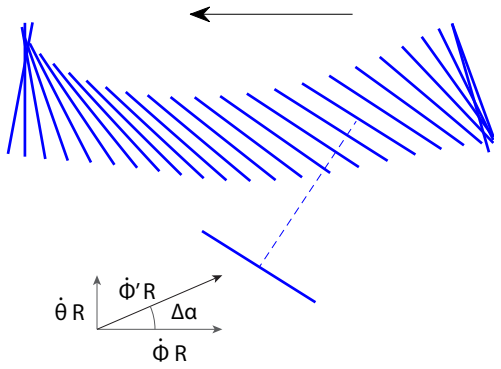

Figure 4.3: Converting a flapping motion to a pitch-plunge motion

The term effective angle in this context is used in a geometric context and is not strictly equal to the incidence angle of the flow. From this geometric perspective the change in pitching angle, $\Delta\alpha$, due to the elevation angle can be quantified as follows.

$$\Delta\alpha = -\arctan\left(\frac{\dot{\bar{\theta}}}{\dot{\bar{\phi}}}\right) \tag{4.3}$$

Yielding equation 4.4 as the expression for the corrected feathering or pitch angle. The variation in time of the pitch angle is plotted in Figure 4.4a. The rotation point coincides with the leading edge.

$$\delta(t) = \bar{\alpha}(t) - \arctan\left(\frac{\dot{\bar{\theta}}(t)}{\dot{\bar{\phi}}(t)}\right) \tag{4.4}$$

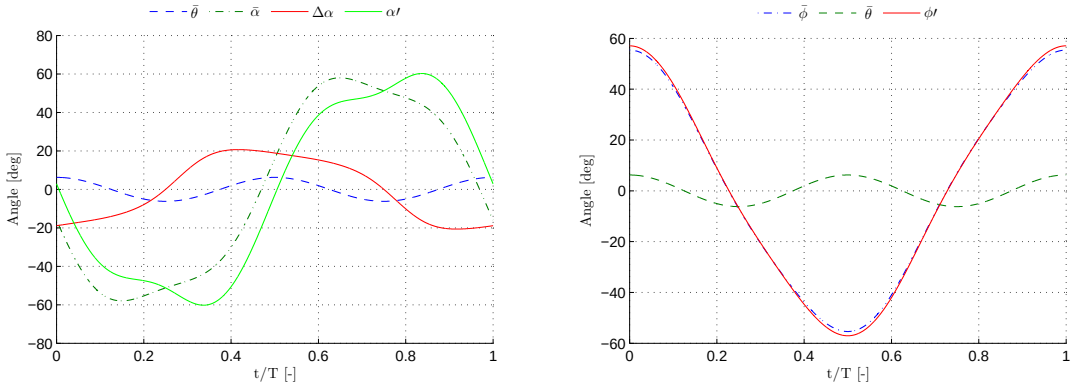

(a) Compensation of the feathering angle for the loss of elevation angle

(b) Compensation of the flapping angle for the loss of elevation angle

Figure 4.4: Compensation for the loss of elevation angle

$$U_{eff} = \pm\sqrt{(\dot{\bar{\theta}}R)^2 + (\dot{\bar{\phi}}R)^2} \tag{4.5}$$

The sign is determined by the sign of the angular flapping speed, $\dot{\phi}$. The effective velocity can be written as $U_{eff} = \dot{\phi}'R$, yielding.

$$\dot{\phi}' = \pm\sqrt{\dot{\bar{\theta}}^2 + \dot{\bar{\phi}}^2} \tag{4.6}$$

Through integration and the correct determination of the integration constant the compensated flapping angle is found, and it is plotted in Figure 4.4b. Converting the elevation angle to an equivalent plunge position $h(t)$.

$$h(t) = \frac{\phi'(t)}{\Phi}h_0 \tag{4.7}$$

4.2 Resulting Kinematics

Three motions result, the first hover motion ignores the loss of elevation angle and simply converts the flapping and feathering angle. Shown in Figure 4.5a. This motion will be referred to as hover motion 1 or HM1.

The second hover motion, Figure 4.5b, incorporates a correction in the flapping and feathering angle for the elevation angle. This motion will be referred to as hover motion 2 or HM2. The correction has an effect on both the pitch and plunging motion. In comparison to the pitch motions, the plunging motions is hardly altered. The difference between HM1 and HM2 is thus dominated by the pitch angle.

As a third reference, a pure sinusoidal motion has been created with the same pitch and plunge amplitude as the basic Agrius Convolvuli kinematics. The sinusoidal kinematics are plotted in Figure 4.5c.

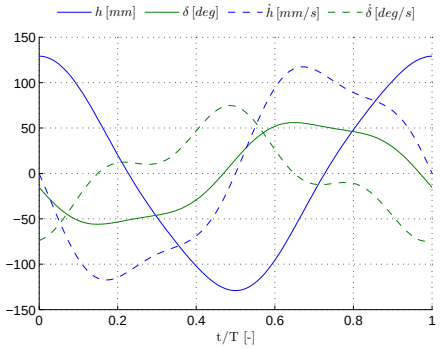

(a) Pitch-plunge hover motion experiment ignoring the loss of elevation angle (hover motion 1)

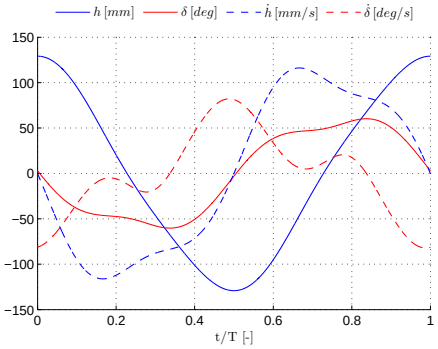

(b) Pitch-plunge hover motion experiment with compensation for the loss of elevation angle (hover motion 2)

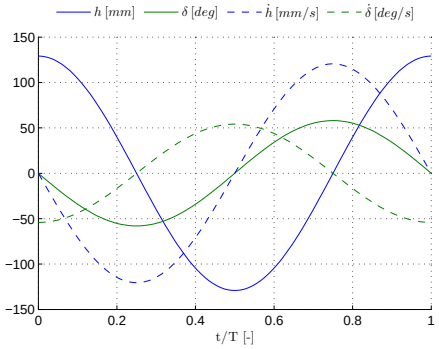

(c) Pure Sinusoidal pitch-plunge motion with the same amplitude and frequency as the Agrius Convolvuli

Figure 4.5: Resulting kinematics pitch-plunge kinematics of the experiments

Chapter 5

Description of the Facilities and Instrumentation

The experiments are performed in The University of Michigan free surface water channel. In this chapter the Facilities, the instrumentation and the methodology will be explained. Particle Image Velocimetry is used to characterize the flow field in two dimensional planes around the airfoil, a load cell is used to measure the force coefficients and the power consumption, and dye flow visualization is used to obtain a qualitative characterization of the three dimensional flow structures around the wing.

5.1 Description of the Flow Facility

The experiments are performed in The University of Michigan free surface water channel. The circulating channel has total volume of about $8,000\,gallons$, and can be seen in Figure 5.1. The test section is made out of transparent float glass, measures 610 by $610\,mm$, and is $2.44\,m$ long. The transparent test section walls facilitate flow visualization and particle image velocimetry experiments. The channel is capable of producing very low turbulence flow, the free turbulence intensity for the possible flow speeds is always less than 1% of the freestream velocity, measured at various flow speeds with Particle Image Velocimetry (PIV). Flow speeds can be varied from 5 to $40\,cm/s$. For this experimental campaign there is no flow in the channel, as we are investigating hover cases.

5.2 Description of the Wing

A Zimmerman wing is used in all experiments; the wing has a chord of $79.4\,mm$ and a span of $241.3\,mm$. The planform shape consists of two ellipses joined at the quarter chord

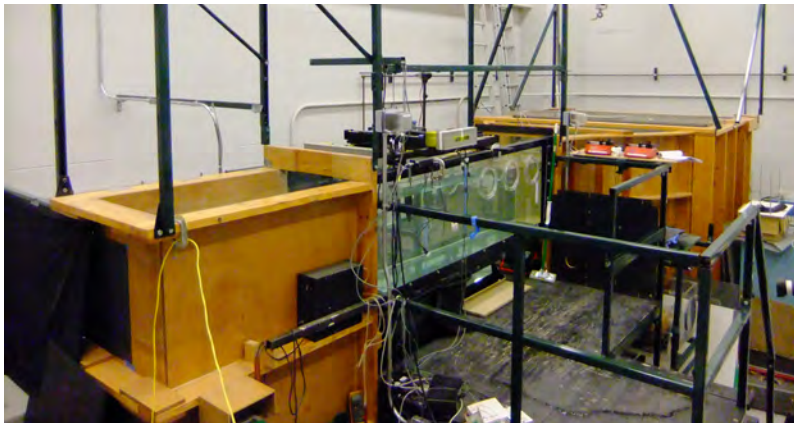

Figure 5.1: Overview of the University of Michigan water channel

of the wing along. The major axes are equal to the span. The minor axes are equal to one quarter and three quarters of the wing chord respectively, cf. Figure 5.2a. The wing planform is laser-cut (PLS6.75, Universal Laser Systems) out of a transparent acrylic plate with a thickness of 2.75 mm. No post-processing is applied and thus the edges of the wing are sharp right angles. The thickness of the wing, 2.75 mm, is substantial and the wing is henceforth assumed to be rigid; during the experiments no deformation of the wing was observed.

The wing is clamped and mounted on a rig with two motors, hanging vertically in the water channel, as shown in Figure 5.2b. The motors are capable of performing pitch-plunge motions with a high degree of accuracy as discussed in the next section.

5.3 Motors and Slides

The kinematics are performed with two stepper motors, sliding systems and gears manufactured by Velmex, inc. For the translation, i.e. the plunge motion, a linear traverse is connected to a PK296-03 two phase stepping motor. The linear traverse consists of two BiSlide positioning slides connected by a belt and pulley system covered by a gray casing shown in Figure 5.3. The translational system is placed perpendicular to the channel walls.

For the pitch motion a rotary table, 4800TS series, is connected to a two phase stepping motor (Vexta PK 266-03B-P2) with a resolution of 1.8 °/$step$. The rotary table is located between the two BiSlide positioning slides, shown in Figure 5.3b. Gears in the rotary table convert the 1.8 °/$step$ to a resolution of 40 $steps/deg$.

5.4 Dye Flow Visualization

To get a qualitative perspective on the flow topology the flow is made visible by adding dye. The dyes used for the experiments are generic red and blue food coloring dyes in-

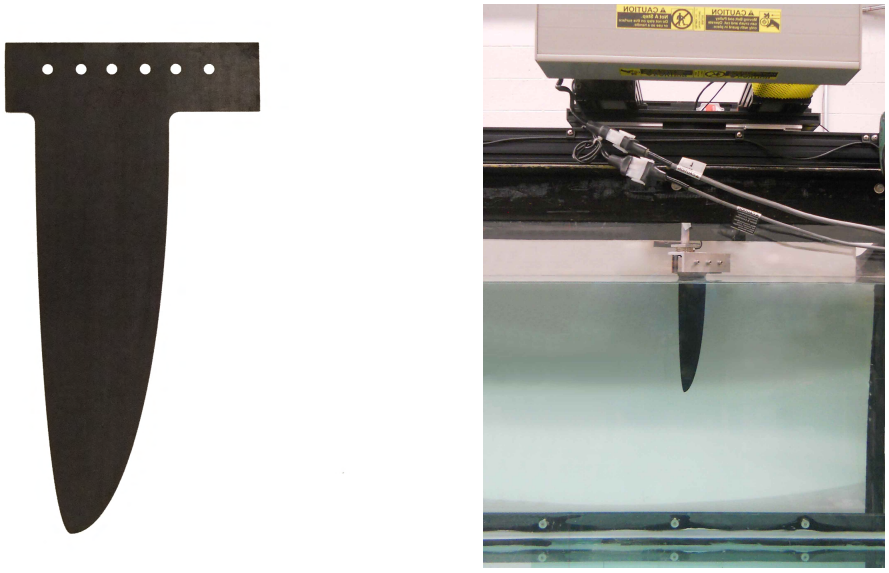

(a) Wing planform

(b) Wing vertically mounted in the water channel

Figure 5.2: Experimental Setup

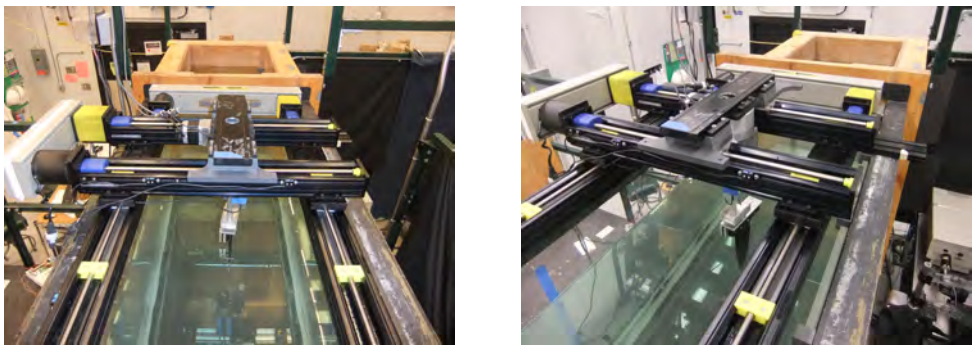

(a) Motor and slide front view

(b) Motor and slide side view

Figure 5.3: Motors and slide configuration

jected by two syringe pumps. The colored dye is injected in the water through a tubing system embedded in the airfoil, Figure 5.4b. Four dye ports are located at the half span and three quarter span position of the leading and trailing edge of the airfoil. A fifth dye port is located at the wing tip. The tubing, embedded in the wing, has an offset closer to one surface of the wing, i.e. the tubing is not located in the middle of the wing with respect to the thickness.

The tip and leading edge is supplied with red dye and the two ports at the trailing edge is fed blue dye. The syringe pumps, model NE-1002X [2], shown in Figure 5.4a, supply the dye at a flow rate of $15\,ml/hr$ for the two blue ports and a rate of $25\,ml/hr$ for the three red ports.

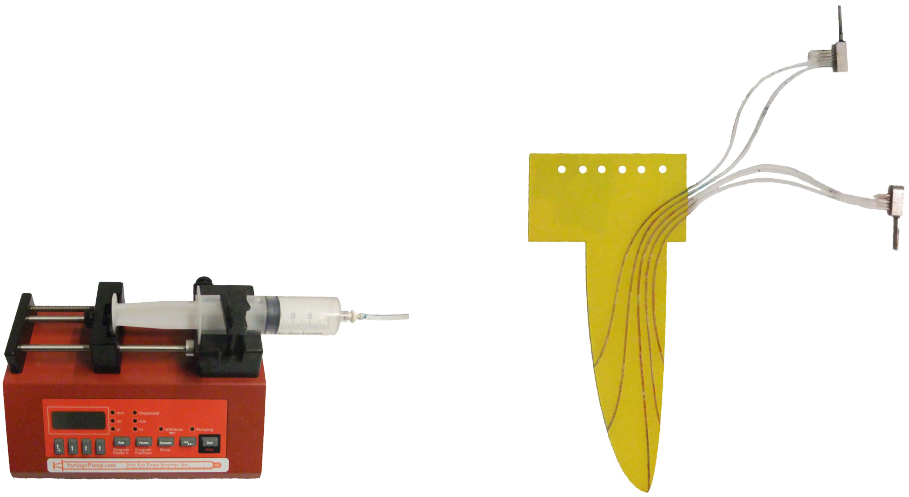

(a) Syringe pump, NE-1002X

(b) Wing with embedded dye injection tubing

Figure 5.4: Flow visualization equipment

Dye injection from ports on the wing is chosen as opposed to a rake system upstream because there is no freestream velocity and since the dye ports are located on the leading and trailing edge vortices are more easily visualized.

The wing clamped in the same bracket as described in Section 5.2 and a white end plate was added. The end plate masked the mounting bracket and provides good contrast with the dye. Two rectangular plates were mounted above for the same reason. These three plates were laser cut (with the PLS6.75, Universal Laser Systems) out of white acrylic.

The wing was lit with high intensity flood lights from below at different angles to minimize reflection and shadows. The dye flow is filmed at a rate of 30 frames per second, in other words there are 202 images per period. An LED, triggered by the motor controller, is used for the synchronization. The signals are set up to light up the LED in the middle of the stroke and shut off at stroke reversal. The LED is positioned such that it is visible in the field of view of the video camera, shown in Figure 5.5a and Figure 5.5b.

The dye injected during the experiments diffuses rapidly, clearly visible in Figure 5.5, therefore the still images of the dye flow visualization are not a useful tool to capture the observations. Still images will be omitted and instead sketches of the most prominent flow features deemed relevant by the observer are provided, an example sketch of the flow field for hover motions at $0.45\,t^*$ is provided in Figure 5.5d. For the enthusiastic reader all still images with the corresponding sketches are provided in Appendix A. The dye flow

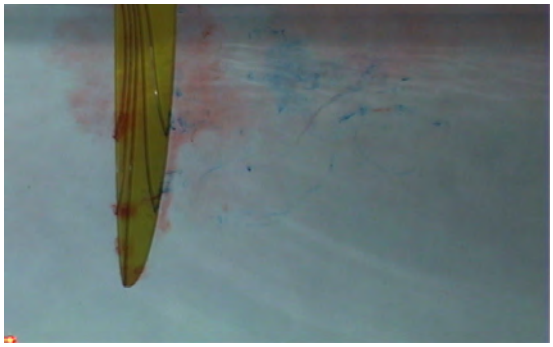

(a) Side view at $t^* = 0.17$

(b) Side view at $t^* = 0.4$

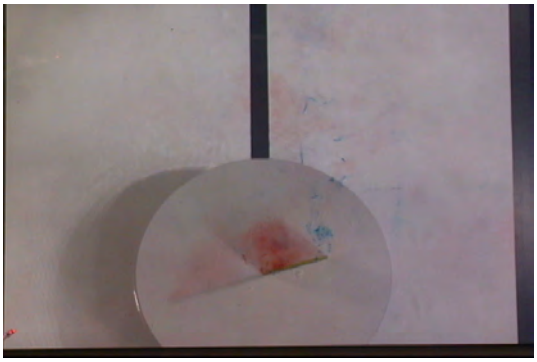

(c) Bottom view at $t^* = 0.45$

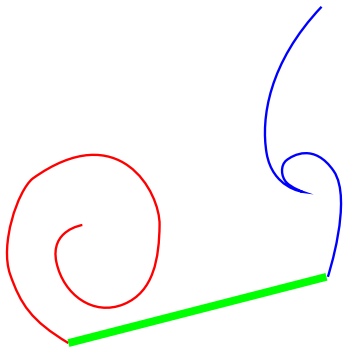

(d) Sketch of the bottom view at $t^* = 0.45$

Figure 5.5: Still images of the flow visualization, hover motion 1

visualization provides a myriad of qualitative information, especially from the moving images in which it is much easier to assess and describe the flow topology.

A few quantitative statements can be made as well, e.g. at stroke reversal there is a spanwise flow from the tip towards the root, since there was no dye present before stroke reversal, the time at which the dye reaches the 75% span position can be determined and a rough estimate for the average speed in that region can be made.

5.5 Force Measurement

5.5.1 Load cell

The force data is acquired using the ATI Mini 40 six-axis force/torque sensor, shown in Figure 5.6. This is a very compact load cell with a diameter of $40\,mm$ and a height of $12\,mm$. The total weight of the sensor is $49.9\,g$. Data is taken in the form of output voltages, the output range of the sensor is $\pm 10V$. Data is sampled at $2000\,Hz$; the high sampling rate ensures the noise can be very well characterized. The sensor is mounted on top of the wing clamp, underneath the rod connected to the rotary stage, cf. Figure

5.2b. The raw sensor data is then calibrated, i.e. converted from Voltages to Newtons and transformed into the correct frame of reference. Using Butterworth low-pass filter the noise can be significantly reduced.

Figure 5.6: ATI Mini 40 force/torque sensor

5.5.2 Data acquisition process

For each kinematic, force data is acquired in 6 separate sets of 25 cycles. The first five cycles are cropped from each measurement eliminating effects of any start up phenomena that might occur. The data is then calibrated and converted to thrust and lateral force components. The thrust is defined as the force perpendicular to the plunge motion, similarly the lateral force is the force component in the plane of the plunge motion.

The thrust and lateral force components are filtered with a low pass Butterworth filter with a cut off frequency of $3\,Hz$. The attenuation properties of the filter are shown in Figure 5.7. To eliminate the phase shift introduced by the filter, it is run over the data back and forth using the MATLAB 'filtfilt'-function. This process ensures zero phase distortion and squares the magnitude of the original filter.

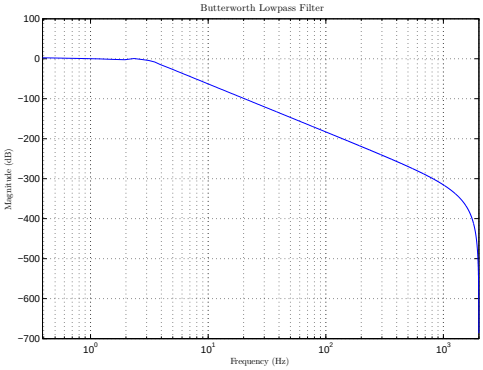

Figure 5.7: Butterworth low pass filter attenuation

Next, the remaining 120 cycles are phase averaged and the sample mean, with the corresponding standard deviation, is calculated. The same procedure is applied to force measurements without the presence of water. This data is used as a tare and subtracted

from the measurements in water.

5.5.3 Non-dimensionalization of the force data

The resulting force data can be non-dimensionalized by the dynamic pressure (based on the reference velocity U_{ref} equal to $4fh_0$, Section 3.2), and the projected wing surface area. The thrust coefficient is then defined as shown in equation 5.1.

$$C_T = \frac{T}{qS} \tag{5.1}$$

Similarly the lateral force coefficient is normalized by the same dynamic pressure and the projected wing surface area.

To obtain a sense of efficiency of the thrust production, the ideal power is calculated using momentum theory [29].

$$P_{ideal} = \sqrt{\frac{T^3}{2\rho A}} \tag{5.2}$$

Where T is the average thrust produced, ρ is the density of the fluid, and A represents the area swept by the wing. The power input can be calculated by multiplying the angular speed with the corresponding moment and the translational velocity with the corresponding force, as shown in equation 5.3.

$$P = F_{lateral}\,\dot{h} + M_z\,\dot{\delta} \tag{5.3}$$

A convenient figure of merit, M, is then defined as follows.

$$M \equiv \frac{P_{ideal}}{P} \tag{5.4}$$

The figure of Merit is used as an indication for the efficiency of the motion.

5.6 Particle Image Velocimetry

In this section the principles and instrumentation of the Particle Image Velocimetry (PIV) setup are explained. In a broad sense PIV is simply the acquisition of two images of particles in a flow with a small time delay. These two images are then cross-correlated to obtain the velocities and its derived quantities. The measurements are indirect, i.e. the velocities are derived from the displacement of the tracer particles and the velocity field of the flow is derived from this. The technique is non-intrusive because the seeding particles have a negligibly small effect on the flow. PIV is also a whole field technique, rather than a point technique, an entire plane in the flow is measured at once.

5.6.1 Basic principles

During the processing of PIV images, the image is evaluated at smaller interrogation windows, technically the windows are two dimensional representations of a volume since the laser sheet has a finite thickness. The displacement of each window is calculated and from this the velocity field is derived.

For the purpose of this research it was chosen to work with two singularly exposure recordings. A constant magnification factor is assumed, i.e. no effects of perspective projection are taken into account. In this way the position of the particle in the image is assumed to be directly correlated to the position in the interrogation volume as sensed by the camera, thus a simple linear conversion can be made to convert the distances in pixels to equivalent distances in meters. Furthermore gravitational forces are assumed to be negligible, and a dispersant was added to the seeding particles to maximize the settling time of the particles.

The theoretical intensity of infinitely small particles captured on a CCD through a perfect lens can be expressed by the square of the first order Bessel function, Bessel functions are canonical (unique) solutions of Bessel's differential equation. The square of the first order Bessel function is also called the Airy function. As a practical approximation for the point spread of particles for non-perfect lenses it is appropriate to assume that the image intensity is Gaussian, $\tau(\mathbf{x})$, as shown in equation 5.5 [32].

$$I = I(\mathbf{x}, \mathbf{\Gamma}) = \tau(\mathbf{x}) \sum_{i=1}^{N} V_0(\mathbf{X_i}) \delta(\mathbf{x} - \mathbf{x_i}) \tag{5.5}$$

Where $\mathbf{x_i}$ is the position vector of the location of the particles with respect to the interrogation window, i.e. a two dimensional position vector. The position vector of the ensemble of all particles is given by $\mathbf{\Gamma}$ and is a function of the position of each particle in three dimensions, $\mathbf{X_i}$, for a given time t. Assuming a constant magnification factor, M, the conversion from $\mathbf{x}$ to $\mathbf{X}$ can be achieved by simply dividing by M and dropping the third dimension. The vector $\tau(\mathbf{x})$ is the Gaussian image intensity for the point spread of a particle for a non perfect lens, assumed to be constant for all particles. Furthermore, $V_0(\mathbf{X_i})$ denotes the transfer function given the light energy of the image of an individual particle i inside the interrogation volume and its conversion into an electronic signal. In many practical cases the light intensity is assumed to be Gaussian across the thickness of the light sheet. Often a weighting factor is added to the transfer function.

Equation 5.5 is often represented in a more compact manner as follows.

$$I(\mathbf{x}, \mathbf{\Gamma}) = \sum_{i=1}^{N} V_0(\mathbf{X_i}) \tau(\mathbf{x} - \mathbf{x_i}) \tag{5.6}$$

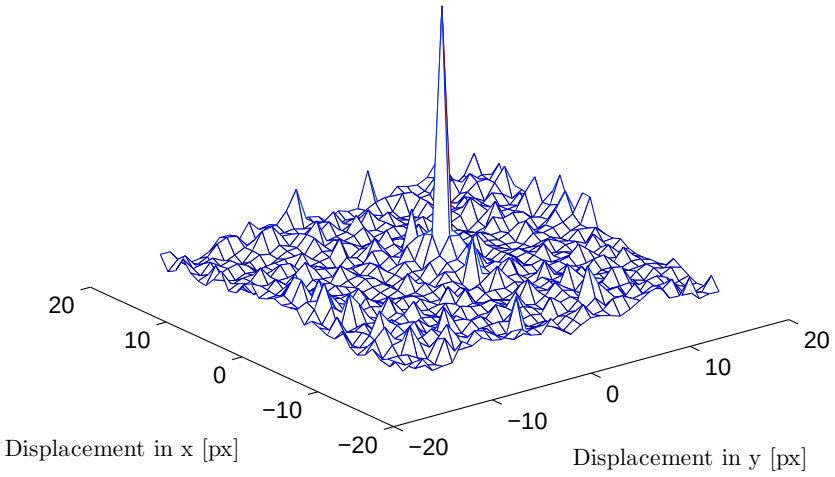

Figure 5.8: The autocorrelation peaks of a 33 by 33 pixel window. The large peak in the center shows that there is no displacement, the correlation with itself ($i = j$), the lower peaks show the correlation with the noise and other particles ($i \neq j$).

Now that we have developed a mathematical way of describing the intensity field of a single exposed image; we can use this notation to describe autocorrelation.

$$R_I(\mathbf{s}, \mathbf{\Gamma}) = \langle I(\mathbf{x}, \mathbf{\Gamma}) I(\mathbf{x} + \mathbf{s}, \mathbf{\Gamma}) \rangle \tag{5.7}$$

$$= \frac{1}{a_I} \int_{a_I} \sum_{i=1}^{N} V_0(\mathbf{X_i}) \tau(\mathbf{x} - \mathbf{x_i}) \sum_{j=1}^{N} V_0(\mathbf{X_i}) \tau(\mathbf{x} - \mathbf{x_i} + \mathbf{s}) d\mathbf{x} \tag{5.8}$$

The correlation of an image with itself is described by equation 5.8, where a_I is the interrogation area and $\mathbf{s}$ is the separation vector in the correlation plane [32]. The equation shows a calculation for the correlation of a particle with itself, $i = j$, and with the noise and other particles, $i \neq j$. An example of autocorrelation of a typical image is given in Figure 5.8. Here a random sample of a PIV image is used and a random interrogation window was placed near the middle of the image. The image was correlated with itself using a fast Fourier transform.

The autocorrelation shows the principle for calculating displacements in a statistical and mathematical fashion. Now we will leverage the same principle to cross-correlate a pair of two singly exposed images, obtained in a flow at a slightly later time. Assuming a constant displacement the particle ensemble, the particle displacement field can be represented as $\mathbf{X'_i} = \mathbf{X_i} + \mathbf{D}$. The intensity of the second image, I', is then defined as follows.

$$I'(\mathbf{x}, \mathbf{\Gamma}) = \sum_{j=1}^{N} V'_0(\mathbf{X_j}) \tau(\mathbf{x} - \mathbf{x_j} - \mathbf{d}) \tag{5.9}$$

Calculating the cross-correlation of these two images we obtain equation 5.10. The full derivation of this equation can be found in reference [32].

$$R_{II}(\mathbf{s}, \mathbf{\Gamma}, \mathbf{D}) = \sum_{i,j} V_0(\mathbf{X_i}) V_0(\mathbf{X_j} + \mathbf{D}) R_\tau(\mathbf{x_i} - \mathbf{x_j} + \mathbf{s} - \mathbf{d}) \tag{5.10}$$

The cross-correlation plane will look very similar to the autocorrelation plane, only now the peak will have shifted from zero to the place where the image has moved to. This can easily be shown mathematically. Considering only the correlation with itself, i.e. when $i = j$, the displacement correlation peak will have a maximum value at $\mathbf{s} = \mathbf{d}$, cf. equation 5.10. This displacement correlation peak yields the in-plane velocity components for this interrogation window.

Equation 5.10 and equation 5.5 provide us with the tools to describe mathematically what the images look like and what the cross-correlation is. In a next step we obtain these functions using statistical mathematical tools. Initially a form of particle tracking was performed manually by linking each particle to its equivalent on the second image. This technique is very time consuming and only suited for sparse seeding. In a later stage computers took over particle tracking. Due to the need for more and more data points the seeding needed to be increased, to deal with this higher seeding density the aforementioned statistical tools were developed.

Instead of direct calculation the cross-correlation theorem is leveraged. The theorem states that the cross-correlation of two functions is equivalent to a complex conjugate multiplication of their Fourier transforms. In the last decades Fourier transforms are easily and rapidly calculated using Fast Fourier Transform (FFT) algorithms, and similarly for its inverse. Hence FFT algorithms are used to find the cross correlation of two PIV images.

This is the mathematical basis on which modern PIV techniques are based. In the next section the instrumentation of the PIV setup will be described.

5.6.2 Instrumentation

The Particle Image Velocimetry (PIV) setup consists of a pulsed Nd:YAG laser (Spectra-Physics PIV-300), an optical setup to form the laser sheet, an external timing system (a BNC 555 pulse delay generator and the Stanford Research Systems' DG535) a high resolution 14bit cooled CCD camera system (Cooke, PCO4000) with a Nikon Micro-NIKKOR 105 mm lens. The camera has a sensor of 4008 by 2672 pixels. The flow is seeded with Titanium(IV) oxide, rutile powder.

Nd:YAG laser

Lasers (Light Amplification by Stimulated Emission of Radiation) leverage the fact that atoms can be exited to a higher level of energy by absorbing energy, e.g. kinetic energy, light. Conversely they can also loose energy through these phenomena. In a laser, the exited atoms are stimulated to decay by interaction with photons with a certain frequency; in this process light will be emitted in the same direction, phase, and frequency as the incident light.

The Particle Image Velocimetry (PIV) setup contains a pulsed Nd:YAG laser (Spectra-Physics PIV-300). The laser has two oscillator cavities. These independent oscillator cavities ensure almost infinitely variable pulse separation times, while maintaining constant output energy. Both output beams have the same phase, direction, and amplitude. The light is intense and monochromatic with a wavelength of $1064\,nm$. The system uses a Type II potassium dideuterium phosphate (KD*P) crystal in the harmonic generator to change the wavelength to the visible green spectrum, i.e. $532\,nm$.

Nd:YAG is an acronym for neodymium-doped yttrium aluminum garnet, the excitation medium for the laser. Nd:YAG has more than three energy states, thus a population inversion is possible, i.e. a state is possible in which the number of atoms in a higher, excited state is higher than the number of atoms in a lower, ground state.

The excitation medium is optically pumped by a krypton flash lamp. Leaving the Q-switch out of consideration for the moment, each time the flash lamp fires, the laser is fired, the power output is moderate and relatively long, the same order of magnitude as the firing time of the flash lamp. This is equivalent to operate the laser in "long pulse" mode.

To increase the power output peak (and shortening the pulse length) a Q-switch is implemented. As first implemented by McClung et. al. [28], the Q-switch introduces a high cavity loss to prevent oscillation. When the oscillation is prevented the population inversion can grow to a high steady state value. As soon as this state is reached the Q-switch can be switched to a low loss and the laser will send out a 2- $7\,ns$, high intensity pulse ($> 100\,mJ$) [42, 43].

The laser light is guided through an optical setup to form the laser sheet. The optical setup consists of a series of mirrors, followed by a spherical lens to refocus the laser light. Subsequently the light goes through a cylindrical lens that transforms the laser beam into a sheet of light.

External timing system

An external timing system is used to synchronize the wing motion, the camera and the laser. All trigger signals are generated by a BNC 555 pulse-delay generator, the delay

between the motion trigger and the laser pulse is governed by the Stanford Research Systems' DG535. All signals come together at a data box that was manufactured in house. To ensure that the synchronization is running smoothly all signals are read out on a computer and a MATLAB script is used to verify all timing conditions are met.

Camera and optics

The images are obtained with a high resolution 14bit cooled CCD camera system (Cooke, PCO4000) with a Nikon Micro-NIKKOR 105 mm lens. The camera has a sensor of 4008 by 2672 pixels.

The aperture of the camera, opening size of the diaphragm, determines to a large extent how much light the CCD will be exposed to. The larger the size of the aperture the more light the CCD will be exposed to. In general f-stops are used to denote the aperture, f-stops are a series of standard opening sizes, in this series the area of the aperture doubles every step [12]. For the PIV experiments, a setting of $f/8$ was found to be adequate.

The aperture also controls the depth of field; this is the region in which the image is acceptably sharp or, in other words, in focus. The smaller the aperture the larger the depth of field, a more extreme example of this is the pinhole camera. In a pinhole camera the size of the aperture is very small and the entire image is reasonably sharp. To obtain an image with aperture sizes this small, long exposure times are needed.

Therefore the shutter speed also influences diaphragm f/number, longer exposure times will be needed to get the same exposure for a smaller diaphragm opening. Exposure time and aperture opening can be assumed to scale linearly. In case of the PIV experiments the exposure is dictated by the laser pulse energy and duration which are 100 mJ and 2 - 7 ns respectively, and the aperture needs to be adjusted accordingly.

Seeding

The seeding particles have to fulfill a number of criteria. First, the particles should trace the flow as close as possible to get an accurate velocity field. Second, the particles should scatter a sufficient amount of light to get clear images, i.e. they need to be distinguishable from the flow medium.

The water is seeded with Titanium(IV) oxide, rutile powder with a diameter of approximately 5 micrometer. The titanium particles are added to a beaker of water containing a small amount of the dispersant. The dispersant, ammonium polymethacrylate (DARVAN C-N), is added to facilitate the suspension of the particles for longer periods of time. The mixture is stirred with a magnetic stirrer. To avoid clotting the particle mixture is treated with a sonicator, ultrasonic processor Q700 (Qsonica, LLC). The mixture is then added to the water channel at a high flow rate to ensure good mixing of the particles with the

flow medium.

Setup

PIV images are taken in two different planes parallel to the water surface. For the PIV data acquisition at both planes, a similar setup is used.

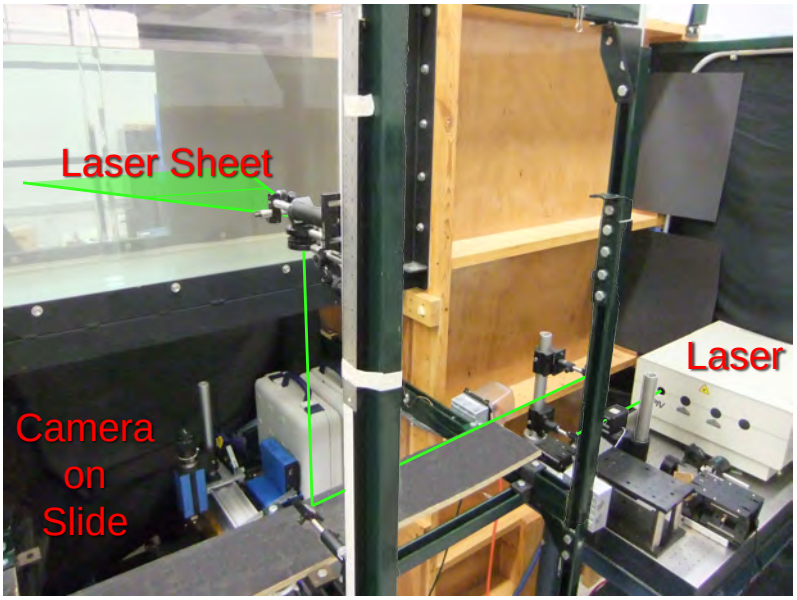

Figure 5.9: Representation of the PIV setup parallel to the water surface

In setup the laser sheet is horizontal, parallel to the water surface, and the camera is underneath looking up, cf. Figure 5.9.

The plunge amplitude is about 130 mm, to get a good resolution three camera positions are used and the data is stitched together during post-processing. The camera is mounted on a slide and shifted to 3 positions that have an overlap region. The stitching procedure, illustrated in Figure 5.10, is completely discrete in order to make sure that discrepancies between images would be spotted visually. The camera lens is focused to produce a magnification of approximately 14 pixels per mm. Using this technique a field of view of 6225 by 3525 pixels (or 437 by 247 mm) is obtained, capturing the entire plunge motion.

The laser sheet is moved to two positions, 50 % span and 75 % span position respectively. The images at 75 % span are expected to be influenced by the tip vortex to a large extend. Conversely, the images at half span are expected to be closer to the two-dimensional solution.

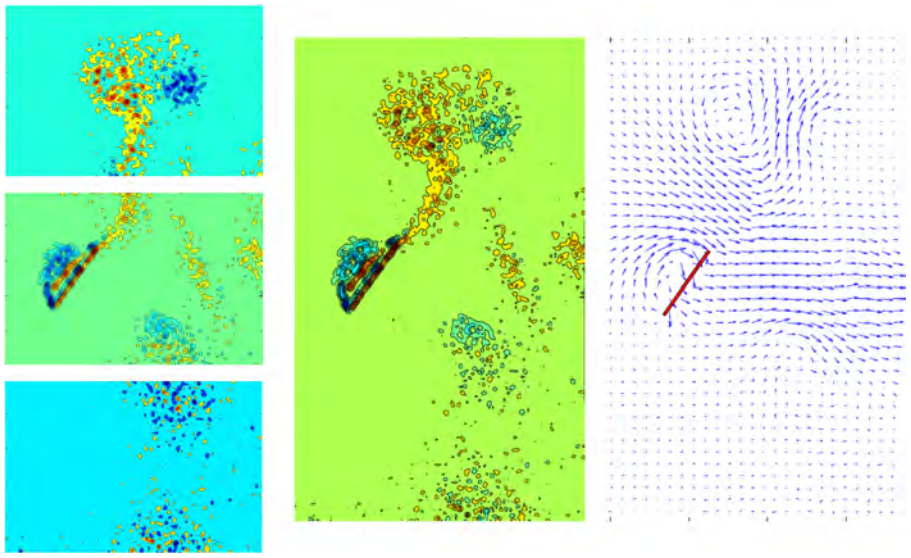

Figure 5.10: Stitching procedure for the horizontal PIV setup. Left, three independently obtained vorticity data plots, middle, the three vorticity plots stitched discretely, right, the corresponding velocity vectors for the discretely stitched data

5.6.3 Post-processing

The post-processing is performed in MATLAB and can be roughly divided into five steps. The first step consists of a preliminary verification of the data and choosing the processing parameters accordingly. In this case the grid size was determined to be 150 by 100 grid points with 25 px spacing between grid points. The second step serves as a validation step of the data, in this step outliers are detected and removed. Third, incorrect data points are replaced by using the mean of the surrounding points to decrease the error when calculating derived quantities such as vorticity. Phase averaging of the data is done in the fourth step. An image of the same phase is taken a hundred times; these one hundred images are all used to obtain a result that is statistically sounder. The flow is highly unsteady and no two cycles will be exactly the same, and averaged over one hundred images the flow does exhibit consistent flow features. The last step of the post-processing consists of the analysis of the information, computation, normalization, and plotting of the vorticity, drawing the appropriate streamlines.

For all vorticity plots the vorticity is normalized with the reference velocity, the average tip speed, and the mean chord, shown in equation 5.11.

$$\bar{\omega} = \frac{\omega\, c}{U_{ref}} \tag{5.11}$$

In the middle of the vorticity plots the thrust and lateral force coefficients are plotted, vertical lines in this plot depict the phases, labeled a through f, at which the PIV images are taken (e.g. Figure 6.9).

In the velocity plots, the magnitude of the vectors is only to scale with the other vectors in the same plot. To give an estimate of the magnitude the maximum velocity for each vertical line of vectors is given at the bottom of each plot. The maximum measured velocity is normalized by the reference velocity, as depicted in equation 5.12.

$$\bar{v} = \frac{v}{U_{ref}} \tag{5.12}$$

The axes in all plots show the distance in mean chords, with zero being the position of the leading edge at half span and the mid position of the plunge motion. Note that the chord length at half span is larger than the mean chord length. The plots are ordered chronologically from left to right, top to bottom. In all figures the airfoil is plunging downwards or the plunge velocity is zero and the leading edge points to the left side of the figure.

5.6.4 Accuracy and error characterization

The measurement error can be characterized in two ways. One approach is to split the error into systematic errors, i.e. errors due to the statistical methods used, and residual errors, i.e. due to the measurement uncertainty. A second approach is to characterize the error as the sum of the bias error and the random error. The bias error is an over- or underestimation of the actual velocity and the random error is added to that to obtain the actual measurement error [32].

To obtain an estimate of the random error we can measure a known flow, since we are investigating a hover case a good baseline is to measure the velocity of the static fluid, i.e. a quiescent flow. The measurements were made on a modest dataset of 5 images, compared to 100 for the experiments. The resulting velocity on the two middle axes of the grid are shown in Figure 5.11. It can be seen that the velocity remains very small in all positions and all directions with mean velocity (for the entire field, not just the axes) of $0.0120\,px/\Delta t$, the standard deviation is $0.0391\,px/\Delta t$. In other words the velocity is nearly zero as expected, and the standard deviation in this case is roughly 4 times the velocity measured. In these experiments there was no spatial shift, i.e. only system noise.

For minimization of the RMS fluctuation the seeding density needs to be at least 10 - 20 particles per interrogation window. Increased seeding decreases the uncertainty because more particle pairs are taken into account. The RMS is also a function of the displacement of the particles. For increasing spatial shift the RMS value increases, but not linearly. Conversely the relative error decreases with increasing displacements [55].

The spatial resolution is limited by the particle seeding density. In the experiments, including the quiescent flow, the seeding density is about 30-40 pixels per interrogation window.

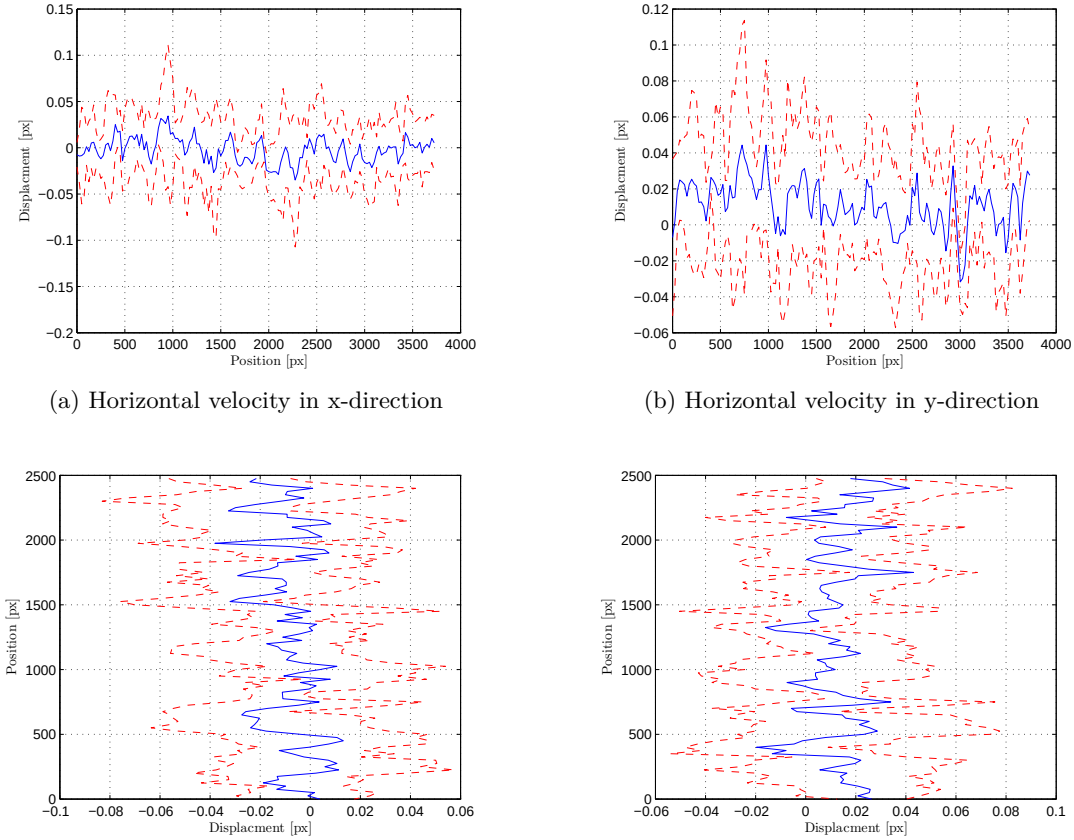

(a) Horizontal velocity in x-direction

(b) Horizontal velocity in y-direction

(c) Vertical velocity in x-direction

(d) Vertical velocity in y-direction

Figure 5.11: Typical velocity (blue) and standard deviation (red) for a vertical and a horizontal line in a quiescent flow, averaged over 5 images

The interrogation window takes the ensemble average of the displacements measured for that region and acts as a low-pass spatial filter. In this way wavelengths smaller than one window size are suppressed, the cut off frequency of this 'filter' is twice the size of the window (Nyquist).

A smaller window increases the cut-off frequency of the filtering due to the interrogation window and will also increase uncertainty of the measurement. The increase of uncertainty is a result of the greater probability of particles entering or leaving the interrogation window between exposures and the decrease in particle pairs for same seeding density.

The correlation peak always covers more than one pixel; the PIV software leverages this by fitting a curve to estimate the displacement. However most of the fitting schemes are biased towards an integer value for the displacement, this effect is called 'peak locking'. To avoid this effect one can take multiple measures. The most efficient measure is to ensure that the particle size is larger than $2\,pixels$. If the particle size is smaller, pre-processing procedures can be applied to mitigate the effects. A pre-processing routine

can be applied to increase particle size using filters, e.g. increasing the contrast of the image and applying a blurring filter. Assuming the small particle size is noticed during the experiments, one can defocus the camera to optically enlarge the particle size on the image. This method will reduce the contrast of the image and hence introduce some random noise in the system. The choice of peak estimator also has an effect on peak locking; if the particle size is smaller it is better to choose a peak estimator that is better suited for smaller particles. Furthermore an equalization scheme of the displacement histogram can be used to reduce the error of peak locking [35].

A histogram of the displacement for a typical PIV image pair taken during the experiments is shown in Figure 5.12, no peak locking was observed.

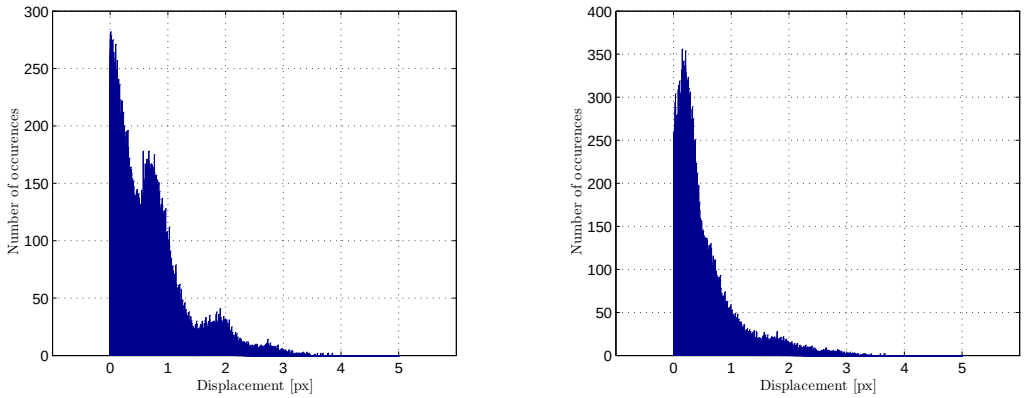

(a) Pixel displacement in x-direction

(b) Pixel displacement in y-direction

Figure 5.12: Typical histograms of the PIV displacement data in pixels.

The interrogation window has a finite size, and in order to perform a Fourier transform we need to integrate from $-\infty$ to $+\infty$. To fulfill this requirement the signal is assumed to be periodic. This assumption means that the correlation will also be periodic, therefore aliasing can occur. Consider an interrogation window with dimensions N by N and a displacement of more than $N/2$. In this case the displacement peak will be folded back into the correlation plane on the opposite side of the original displacement, this effect is called aliasing. It is crucial that the combination of the interrogation window size and the time between exposures is chosen such that no aliasing will occur.

The more the image is displaced the smaller the correlation peak will be, because of the proportional decrease in possible particle matches. This effect is called the displacement range limitation. A practical and conservative measure is to make sure the displacement is less than $N/4$.

Chapter 6

Results

In Chapter 3 and 4 dynamic scaling was discussed and the kinematics of the hawkmoth were converted to pitch-plunge motions. In this chapter the aerodynamic effect of the kinematics will be analyzed at length. The basic motions are discussed using particle image velocimetry, aerodynamic force measurements, and flow visualization. And they serve as a basis for comparison when expanding the parameter space by changing the reduced frequency and adding phase lag.

6.1 Test Matrix

The experiments can be performed at various Reynolds numbers and reduced frequencies. As an initial base condition the values of the hawkmoth are used, i.e. a reduced frequency of 0.38 and a Reynolds number of 4800. Both parameter values are based on the average velocity at the three quarter span location.

Next it is also investigated how an increase in reduced frequency affects aerodynamic force generation. There are some practical limitations to what can be achieved in a water channel. The maximum and minimum values for the reduced frequency are predetermined by the limits in acceleration and speed of the motor, and by the channel width. The channel width limits the maximum amplitude of the motion and hence the minimum achievable reduced frequency, as shown in equation 6.1.

$$k = \frac{\pi c f}{U_{ref}} = \frac{\pi c f}{4 f h_0} = \frac{\pi c}{4 h_0} \tag{6.1}$$

Since the chord is kept constant in these experiments we can rewrite equation 6.1 as follows.

$$k \propto \frac{1}{h_0} \tag{6.2}$$

Table 6.1: Independent variations of the parameters

k	0.38	0.7	
Phase lag	-10%	0%	-10%

Equation 6.2 shows that the reduced frequency of the experiment is only proportional to the inverse of the amplitude.

At the same time to keep similarity between the experiments the Reynolds number needs to be kept constant as well. The Reynolds number in this case is defined as follows.

$$Re = \frac{U_{ref}c}{\nu} = \frac{4fh_0c}{\nu} \tag{6.3}$$

Since the chord is kept constant, the Reynolds number is only proportional to the product of the frequency and the amplitude.

$$Re \propto fh_0 \tag{6.4}$$

In other words, when increasing the reduced frequency the decrease in amplitude must be compensated by an increase in the motion frequency. This maximum frequency is limited by the maximum acceleration and maximum speed of the motors. In this case the reduced frequency of the hawkmoth, $k = 0.38$, is relatively close to the lower limit, and the upper limit corresponds with a reduced frequency of 0.7. These two points will be two measurement points for all three kinematics.

A second variation will be the effect of phase lag between the pitch and the plunge motion. The difference in phase between the pitch and the plunge will be expressed as percentages of the period. The lag introduced is $\pm 10\%$ of the period.

The parameter space is explored through the variation of one parameter independently of the others, i.e. starting from the base point the reduced frequency is changed and starting from the base point the phase lag is introduced. In this study coupling effects between parameters will not be assessed. A summary of the test matrix is provided in Table 6.1, note that the Reynolds number has been kept constant throughout.

6.2 Baseline Bio-Inspired Kinematics

The baseline kinematics are studied extensively and a detailed account will be provided in this section. The data provided in this section will also serve as a basis for comparison when expanding the parameter space.

6.2.1 Force coefficients

In this section the resulting force coefficients of the base motions, described in Section 4.1.4, are presented. Figure 6.1 illustrates the force magnitude and direction for the three cases considered in this study. Also shown in this figure are the wing location and the orientation for each force value shown in the figure.

For hover motion one, the thrust coefficient, as shown in Figure 6.2a, peaks at 4.7. The peak occurs at $t^* = 0.2$ just after the pitch angle and the plunge speed reach their maximum value. The average thrust coefficient is 2.79. The non-dimensionalized standard deviation of the mean varies between 0.60 and 0.17 or between 4% and 13% of the maximum thrust. The average of the absolute value of the lateral force coefficient is 3.00, as shown in Figure 6.2d. The lateral force coefficient increases fairly rapid and varies around a value larger than the average. Three local maxima exist 3.2, 3.3 and 4.8 respectively. The figure of merit for this motion is 0.47.

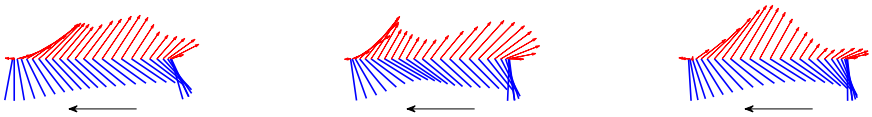

(a) Hover motion 1 (b) Hover motion 2 (c) Sinusoidal motion

Figure 6.1: Visualization of the three kinematics (blue lines) and the generated forces (red vectors)

Two peaks exist in the thrust coefficient for hover motion two, 4.4 and 4.8 respectively. The location of the first maximum occurs at $t^* = 0.15$ and the second maximum occurs at 41 percent of the period. The local minima occur at the end of the stroke and right in the middle, at $t^* = 0.25$, their values are -0.06 and 2.12. The average thrust coefficient is 2.64. The non-dimensionalized standard deviation of the mean varies between 0.43 and 0.19 or less then 10% of the maximum thrust coefficient. The absolute value of the lateral force coefficient averages at 2.98, the shape consist of two peaks with a local minimum in between. The peaks are located at 0.1 and $t^* = 0.43$ with values of 4.22 and 4.45. The figure of merit equals 0.48.

The sine motion thrust coefficient also has two peaks, the first peak is relatively small (about 1.2) and the second peak is substantially larger, 6.11 at $t^* = 0.32$. The average thrust coefficient is 2.39. The standard deviation of the mean varies between 0.67 and 0.21 or between 3 and 11% of the maximum thrust coefficient. The absolute lateral force coefficient averages at 2.39. Resulting in a figure of merit of 0.49.

The force on the wing is primarily perpendicular to the airfoil, this is also implied in Figure 6.2, where the pitch angle is zero the thrust force is also zero. By means of com-

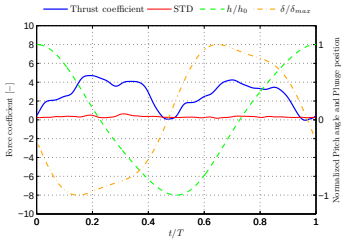

(a) Thrust coefficient hover motion 1

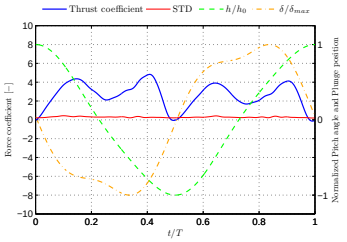

(b) Thrust coefficient hover motion 2

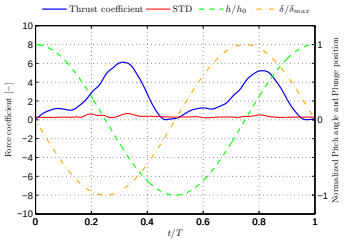

(c) Thrust coefficient pure sinusoidal motion

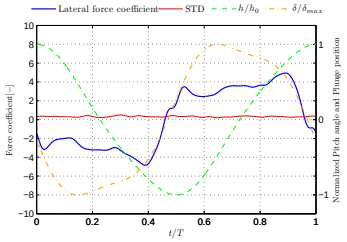

(d) Lateral force coefficient hover motion 1

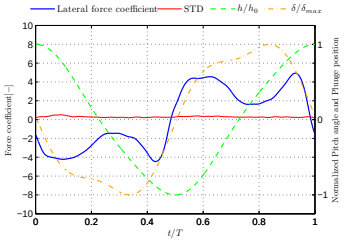

(e) Lateral force coefficient hover motion 2

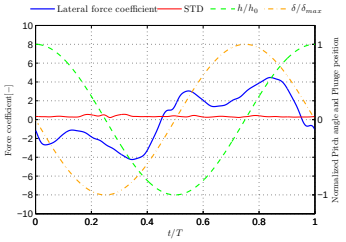

(f) Lateral force coefficient pure sinusoidal motion

Figure 6.2: Hover motions force coefficients

parison all force coefficients of the different motions are plotted in Figure 6.3. The average coefficients are tabulated in Table 6.2. It can be concluded that the figures of merit are all in the same order of magnitude. HM1 produces the most thrust, about 6% more than HM2 and 17% more than the pure sinusoidal motion. As expected, for all motions the average lateral force coefficient (in absolute values) is of the same order of magnitude as the average thrust coefficient.

Assuming a number of hawkmoths variable in weight and size [27, 37, 54] the average thrust coefficient needed for hover would be around 0.88 to 1.01 (using the average velocity at 75% span position). The thrust coefficients for the motions in the experiment calculated using equation 5.1 are 2.79, 2.64 and 2.39 respectively, which is of the same order of magnitude. There are several factors increasing the thrust coefficient of the pitch-plunge motion compared to the flapping motion. The speed of the wing at the root is not zero, leading to a large contribution to the force since at the root the chord is the largest. The average speed over the airfoil is larger since it moves in its entirety, rather than just flapping. And last the swept area is larger for the pitch-plunging motion compared to the flapping motion.

6.2.2 Dye flow visualization

The dye injection is performed as described in Section 5.4. Since the dye diffuses rapidly, still images will not be used to illustrate the observations. Instead sketches will be shown

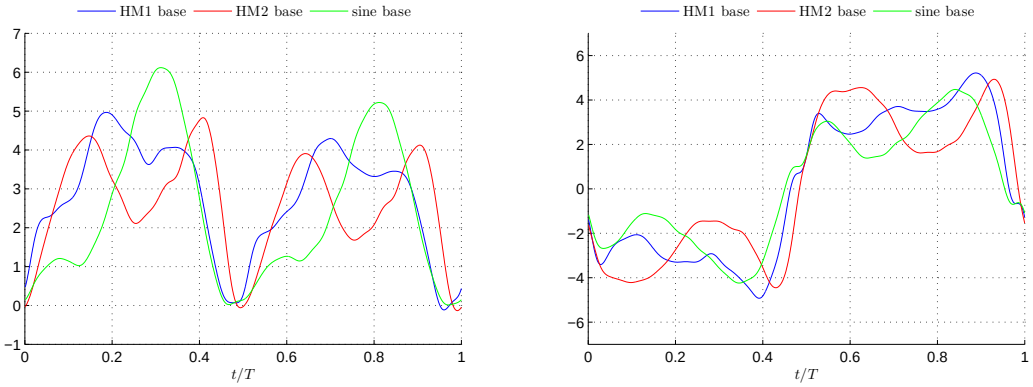

(a) Thrust coefficient

(b) Lateral force coefficient

Figure 6.3: Base motion force coefficients

Table 6.2: Base motion average force coefficients

	HM1	HM2	Sine
C_T	2.79	2.64	2.39
$\|C_{Lateral}\|$	3.00	2.98	2.39
M	0.47	0.48	0.49

to illustrate the most prominent flow features observed. In all figures the airfoil is plunging downwards or the plunge velocity is zero and the leading edge points to the left side of the figure.

The hover motion starts by moving through the dye from the previous stroke, $t^* = 0.0 - 0.1$. The dye cloud from the previous stroke, during this time period, is nearly stationary compared to the airfoil and no rotating flow or distinct movement of the flow is observed. At $t^* = 0.17$, shown in Figure 5.5a and sketched in Figure 6.4a, a small vortex is observed a little aft from the leading edge. A distinct starting vortex has also been shed from the trailing edge due to the onset of the translation. The side view of this phase reveals no significant spanwise flow at the half and three quarter span positions. Conversely at the tip two dye streams were observed. The first is flowing aft and upward; it is unclear whether this is vortical flow or a merely dye diffusion, i.e. no conclusions can be made regarding the existence of a tip vortex at this point. The second flow is moving straight up and seems to be spinning in the same direction as the leading edge vortex. Since there is no dye on that side of the airfoil in the first few frames of this stroke, a qualitative measurement can be made regarding the average spanwise velocity component of the dye between the tip and the three quarter span position. The average speed is estimated to be $60\,mm/s$ or $0.78\,U_{ref}$. Note that this is an average velocity and evidence suggests that the dye is accelerating during this period, resulting in higher spanwise velocity components.

As the stroke continues and the flow develops further, the dye at the trailing edges starts

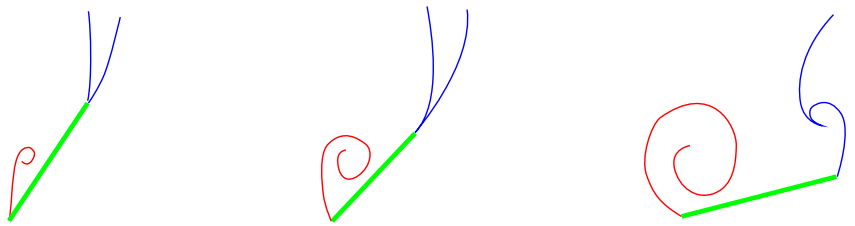

(a) $t^* = 0.17$ (b) $t^* = 0.3$ (c) $t^* = 0.45$

Figure 6.4: Sketch of the most prominent features observed in the flow visualization, hover motion 1

pointing aft and upwards. Spanwise flow is observed across the leading edge (excluding the position from the root to quarter span, since no dye is present in this region). No quantitative statements about the spanwise flow can be made at this point since the dye is diffused across the entire region. The size of the leading edge vortex is growing and the core moves further away from the airfoil.

A distinct difference between the trailing edge flow at half span and three quarter span is observed. The sketch in Figure 6.4b clearly shows that the dye coming from the trailing edge dye port at the half span position is further downstream than the dye originating from the three quarter span position. This indicates there is more momentum in the aft direction originating from the half span position, which is expected since the chord is larger at that location and there are less three dimensional effects that would diminish the thrust compared to the three quarter span position.

Close to the wing surface, at $t^* = 0.4$, there is a portion of the dye originating from the trailing edge moving toward the leading edge visible in Figure 5.5b. At stroke reversal there is a trailing edge vortex forming due to the rapid rotation (supination) of the airfoil, the vortex formation starts approximately at $t^* = 0.35$. The vortex is sketched in Figure 6.4c and visible in the still image of the flow visualization, Figure 5.5c. At this point there is a large, diffuse and rotating flow present from the leading edge to roughly the three quarter chord position.

The wake of the airfoil is clearly contracting in the spanwise direction, the contraction is estimated to be 1 to 2 chord lengths over a distance of 2 chord lengths downstream. In the plunging direction no distinct contraction is observed. The speed of the wake moving downstream is estimated to be between 1 and 2 chord lengths per stroke.

The flow development for hover motion 2 is significantly different from hover motion 1. Early in the stroke, at $t^* = 0.08$, the first indication of a starting vortex is observed in the trailing edge region. The trailing edge vortex is stationary in the next few frames and a leading edge vortex starts developing at $t^* = 0.11$. Simultaneously the flow at the tip splits into two directions, one upward and aft, and the other upwards, conjoined with the LEV. The average speed of the spanwise flow originating from the tip is about $56\,mm/s$

or $0.73\,U_{ref}$. The flow at three quarters of the span remains stationary until $t^* = 0.2$. At this point the features are very similar to the features observed in hover motion 1 depicted in Figure 6.4a.

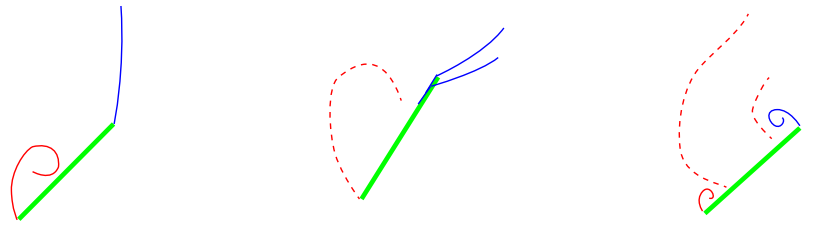

(a) $t^* = 0.20$ (b) $t^* = 0.34$ (c) $t^* = 0.42$

Figure 6.5: Sketch of the most prominent features observed in the flow visualization, hover motion 2

The leading edge vortex seems to grow slightly and start moving aft, i.e. it seems to be separating. The LEV has moved significantly aft by $t^* = 0.26$ and at this point the measured normal force is at its lowest. After this point in time there is some flow from the trailing edge towards the leading edge. The inward flow toward the leading edge has a significant spanwise component towards the leading edge at the three quarter span position. At $t^* = 0.34$ the LEV has separated from the airfoil and the resulting flow pattern is sketched in Figure 6.5b.

The supination starts and a trailing edge vortex is formed due to the rotation. At $t^* = 0.42$ the first evidence of the formation of a second LEV is seen, Figure 6.5c. In between the dashed lines of the sketch the dye is very diffused and with no distinguishable flow patterns.

From the side perspective a large upward and aft flow is observed originating from the trailing edge at the half span position around stroke reversal from $t^* = 0.43$ to 0.56. The average vertical velocity component is estimated to be about $130\,mm/s$ or $1.7\,U_{ref}$. The wake in the span direction contracts by the same order of magnitude as the wake from HM1, about 1 to 2 chord lengths over a distance of 2 chord lengths downstream.

The flow around the sine motion is a much simpler compared to the bio-inspired motions. The leading edge vortex remains attached throughout the stroke and there is only the formation of one trailing edge vortex (a starting vortex). The earliest onset of the formation of the LEV was observed at $t^* = 0.14$ and is sketched in Figure 6.6a. This is right after the depression in the normal force at $t^* = 0.13$. The trailing edge vortex is very faint in comparison to the bio-inspired motions.

The leading edge vortex keeps developing into a larger flow structure and seems to grow in strength. The dye from the ports at three quarter and half span position on the leading edge remains stationary till $t^* = 0.2$. The average spanwise velocity component from the

(a) $t^* = 0.14$ (b) $t^* = 0.3$

Figure 6.6: Sketch of the most prominent features observed in the flow visualization, pure sinusoidal motion

tip to three quarter span position (from $t^* = 0.05$ to 0.25) is estimated to be between 0.6 and $0.83\,U_{ref}$. The flow originating from the trailing edge at half span convects downstream more rapidly than the flow at three quarter span position, illustrated in Figure 6.6b, suggesting more force is produced near the root of the airfoil. From the trailing edge there is some flow observed toward the leading edge, originating from the three quarter span position at $t^* = 0.27$ and from the half span position at $t^* = 0.37$. There is no formation of a trailing edge vortex due to the onset of the rotation at supination and no formation of a second leading edge vortex.

At a distance of 2 chord lengths downstream the wake had contracted by roughly 2 chord lengths, which is similar to the bio-inspired motions.

Comparing the three motions a number of conclusions can be drawn. The dye flow visualized the formation of one leading edge vortex per half cycle for hover motion 1 and the pure sinusoidal motion. The evolution in time of the leading edge vortex is different for all motions. The largest difference is that the LEV completely detaches during the stroke in hover motion 2 and a second LEV is formed at stroke reversal. For the purely sinusoidal motion there is one trailing edge vortex formed at the start of the motion and it was observed to be faint compared to the starting vortex of hover motion 1 and 2. The bio-inspired motions both exhibit the formation of a second TEV at the supination right before stroke reversal.

Although the time history flow development is unique to every motion, some generalizations hold. For all motions the wake seems to be moving downstream with a velocity that is of the same order of magnitude, approximately 0.1 to $0.25\,U_{ref}$. Thus the momentum in the wake is comparable and hence the thrust is expected to be of the same order of magnitude.

The dye originating from the trailing edge moves faster downstream at the half span position than at the three quarter span position and consequently it is expected that the half span region accounts for more thrust force than the region closer to the tip.

A spanwise flow was observed for all motions. A qualitative measurement of its average

spanwise velocity, between the tip and the three quarter chord position in the beginning of the stroke, revealed that the spanwise velocity component is in order of $0.7\,U_{ref}$. It is very plausible that the spanwise component is even larger, since the flow seemed to be accelerating within this region. Furthermore spanwise flow was observed later in the stroke; its magnitude proved to be difficult to quantify using the flow visualization method.

6.2.3 Particle image velocimetry

Complementary to the force data acquisition and the dye flow visualization, two dimensional particle image velocimetry is performed. Two measurement positions were chosen in the plane perpendicular to the airfoil, one at half and one at the quarter span position. The flow topology at half span is expected to be representative for the flow topology on the majority of the airfoil. The images at the quarter chord position were taken to obtain more information about the three dimensional effects due to the wing tip.

The axes in all plots show the distance in mean chords, with zero being the position of the leading edge at half span and the mid position of the plunge motion. Note that the chord length at half span is larger than the mean chord length. The plots are ordered chronologically from left to right, top to bottom. In all figures the airfoil is plunging downwards or the plunge velocity is zero and the leading edge is on the left side of the figure.

Using flow visualization we observed a significant axial flow and a large contraction of the wake. Therefore the measurements are taken with a 2ms time delay between the images and the resolution as described in Section 5.6. These settings give us a good estimate of the flow topology, while keeping the measurements reliable both in the vortices close to the airfoil as further away from the airfoil where the flow speeds are much smaller, in the order of 0.7 to $0.1\,U_{ref}$, cf. Appendix B.

Images at half span position

Figure 6.7 shows the vorticity and streamlines of the phase-averaged flow field for hover motion 1 at half span and phases as indicated. At the beginning of the stroke we see that the LEV from the previous half stroke breaks into two pieces, a small part flowing over the leading edge dissipating almost immediately and a larger part moves along the airfoil surface to the trailing edge where it interacts with the TEV or starting vortex. There is evidence of one LEV forming from approximately $t^* = 0.2$ until the end of the stroke. The largest thrust coefficient occurs at $t^* = 0.2$. After the change in pitch rate at $t^* = 0.4$, where the largest force coefficient occurs, another starting vortex appears at the trailing edge. This vortex and the starting vortex at stroke reversal, which has opposite circulation, combine to form a persistent vortex structure.

The phase-averaged vorticity and streamlines for hover motion 2 are plotted in Figure 6.8. Similarly to HM1, the LEV breaks into two parts at stroke reversal. The larger part joins the starting vortex at the trailing edge. The other part remains around the leading edge and is entrained and annihilated by the new LEV having opposite circulation. In this case the LEV detaches between $t^* = 0.2$ and 0.4, stimulated by the increase of the pitch angle at $t^* = 0.25$. A new LEV forms around $t^* = 0.4$. These flow features correlate closely with the two peaks in force coefficients.

In Figure 6.9, the phase-averaged vorticity and streamlines for the sine motion are plotted. At the start of the stroke during stroke reversal, the vorticity contours show significantly weaker LE and TE vortices compared to the other two kinematics, which is consistent with the relative low force coefficient measured at these phases. For this kinematics the LEV is observed first on the image corresponding to $t^* = 0.2$. The force coefficients at the beginning of the stroke are small but as the LEV grows larger the force coefficients surmount the maximum coefficients of both HM1 and 2. There is no formation of a TEV at stroke reversal, in contrast to HM1 and 2.

Analogous to the qualitative observations made with the dye flow visualization method, the PIV data shows the time history of the vortical flow evolution differs distinctly comparing the three motions. This was also reflected in the time history of the forces, although the average force coefficients are of the same order of magnitude, i.e. within a 20 % range with respect to each other.

The maximum and minimum values of the vorticity were also measured. The minimum vorticity was generally found in the vicinity of the LEV vortex core or the leading edge, e.g. during the formation of an LEV. Similarly, the maximum vorticity value was generally found in the vicinity of the TEV vortex core or the TE, although this did not always lead to the formation of a vortex, e.g. Figure 6.7 at $t^* = 0.2$.

The correlation between the absolute strength of the vorticity and the force normal to the airfoil was investigated. The correlation coefficients are tabulated in Table 6.3. When taking into account only the maximum vorticity in the vicinity of the LE or the maximum strength of the LEV the correlation coefficients range between 0.62 and 0.83. When the maximum vorticity at the TE is taken into account, i.e. a summation of the absolute values, the correlation coefficients are higher than 0.9, excluding the HM2 case. Looking at the PIV images for HM2, it is hypothesized that the effect of the vortex at the TE might be small at $t^* = 0.5$ due to the larger distance. The correlation between the vorticity and force coefficient increased to 0.94 when the maximum vorticity in the TEV at $t^* = 0.5$ was discarded from the data set.

The close correlation between the forces and the leading and trailing edge vortex indicate that these are very important in force generation of the present experiments (pitch-plunge kinematics at a Reynolds number of $4,800$ and a reduced frequency of 0.38). Note that

[a] Correlation coefficient if the strength of the TEV at $t^* = 0.5$ is not accounted for, i.e. set to zero

Table 6.3: Correlation coefficients between maximum vorticity in the PIV images and the corresponding force coefficients

	HM1	HM2	Sine
LE(V)	0.73	0.62	0.83
|LE(V)| + |TE(V)|	0.91	0.68 (0.94[a])	0.99

the correlation coefficients are based on five discrete measurement points for three different cases and do not include the proximity of the maximum strength with respect to the airfoil as a scaling variable.

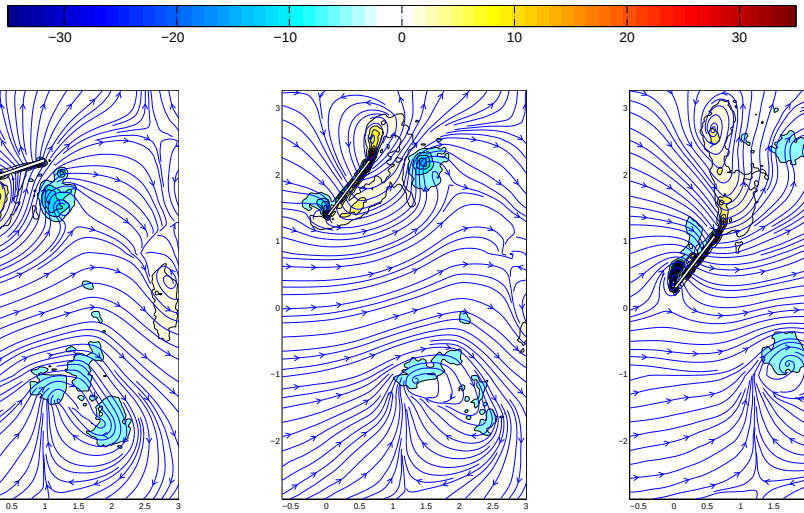

(a) $t^* = 0.0$, $C_T = 0.47$, $C_{Lat} = -1.39$ (b) $t^* = 0.1$, $C_T = 2.68$, $C_{Lat} = -2.11$ (c) $t^* = 0.2$, $C_T = 4.90$, $C_{Lat} = -3.30$

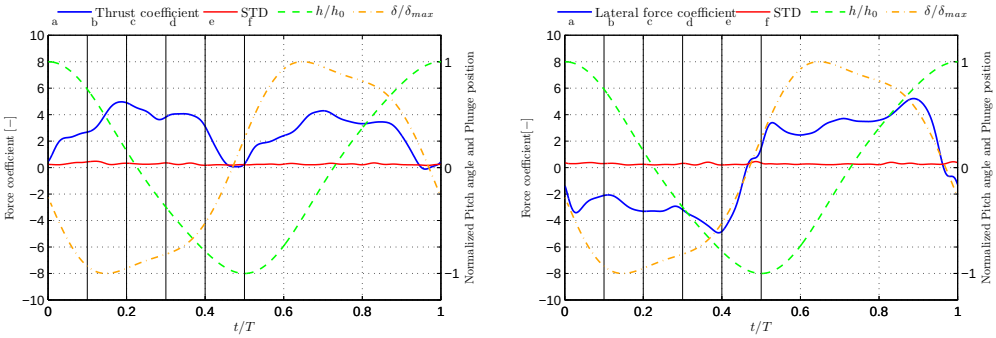

(d) $t^* = 0.3$, $C_T = 3.82$, $C_{Lat} = -3.16$ (e) $t^* = 0.4$, $C_T = 3.11$, $C_{Lat} = -4.82$ (f) $t^* = 0.5$, $C_T = 0.27$, $C_{Lat} = -1.47$

Figure 6.7: Vorticity and streamline plots for HM1 base at half span, $C_T = 2.79$ and $|C_{Lat}| = 3.00$

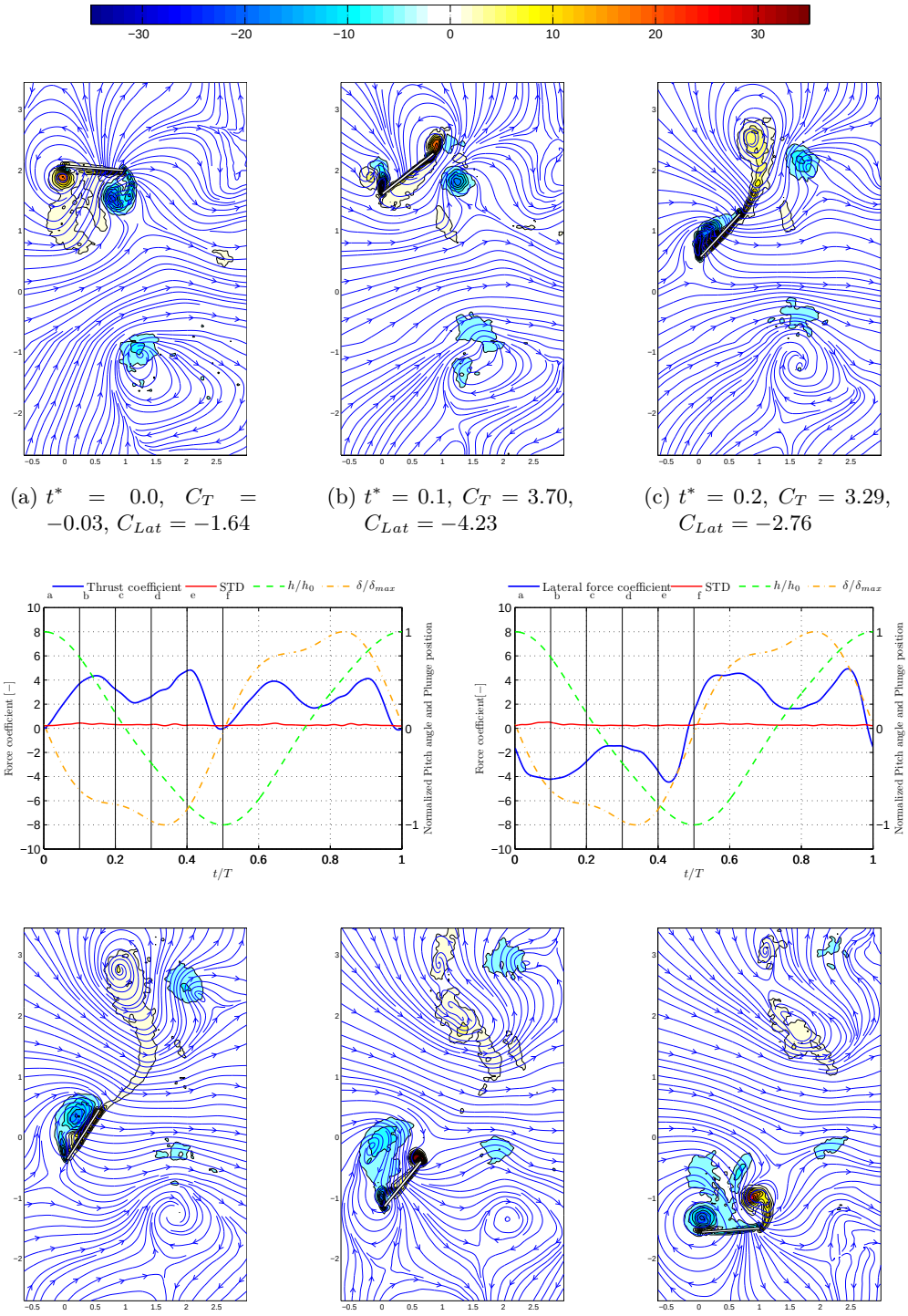

(a) $t^* = 0.0$, $C_T = -0.03$, $C_{Lat} = -1.64$

(b) $t^* = 0.1$, $C_T = 3.70$, $C_{Lat} = -4.23$

(c) $t^* = 0.2$, $C_T = 3.29$, $C_{Lat} = -2.76$

(d) $t^* = 0.3$, $C_T = 2.61$, $C_{Lat} = -1.46$

(e) $t^* = 0.4$, $C_T = 4.76$, $C_{Lat} = -3.57$

(f) $t^* = 0.5$, $C_T = -0.06$, $C_{Lat} = 1.43$

Figure 6.8: Vorticity and streamline plots for HM2 base at half span, $C_T = 2.64$ and $|C_{Lat}| = 2.98$

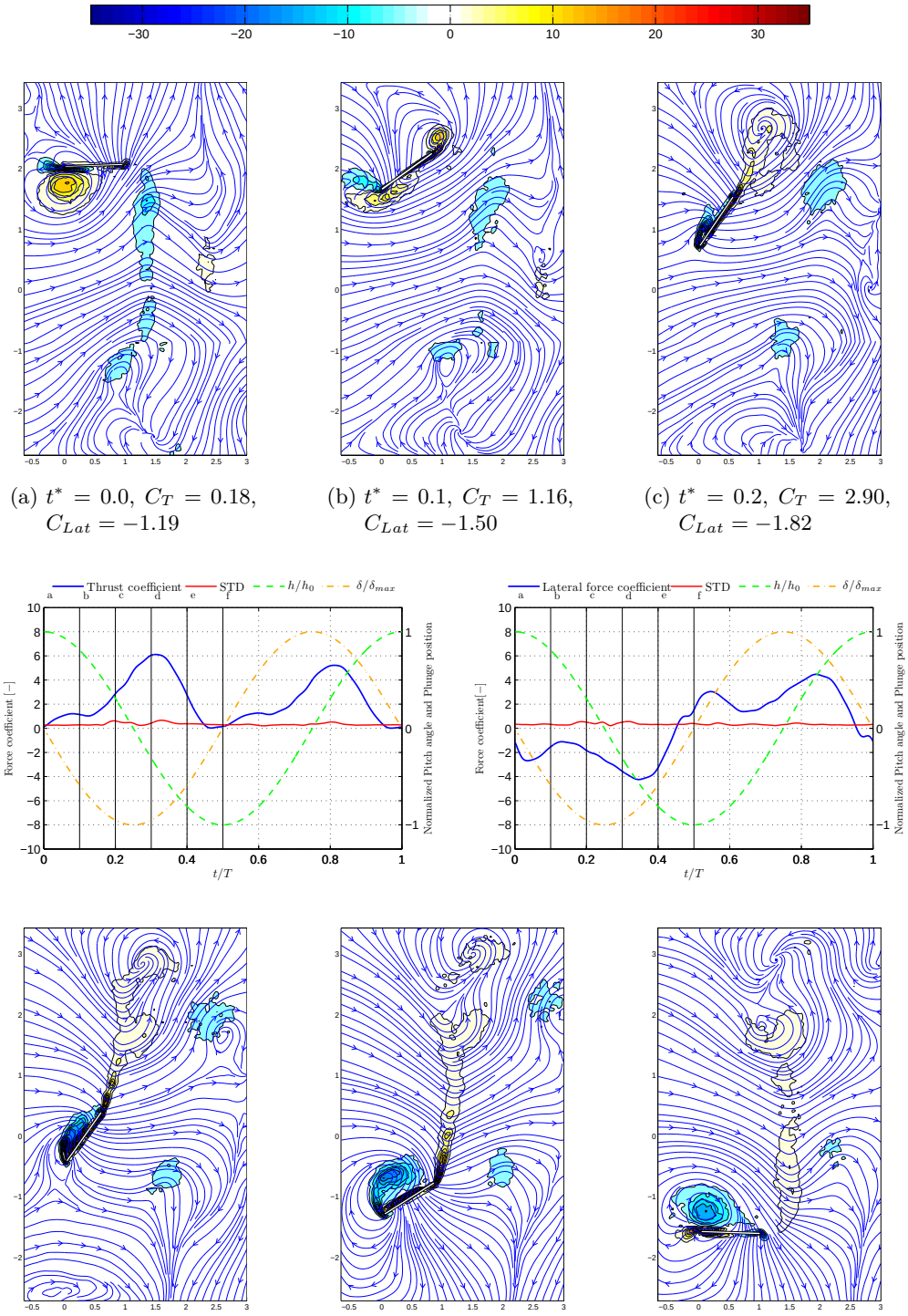

(a) $t^* = 0.0$, $C_T = 0.18$, $C_{Lat} = -1.19$

(b) $t^* = 0.1$, $C_T = 1.16$, $C_{Lat} = -1.50$

(c) $t^* = 0.2$, $C_T = 2.90$, $C_{Lat} = -1.82$

(d) $t^* = 0.3$, $C_T = 6.06$, $C_{Lat} = -3.58$

(e) $t^* = 0.4$, $C_T = 2.75$, $C_{Lat} = -3.26$

(f) $t^* = 0.5$, $C_T = 0.16$, $C_{Lat} = 1.51$

Figure 6.9: Vorticity and streamline plots for Sine base at half span, $C_T = 2.39$ and $|C_{Lat}| = 2.39$

Images at three quarter span position

The measurements performed at the quarter span position are influenced by the presence of the wing tip and include a number of three dimensional effects.

The vorticity and phase-averaged streamlines of hover motion one are shown in Figure 6.11. In the first image, at $t^* = 0.0$, the LEV and TEV are clearly visible, similar to the images taken at half span. The wake of the wing however shows some distinct differences. There is a clear region with a path of positive and negative vorticity. Over this region there is clear flow opposite to the thrust direction. This reverse flow is believed to be direct evidence of the presence of a tip vortex. In the following images the tell tale signs of the tip vortex disappear and the vorticity field becomes comparable to the half span position. The tip vortex effects reappear in the images taken at $t^* = 0.4$ and are very prominent at $t^* = 0.5$.

The effects of the tip vortex are not as clearly observed for hover motion two, Figure 6.12. However at $t^* = 0.2$ two patches of opposite vorticity appear near the trailing edge of the wing, likely to be caused by the tip vortex from the previous stroke. The evolution of LEV's and TEV's is similar to the half span position with a detachment of the LEV around $t^* = 0.2$ and formation of a new LEV and TEV at the end of the stroke.

For the simple harmonic case, the pure sinusoidal motion, the phase-averaged vorticity and streamlines at three quarter span are shown in Figure 6.13. Similar to HM1 indications of the presence of a tip vortex are found at $t^* = 0.0$, 0.1 and 0.5. The general evolution of the LEV and TEV is similar to the half span position.

Table 6.4: Correlation coefficients between sum of the maximum and minimum vorticity in absolute values obtained from the PIV measurements and the corresponding normal force coefficients

	HM1	HM2	Sine
Half span	0.91	0.68 (0.94[b])	0.99
Three quarter span	0.87	0.85	0.98
Sum of half and three quarter span	0.93	0.91	0.99

As described in the previous section the sum of the maximum and minimum vorticity in absolute values can be correlated to the normal force coefficient. The results for the three quarter span position and the sum with the half span position are tabulated in Table 6.4. The correlation with the normal force is higher then 0.85 for all cases and always smaller than the correlation at half span. When the maxima of the half and three quarter span position are added the correlation is almost equal to the correlation at half span, although the values at three quarter span are of the same order of magnitude compared to half span. A visual representation of the normal force coefficient and scaled vorticity

[b] Correlation coefficient if the strength of the TEV at $t^* = 0.5$ is not accounted for, i.e. set to zero.

strength is shown in Figure 6.10. The vorticity strength follows the same trends as the force coefficients and hence the correlation coefficients are close to 1.

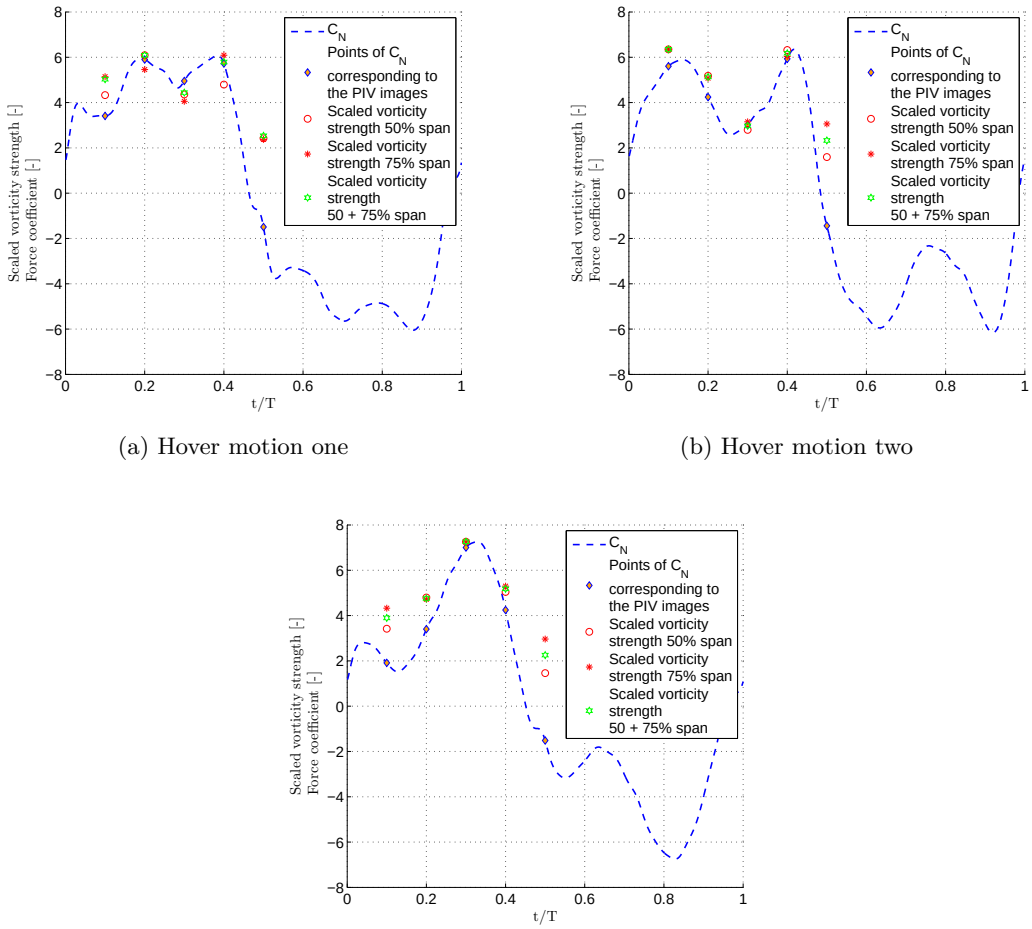

(a) Hover motion one

(b) Hover motion two

(c) Sinusoidal motion

Figure 6.10: Plots of the normal force coefficient and the sum of the maximum and minimum vorticity in absolute values at half span and three quarter span and their sums (the vorticity is scaled with the maximum value of the force coefficient to fit the figure)

In general the maximum flow speeds at the three quarter span position are always less then half of the speed measured at half span. The out of plane velocity in this region was estimated through dye flow visualization to be of the same order of magnitude as the reference velocity. As expected, the in-plane streamlines indicate the presence of out of plane velocity.

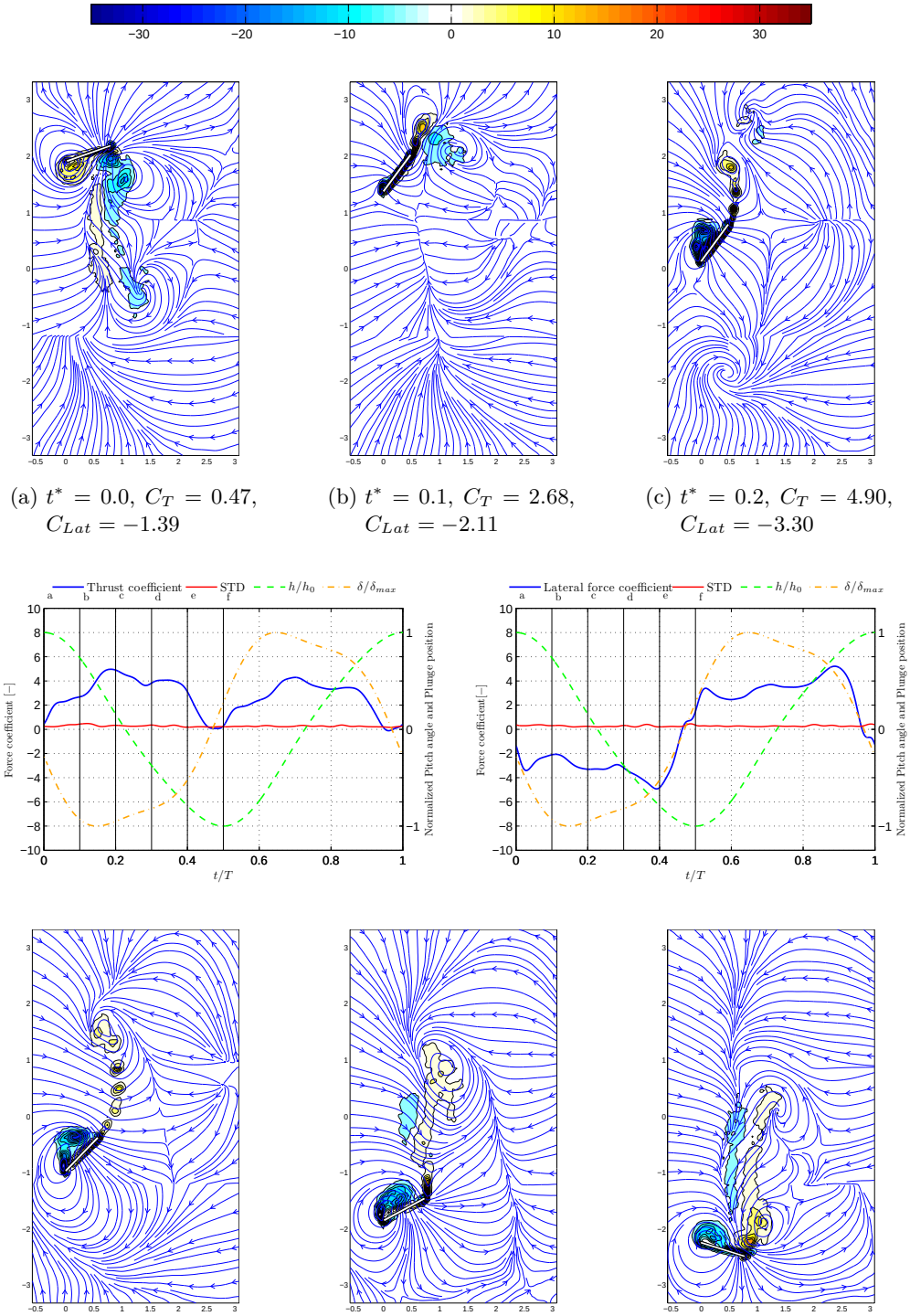

(a) $t^* = 0.0$, $C_T = 0.47$, $C_{Lat} = -1.39$

(b) $t^* = 0.1$, $C_T = 2.68$, $C_{Lat} = -2.11$

(c) $t^* = 0.2$, $C_T = 4.90$, $C_{Lat} = -3.30$

(d) $t^* = 0.3$, $C_T = 3.82$, $C_{Lat} = -3.16$

(e) $t^* = 0.4$, $C_T = 3.11$, $C_{Lat} = -4.82$

(f) $t^* = 0.5$, $C_T = 0.27$, $C_{Lat} = -1.47$

Figure 6.11: Vorticity and streamline plots for HM1 base at three quarter span, $C_T = 2.79$ and $|C_{Lat}| = 3.00$

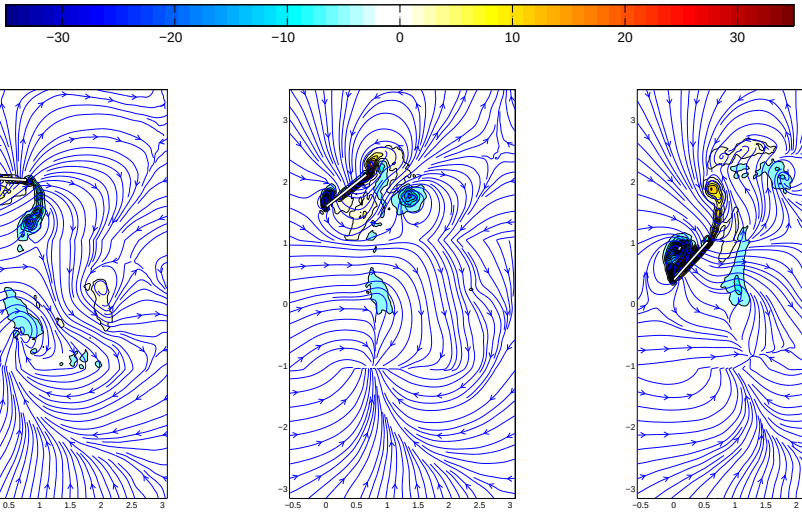

(a) $t^* = 0.0$, $C_T = -0.03$, $C_{Lat} = -1.64$

(b) $t^* = 0.1$, $C_T = 3.70$, $C_{Lat} = -4.23$

(c) $t^* = 0.2$, $C_T = 3.29$, $C_{Lat} = -2.76$

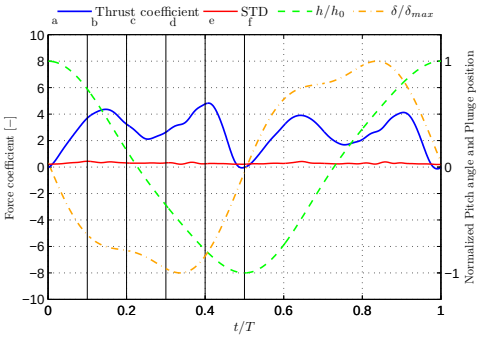

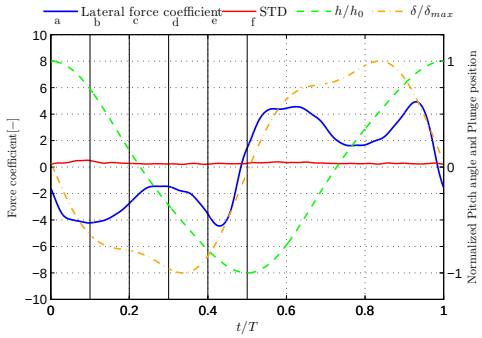

(d) $t^* = 0.3$, $C_T = 2.61$, $C_{Lat} = -1.46$

(e) $t^* = 0.4$, $C_T = 4.76$, $C_{Lat} = -3.57$

(f) $t^* = 0.5$, $C_T = -0.06$, $C_{Lat} = 1.43$

Figure 6.12: Vorticity and streamline plots for HM2 base at three quarter span, $C_T = 2.64$ and $|C_{Lat}| = 2.98$

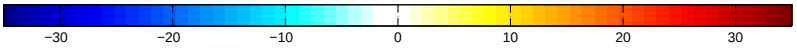

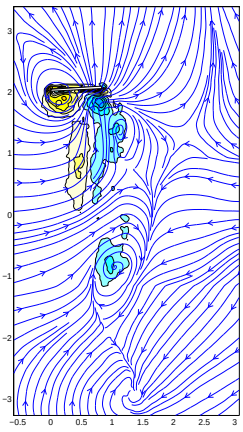

(a) $t^* = 0.0$, $C_T = 0.18$, $C_{Lat} = -1.19$

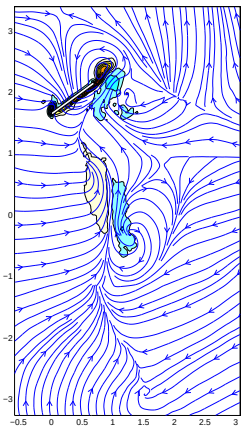

(b) $t^* = 0.1$, $C_T = 1.16$, $C_{Lat} = -1.50$

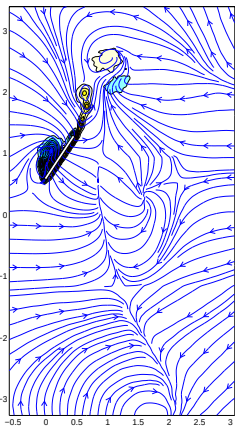

(c) $t^* = 0.2$, $C_T = 2.90$, $C_{Lat} = -1.82$

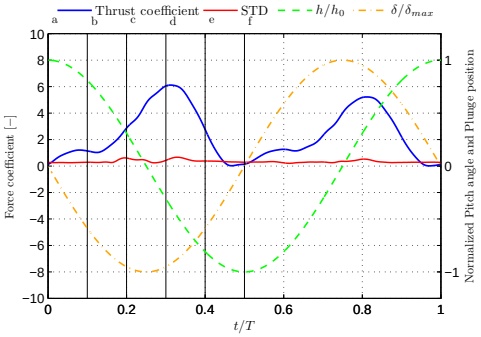

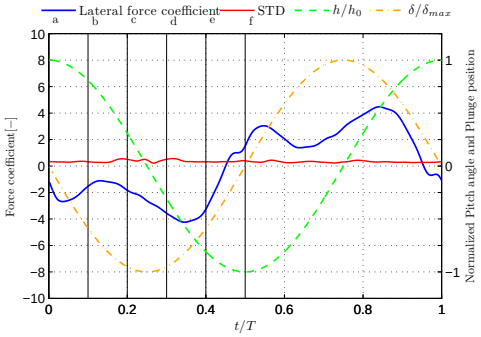

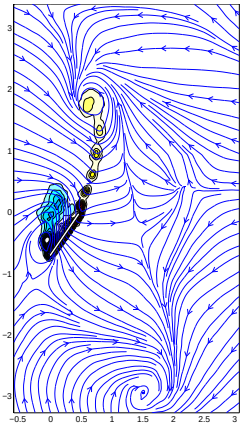

(d) $t^* = 0.3$, $C_T = 6.06$, $C_{Lat} = -3.58$

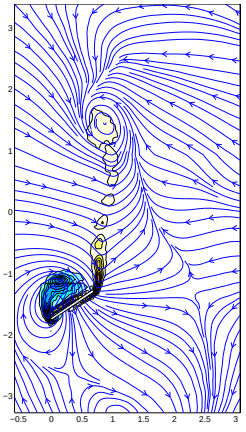

(e) $t^* = 0.4$, $C_T = 2.75$, $C_{Lat} = -3.26$

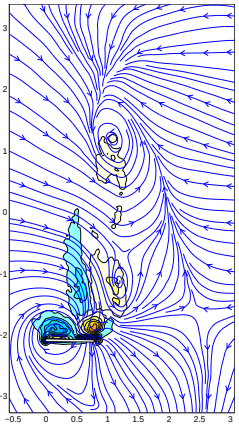

(f) $t^* = 0.5$, $C_T = 0.16$, $C_{Lat} = 1.51$

Figure 6.13: Vorticity and streamline plots for Sine base at three quarter span, $C_T = 2.39$ and $|C_{Lat}| = 2.39$

6.2.4 Comparison with the unsteady aerodynamic vortex model

The unsteady aerodynamic model is based on two-dimensional potential flow and uses a vorticity/circulation approach to compute the aerodynamic loads. The formulation was originally derived for rigid wings in hover [3, 4]. The model has been subsequently modified to account for spanwise and chordwise wing flexibility [16, 17] and freestream due to forward flight speed [15]. The effect of the Reynolds number is also incorporated into the calculation of shed vorticity [15].

Transient and time-averaged forces, computed using the approximate model, were compared with those obtained from CFD-based computations for rigid airfoils as well as wings in hover and forward flight [16, 17, 15]. For all cases considered, the approximate unsteady aerodynamic loads show reasonable agreement with CFD-based results.

The overall approach is as follows. First, the wing is divided into several spanwise stations, where each section is represented as an airfoil. For each airfoil, an airfoil-wake surface that captures the airfoil degrees of freedom (DOF), and approximates the geometry of the shed wake, is identified. Next, the airfoil and the airfoil-wake surface are transformed to a circle in the complex plane using conformal mapping. Thus, the airfoil-bound and shed wake vorticity are computed on the complex plane. The quasi-steady component of vorticity is obtained by neglecting the effect of the shed wake. The strength of shed vorticity is computed by enforcing a stagnation condition at the leading edge (LE) and a Kutta condition at the trailing edge (TE). The airfoil bound vorticity is obtained as a sum of the quasi-steady and wake-induced vorticity on the airfoil. Next, the vorticity in the complex plane is transformed back to the airfoil-wake surface (physical plane) using the inverse transform. The unsteady loads acting on the airfoil are obtained from the total vorticity using the unsteady Bernoulli equation. Finally, the shed vorticity is convected using the Rott-Birkhoff equation, which is derived from Biot-Savart law for two dimensional flow.

The calculations were performed by Dr. Abhijit Gogulapati, a Post Doctoral Research Fellow at the University of Michigan Aerospace department [18]. The comparison of the forces with the unsteady aerodynamic model for HM1, HM2 and the sinusoidal motion are shown in Figure 6.15, 6.16, and 6.17 respectively. The calculations show a reasonable agreement with the experiments.

For the case of hover, the vortices that are shed during previous cycles remain in the vicinity of the wing and therefore influence the forces generated by the wing even after several subsequent cycles. Consequently, the mean forces were computed once the forces reached an approximate steady state. For all the cases considered, an approximate steady state was reached after the second cycle as shown in the Figures. Simulations also showed that decreasing the vortex core improved correlation with experimental results. Decreasing the vortex core size promotes vortex roll up. Thus it appears that a core size of $0.025\,c$ captures the vortex dynamics most accurately. Furthermore, decreasing the size of the vortex core also decreased the noise generated due to interaction of the

vortices with the airfoil thereby improving quality of the solution. It appears that decreasing the core size further had a comparatively minor impact on the forces (cf. Figure 6.14).

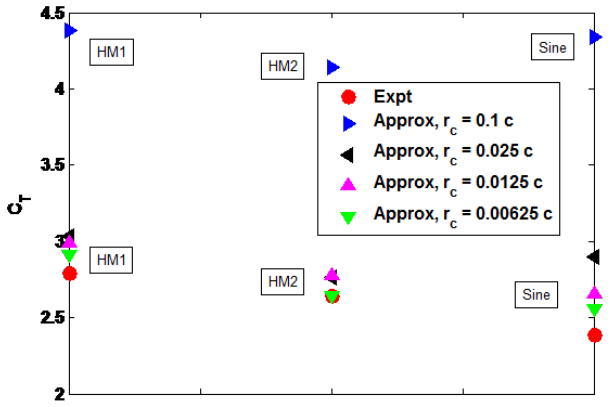

Figure 6.14: Comparison of the force coefficients for different core radii

The flow visualization data revealed the presence of tip vortices and a spanwise component of the flow from the tip towards the root of the wing. However, the good overall agreement between the calculated and measured forces suggests that the dominant force generating mechanisms are the leading and trailing edge vortices. The impact of spanwise flow and tip vortices on the overall magnitude of the forces is not as significant.

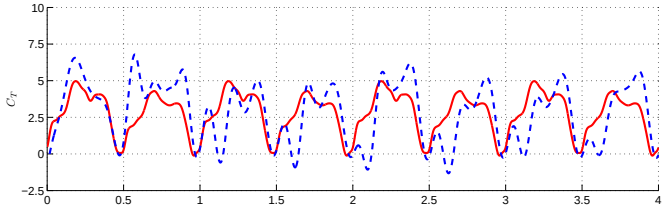

(a) Thrust force coefficient, C_T

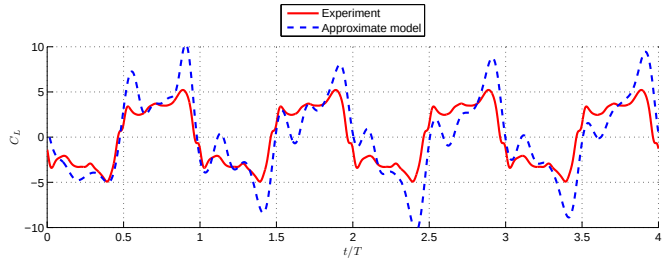

(b) Lateral force coefficient, C_L

Figure 6.15: Comparison of the force coefficients for hover motion 1 as measured in the experiment and the ones calculated with the approximate model

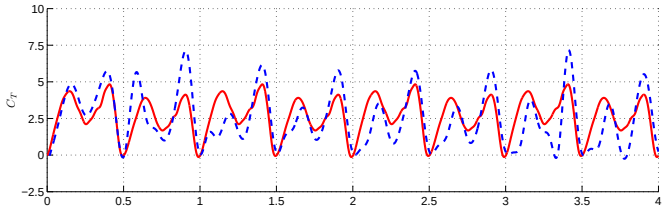

(a) Thrust force coefficient, C_T

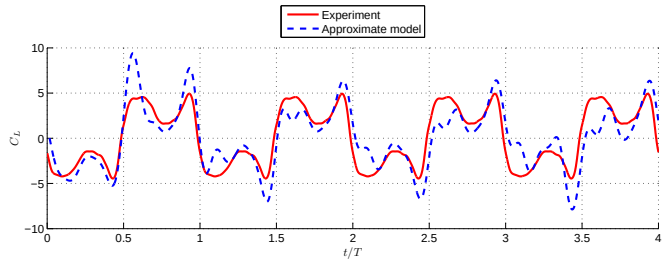

(b) Lateral force coefficient, C_L

Figure 6.16: Comparison of the force coefficients for hover motion 2 as measured in the experiment and the ones calculated with the approximate model

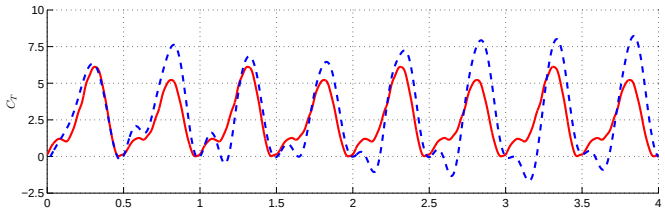

(a) Thrust force coefficient, C_T

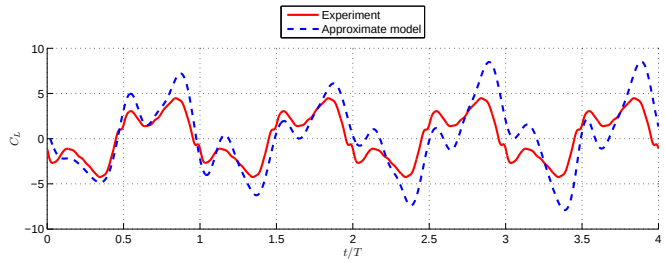

(b) Lateral force coefficient, C_L

Figure 6.17: Comparison of the force coefficients for the purely sinusoidal motion as measured in the experiment and the ones calculated with the approximate model

6.2.5 Comparison with the high-fidelity CFD model

The results are compared to CFD calculations performed in house by Dr. Chang-kwon Kang, a Post Doctoral Research Fellow at the University of Michigan Aerospace department [25].

The governing equations for the fluid are the incompressible Navier-Stokes equations and the CFD solution is obtained using Loci-STREAM. Loci-STREAM is an all-speed, pressure based, finite volume CFD solver for arbitrary unstructured polygonal meshes [24, 46].

The computational grid to solve the Navier-Stokes equations consists of mixed brick and tetrahedral cells around the Zimmerman wing, see Figure 6.18. To assess the grid size sensitivity three grids with different spatial resolutions are utilized with 0.34×10^6, 0.51×10^6, and 0.73×10^6 nodes for each mesh. For the time step sensitivity analysis 250, 500, and 1000 time steps per motion cycle were chosen. The fluid flow is assumed to be laminar. The first grid spacing from the wing surface is set to 2.5×10^{-3} and the outer boundary of the computational grid is located at 30 chords away from the wing. At the outer computational boundary zero velocity and reference density are assigned. On the wing surface the no-slip condition is applied.

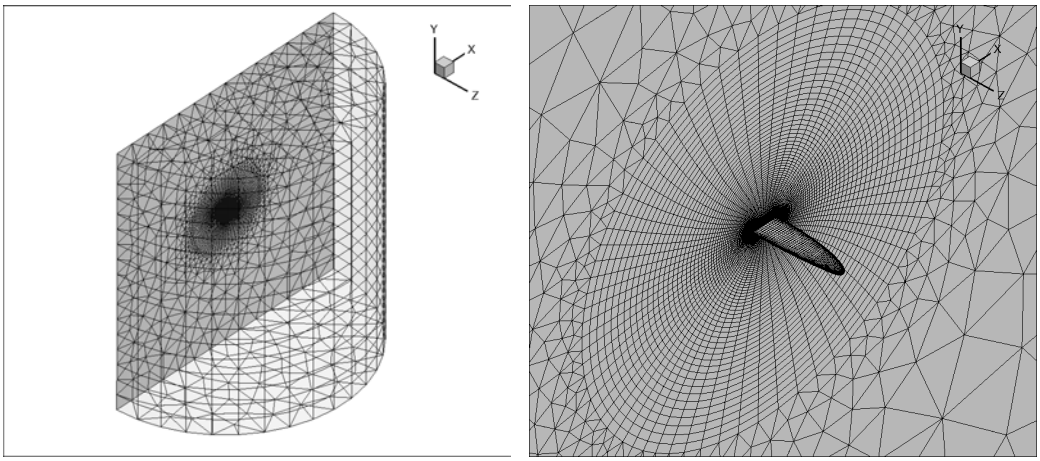

(a) Computational domain

(b) Mesh distribution around the Zimmerman wing

Figure 6.18: Computational grids for the Zimmerman wing

The time history of the force coefficients for the CFD model and the experiment are shown in Figure 6.19, 6.20, and 6.21. In these figures the force coefficients of the experiment represented by a repetition of the averaged time history, the CFD results were calculated over 5.5 cycles. It takes roughly two cycles for the forces to converge into a quasi-steady state value, and due to the complex wake it is not expected that a true steady state would ever be reached.

The shape of the time history of the force coefficients is remarkably similar to the measurements for all motions. As with the experiments there is a slight asymmetry in the

force coefficients for the up and downstrokes. For HM1 the CFD results can almost be linearly scaled to fit the experimental results. There is a small disagreement for HM2 in each stroke, that is the ratio between the first and second maximum in the thrust force coefficient is slightly larger in the CFD calculations. And the differences between the up and downstroke are a lot less pronounced for the purely sinusoidal motion. For all motions however the shape is very similar.

Table 6.5: Base motion average force coefficients, experiment versus CFD (averaged over the last 4 cycles)

	HM1		HM2		Sine	
	Experiment	CFD	Experiment	CFD	Experiment	CFD
C_T	2.79	2.37	2.64	2.29	2.39	1.96
$\lvert C_{Lateral} \rvert$	3.00	2.64	2.98	2.50	2.39	2.08

The average force coefficients for both CFD calculations and force measurements are summarized in Table 6.5. On average the forces computed with CFD are between 82 and 87 % of the coefficients measured in the experiment. This discrepancy might originate from both differences in the experiment and measurement errors. First, the experimental and CFD cases are not exacly equal. It is expected that there will be wall and blockage effects in the water channel that might increase the forces measured, these effects are unquantifyable at this point and it is not sure to what extend they impact the results. There is also an offset between the center of the motions and the center of the water channel and this can cause an exaggerated asymmetry in the up and downstroke. Second, the CFD results do not perfectly capture the exact physics of the flow. The flow is also assumed to be laminar and hence turbulent effects are another source of disagreement.

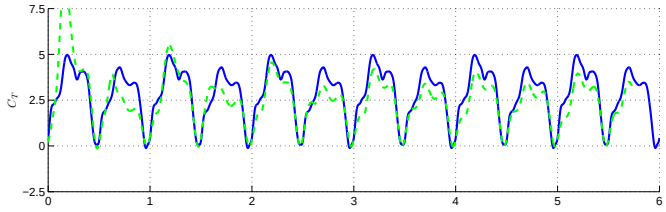

(a) Thrust force coefficient, C_T

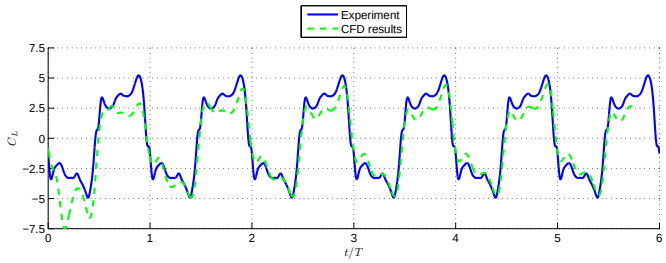

(b) Lateral force coefficient, C_L

Figure 6.19: Comparison of the force coefficients for hover motion 1 as measured in the experiment and the ones calculated with the CFD model

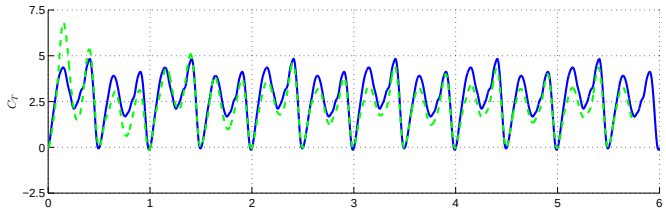

(a) Thrust force coefficient, C_T

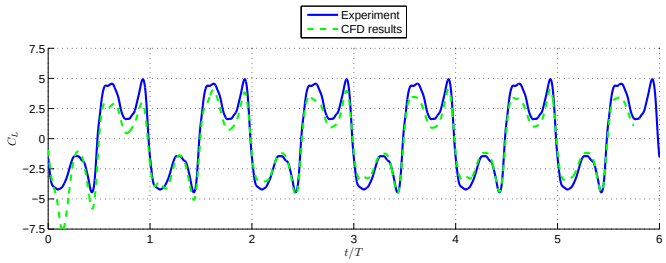

(b) Lateral force coefficient, C_L

Figure 6.20: Comparison of the force coefficients for hover motion 2 as measured in the experiment and the ones calculated with the CFD model

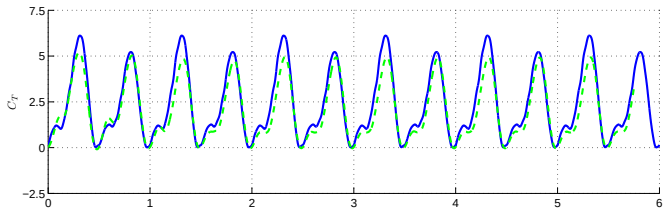

(a) Thrust force coefficient, C_T

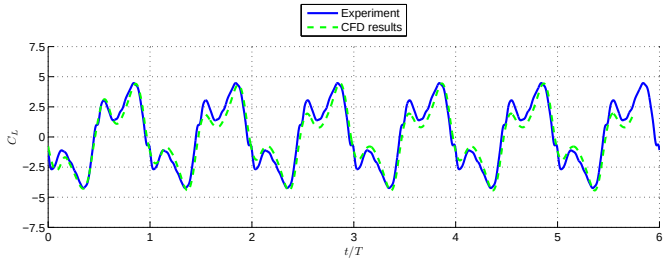

(b) Lateral force coefficient, C_L

Figure 6.21: Comparison of the force coefficients for the purely sinusoidal motion as measured in the experiment and the ones calculated with the CFD model

6.2.6 Comparison with three dimensional flapping experiment with two degrees of freedom

The results of the pitch-plunge motion are compared to the results of Morrison et al [30]. In their experiments the kinematics (HM1, HM2, and the Sinusoidal motion) were tested in the water channel on a two degrees of freedom flapping rig.

The two angular degrees of freedom are the flapping angle, ϕ, and the pitch angle, α. The axis of rotation for the flapping angle is located above the root of the wing and is parallel to the wing when the pitch angle is zero. For the pitch angle the axis of rotation corresponds with a line tangent to the leading edge at the root of the wing and parallel to the wing. The zero position of the pitch angle coincides with the airfoil being perpendicular to the flapping plane. Figure 6.22a shows a visual representation of the flapping angle, pitch angle, and flapping plane. The motion is actuated by two Velmex B4800TS series rotary stages through a custom gear train, shown in Figure 6.22b. The free surface of the water channel is located 40 mm above the flapping axis of rotation.

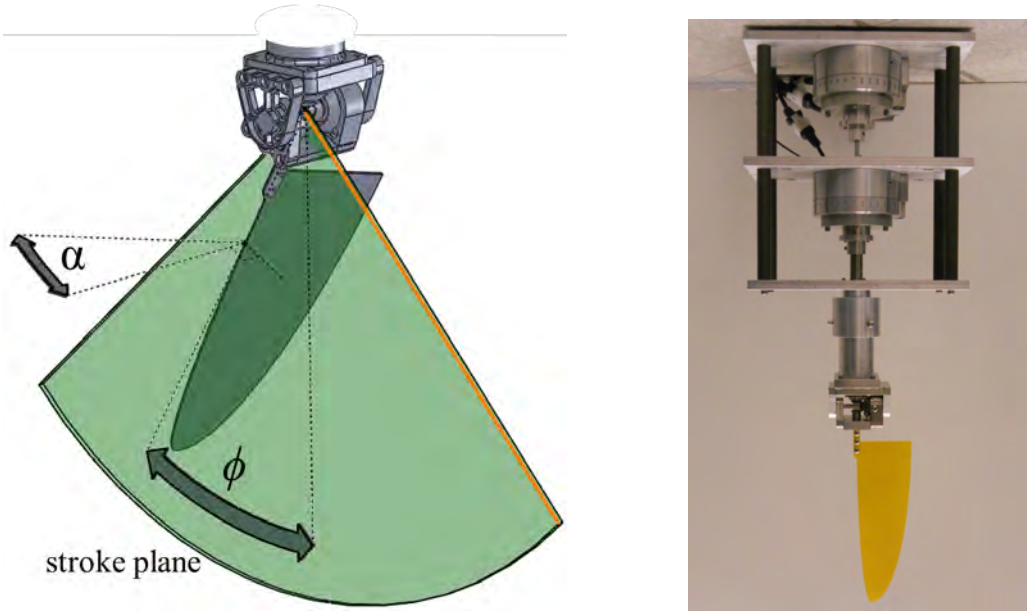

(a) Coordinate system

(b) Assembly of the flapping rig

Figure 6.22: Two degree of freedom flapping rig for experiments in the water channel

The force data is acquired using a six-component ATI Nano 25 IP68 submersible force/torque transducer. The force/torque sensor is mounted at the root of the wing and moves with the wing. Force data is taken at a sampling frequency of 2 kHz and the data is filtered using a 5^{th} order Butterworth low-pass filter with a 2.5 Hz cut-off frequency. Data is sampled over 100 cycles and subsequently phase-averaged.

To isolate the hydrodynamic force from other contributions to the force and torque acting

on the sensor a tare procedure was used. First, a static tare procedure is performed in both water and air. The static tare consists of static measurements at 50 discrete locations, interpolated using a 6-term Fourrier series representation of the averaged data at the 50 locations. Second, a dynamic tare is performed in air to be able to subtract the inertial loads due to the wing mass and the kinematics.

For the comparison with the pitch-plunge experiments the lateral force coefficient for the flapping motion is defined as the force coefficient perpendicular to the rotation axis and parallel to the flapping plane. Similarly the thrust coefficient is defined as the force coefficient perpendicular to the flapping plane with the positive direction towards leading edge. The force coefficients for flapping are normalized by the projected wing area and the dynamic pressure based on the reference velocity, $U_{ref} = 122e-3\,m/s$, as reported by Morrison et al [30].

The time history of the force coefficients compares well with the pitch-plunge results when looking at the force perpendicular to the rotation axis and parallel to the flapping plane, shown in Figure 6.23. Note that the lateral force coefficients in the original paper are reported as the force parallel to the flapping plane perpendicular to the line where the flapping angle is zero, in other words stationary with respect to the airfoil.

The shape of the phase averaged force coefficients of the lateral force for HM1 is nearly analogous when comparing flapping and pitch-plunging kinematics. The thrust force coefficient has a subtle difference, the middle peak in the thrust coefficient is slightly more pronounced in the flapping results.

The largest discrepancy of the shape of the time history of the force coefficients is found in HM2. The thrust for both motions consists of two peaks. For the flapping motion the first peak in thrust is higher than the second one and vice versa for the pitch-plunge kinematics. The lateral force also seems to have a discrepancy in this region, $t^* = 0$ to 0.2. The first peak in the lateral force has changed into two distinct peaks, and in the process the local maximum has shifted slightly aft of the maximum of the pitch-plunge kinematics.

The shape of the sinusoidal motion is nearly analogous for both the lateral and thrust force coefficient. A small difference is spotted in the thrust coefficient where the plunging motion has a small local maximum at the beginning of the stroke, this local maximum seems to be smeared out for the flapping kinematics.

For all motions the shape of the time history of the force coefficients is similar. This leads us to speculate that the underlying lift mechanisms are similar and the flow should have a similar flow topology on most of the airfoil. Furthermore if the flow topology differs significantly this might mean that the kinematics are more important for force generation.

The average force coefficients are summarized in Table 6.6. The trends found in the plunging motion are still present; HM1 produces the most thrust followed by HM2 and

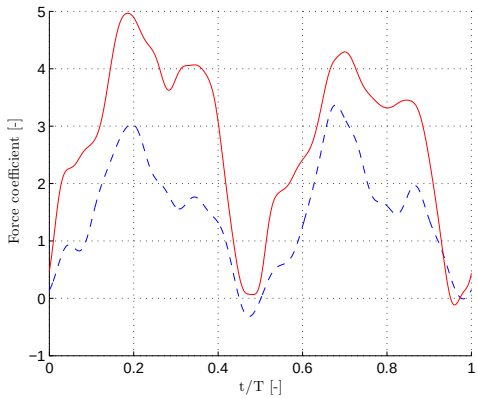

(a) Thrust coefficient HM1

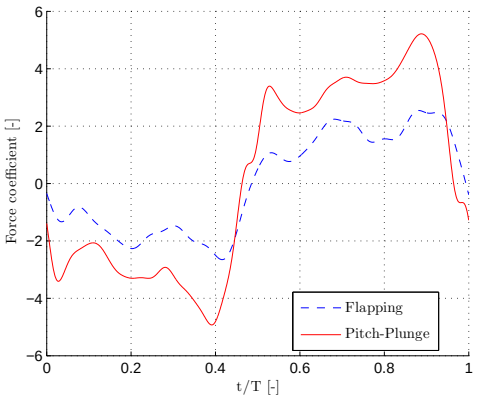

(b) Lateral force coefficient HM1

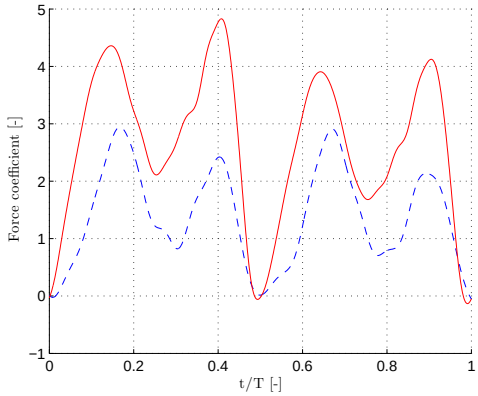

(c) Thrust coefficient HM2

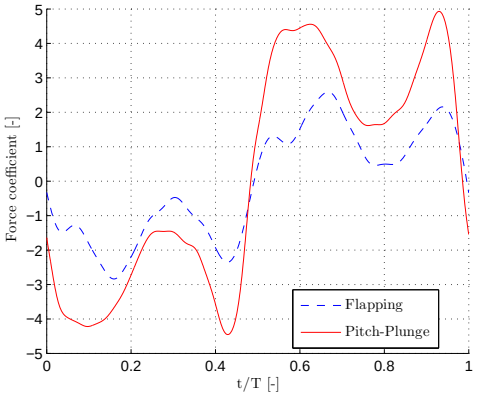

(d) Lateral force coefficient HM2

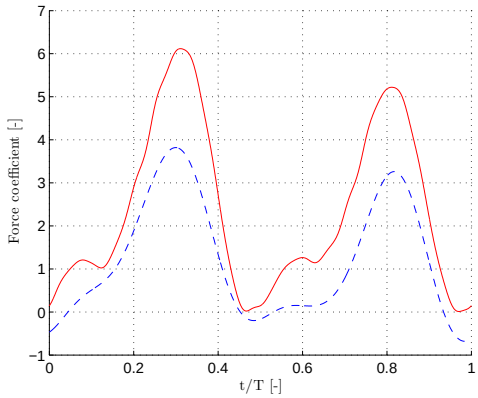

(e) Thrust coefficient pure sinusoidal motion

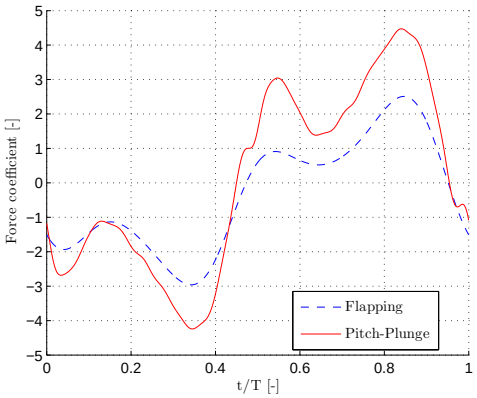

(f) Lateral coefficient pure sinusoidal motion

Figure 6.23: Comparison of pitch-plunge force data with the two degree of freedom flapping force data

the sinusoidal motion. Interestingly the flapping coefficients are roughly half of the coefficients measured with the pitch-plunging rig. It seems as if there might be a scaling rule present, in this case dividing the plunging coefficients by a factor of two will provide a fair estimate for the flapping coefficients.

Table 6.6: Comparison of the flapping and the pitch-plunge motion

	C_T	$\lvert C_{Lateral}\rvert$	Thrust Ratio (Flapping/Plunging)	Lateral Force Ratio (Flapping/Plunging)
HM1	1.49	1.62	0.53	0.53
HM2	1.39	1.44	0.53	0.48
sin	1.21	1.47	0.51	0.61

Careful consideration needs to be taken when comparing flapping motions with pitch-plunging motions. First, there is the difference between flapping and pitch-plunging, i.e. the movement of the root of the airfoil will contribute significantly to the force production in pitch-plunging. Second, the definition of the reference velocity is not the same. The reference velocity in this case is based on the average velocity at 75 % of the span. This not only affects the normalization of the forces but also the Reynolds number, which in the flapping experiments was $7,100$. The reference velocity also affects the reduced frequency ($k = 0.21$ in the flapping experiments). The reduced frequency is analogously defined but not necessarily one to one comparable with the reduced frequency of the pitch-plunging experiments ($k = 0.38$).

6.3 Effects of Changes in Phase

The parameter space can be further expanded by introducing phase lag. The phase lag of the pitch angle is expressed in percentages of the period. Two different cases have been added to the base motions, $\pm 10\%\, T$.

6.3.1 Force coefficients

The results for HM1 are shown in Figure 6.24 and Table 6.7. The delayed rotation case, i.e. having a phase lag of $-10\%T$, produces a lot less thrust than the base case. Furthermore the figure of merit drops to a value of only 0.23. The opposite is true for the advanced rotation case, the thrust is 34% higher than the base case with a decrease in the figure of merit from 0.47 to 0.41. In both cases there is a shift in the location of the minimum thrust corresponding approximately to the amount of phase lag for the advanced rotation case and less then half of the amount of phase lag for the delayed rotation case. For all three motions the minima are close to zero compared to the maxima of the motions.

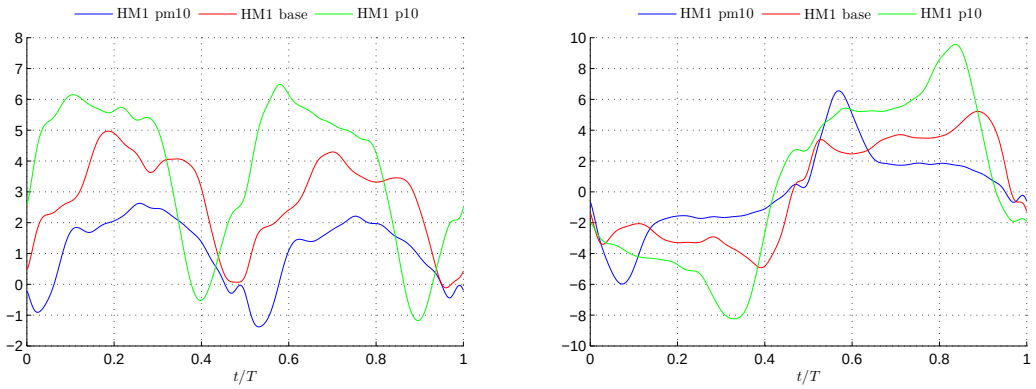

(a) Thrust coefficient

(b) Lateral force coefficient

Figure 6.24: Force coefficient for HM1 with with phase lag

A visual representation of the force vectors on the airfoil is shown in Figure 6.25. The maximum force builds up rapidly for the advanced rotation case and remains high throughout the stroke until the airfoil rotates and the orientation of the force vector becomes unfavorable. The pattern for the base case is similar but less aggressive. For the advanced rotation case the forces are smaller than the two other cases and the orientation at maximum force is less favorable.

Similarly, for the Sine motion (Table 6.8), the delayed rotation case produces less than half of the thrust and has a figure of merit of only 0.17. The advanced rotation case however produces more thrust compared to the base case, about 47% more thrust. The thrust and lateral force coefficients are plotted in Figure 6.26. For the delayed rotation

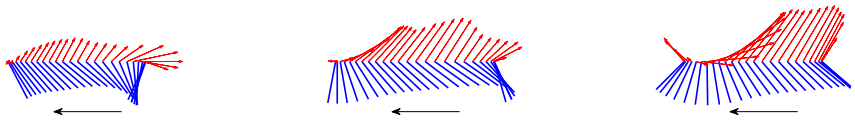

(a) HM1 $-10\%T$ (b) HM1 base motion (c) HM1 $+10\%T$

Figure 6.25: Visualization of HM1 with phase lag and the generated forces

Table 6.7: HM1 force coefficients for different phase lag

	HM1 $-10\%T$	HM1	HM1 $+10\%T$
C_T	1.11	2.79	3.74
$\lvert C_{Lateral}\rvert$	2.17	3.08	4.81
M	0.23	0.47	0.41

case the minimum has shifted by less than half the amount of phase lag, i.e. less than $5\%T$ and for the advanced rotation the shift is roughly equal to the phase lag.

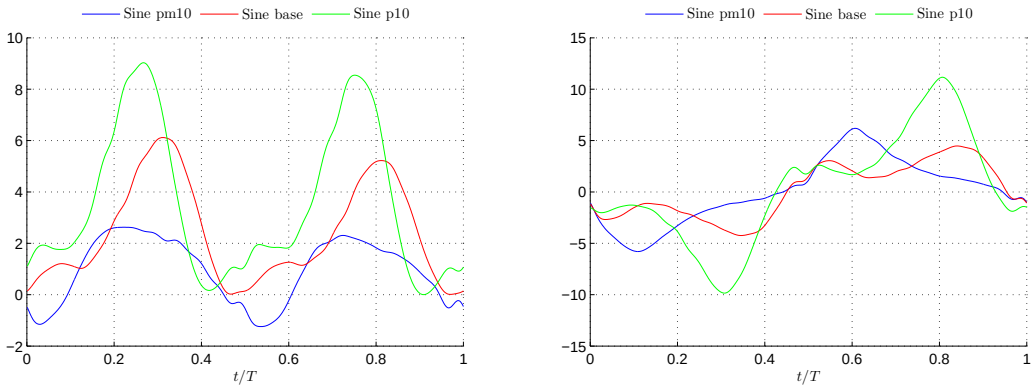

(a) Thrust coefficient (b) Lateral force coefficient

Figure 6.26: Force coefficients for the purely sinusoidal motion with phase lag of $\pm 10\%$

For both HM1 and Sine the thrust production is greatly enhanced by the advanced rotation. The efficiency however decreases from 0.47 to 0.41 and from 0.49 to 0.39 respectively. The location of the maximum force shifts by approximately the amount of phase lag for the advanced rotation cases. Delayed rotation is detrimental for both thrust and efficiency in both motions.

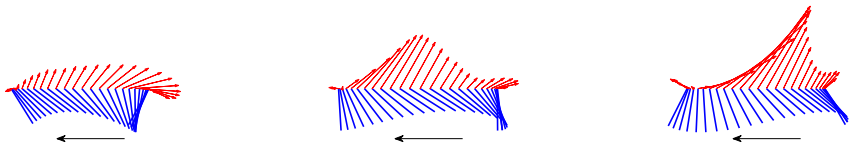

(a) sine $-10\%T$ (b) sine base motion (c) sine $+10\%T$

Figure 6.27: Visualization of sine with phase lag and the generated forces

Table 6.8: Sine force coefficients for different cases of phase lag

	Sine -10%	Sine	Sine $+10\%$
C_T	0.96	2.39	3.51
$\lvert C_{Lateral}\rvert$	2.53	2.39	4.21
M	0.17	0.49	0.39

6.3.2 Dye flow visualization

At $t^* = 0.0$ the HM1 delayed rotation case starts out with a cloud of dye on top of the airfoil. A small vortex forms at both the LE and the TE as the airfoil translates. The vortices are shed immediately, the topology is sketched in Figure 6.28a. At this point the normal force has dropped to a relatively constant value and as the airfoil translates it seems to be fully stalled and no formation of vortices was observed in the flow visualization data, except at the tip. A tip vortex is present during the stroke, the direction of rotation is counter clockwise for an observer looking parallel with the plunge motion and the downstream direction on the left. The distance between the shed tip vortices in the wake varies between one and two chord lengths in the downstream direction depending on the stroke. The average spanwise flow component from the tip to the three quarter chord position was $0.65\,U_{ref}$.

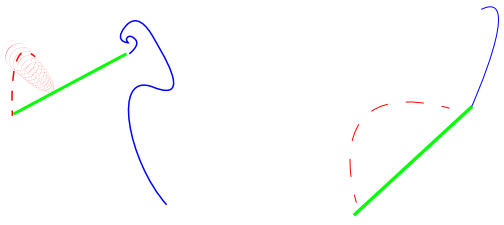

(a) $0.14\,t^*$ (b) $0.42\,t^*$

Figure 6.28: Sketches of the flow visualization features HM1 with a $10\,\%T$ delayed rotation

The motion is not efficient because it is never able to form a proper LEV during the stroke, furthermore the force peak occurs when the airfoil is perpendicular to the plunge

direction and hence in the buildup this force causes some negative thrust.

For the HM1 advanced rotation case a TE starting vortex is created at the very start of the stroke. There is evidence of an LEV forming as sketched in Figure 6.29b and a tip vortex seems to be present early in the stroke. With the advent of a new TEV due to the rotation at $t^* = 0.27$ the tip vortex seems to disappear. The LEV grows very large in size, cf. Figure 6.29c. The normal force changes sign after the change in sign of the pitch motion and hence the thrust is negative from $t^* = 0.38$ to 0.42. The average spanwise flow velocity measured is $1.16\,U_{ref}$. Furthermore a large spanwise contraction of the wake was observed. The contraction was difficult to quantify due to the diffusion of the dye, and it is estimated that the wake had contracted by roughly 2 chord lengths at 2 chord lengths downstream.

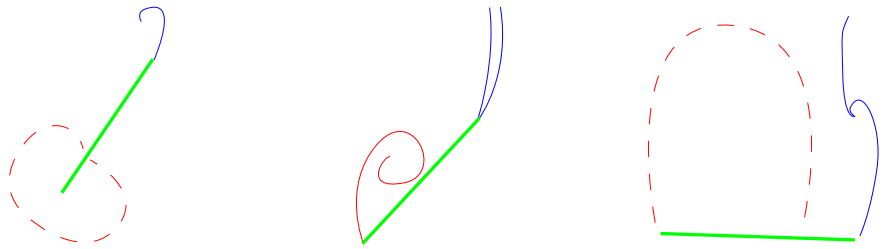

(a) $0.07\,t^*$ (b) $0.2\,t^*$ (c) $0.38\,t^*$

Figure 6.29: Sketches of the flow visualization features HM1 with a $10\,\%T$ advanced rotation

The motion seems to be able to create large forces, with the orientation of these forces in a favorable direction. A gain of 34 % thrust compared to the base motion with a decrease in efficiency of 13 %.

A vortex is created at the leading edge and the trailing edge early in the stroke of the purely sinusoidal delayed rotation case, Figure 6.30a. Both vortices are shed immediately and a tip vortex is formed simultaneously. As the stroke progresses the tip vortex becomes more pronounced and no LEV was visible. At stroke reversal a small TEV is formed due to the rotation of the wing and rapidly broken up before the stroke actually reverses direction. Average spanwise flow speeds were measured to be up to $0.56\,U_{ref}$.

No evidence of high lift mechanisms was observed in this stroke. The airfoils seems to be stalled throughout the entire stroke.

The sinusoidal advanced rotation case generates a faint TE starting vortex as it begins to translate. The first evidence of the LEV is seen at $t^* = 0.24$, and the LEV keeps growing until the end of the stroke. A peak in normal force was found just before $t^* = 0.3$ and the flow topology at this point is sketched in Figure 6.31b. In this Figure a distinct LEV and tip vortex are depicted.

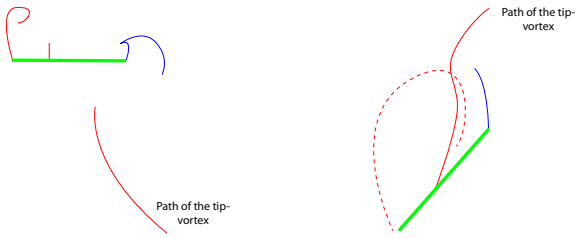

(a) $0.11\,t^*$ (b) $0.43\,t^*$

Figure 6.30: Sketches of the flow visualization features sinusoidal motion with a $10\,\%T$ delayed rotation

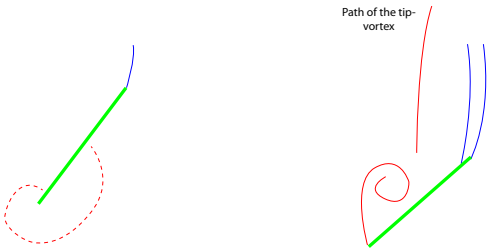

(a) $0.1\,t^*$ (b) $0.3\,t^*$

Figure 6.31: Sketches of the flow visualization features sinusoidal motion with a $10\,\%T$ delayed rotation

The motion is 47 % more effective in the production of thrust compared to the base motion. The increase in thrust comes at the price of a reduction of 20 % in efficiency.

For both motions the flow topology is comparable to the base motions for the advanced rotation case. The time history of the force coefficients has roughly the same shape, only more pronounced. Conversely the delayed rotation cases do not seem to generate high lift mechanisms in the flow and the peaks in the generated force occur at unfavorable orientations of the airfoil. Incorporation of advanced and delayed rotation can increase and decrease thrust significantly, up to 60 % difference in the thrust force with a delay in the rotation of only $10\,\%T$. Hence these mechanisms might be used to generate large forces used for quick maneuvres in exchange for efficiency.

6.4 Effects of Changes in Reduced Frequency

The reduced frequency provides a measure of the unsteadiness associated with a flapping wing [37]. As an expansion of the parameter space the reduced frequency is increased from 0.38 to 0.7.

6.4.1 Force coefficients

In Figure 6.32, the resulting force coefficients are plotted. Here all motions are plotted in the same plot, a plot of each individual motion at a reduced frequency of 0.38 and 0.7 can be found in Appendix C. It can be seen that the thrust coefficient for a reduced frequency of 0.7 is slightly lower in the first half stroke as compared to the values with a reduced frequency of 0.38. However in the second half stroke the thrust is considerably larger, making up entirely for the loss in the first half stroke. That is for all motions the average thrust coefficient (Table 6.9) is larger for the largest reduced frequency. The increase in reduced frequency amounts to an increase in thrust coefficient of 12 to 18%. All the while the figure of merit does not vary significantly. Note that the Sine motion is the only motion for which the figure of merit increases.

The general trends of the base motions do not change, HM1 still produces the largest amount of thrust, followed by HM2 and the sine motion. The sine motions produces the highest measured thrust force coefficient for the highest efficiency at the reduced frequency of $k = 0.7$.

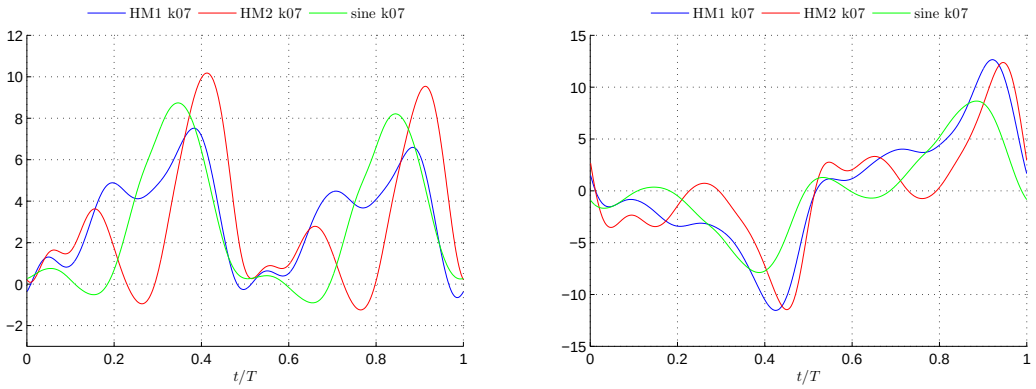

(a) Thrust coefficient (b) Lateral force coefficient

Figure 6.32: Force coefficient for motions with a reduced frequency of 0.7

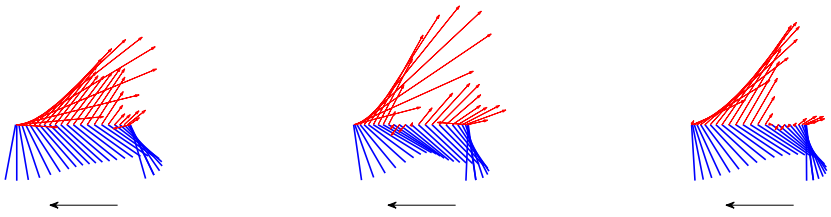

(a) HM1 (b) HM2 (c) Sine

Figure 6.33: Visualization of HM1 at a reduced frequency of 0.7 and the generated forces

Table 6.9: Motion force coefficients

	HM1		HM2		Sine	
	$k = 0.38$	$k = 0.7$	$k = 0.38$	$k = 0.7$	$k = 0.38$	$k = 0.7$
C_T	2.79	3.22	2.64	2.95	2.39	2.81
$\lvert C_{Lateral} \rvert$	3.00	4.61	2.98	3.73	2.39	3.05
M	0.47	0.42	0.48	0.46	0.49	0.51

6.4.2 Dye flow visualization

At the higher reduced frequencies the flow topology is rather similar compared to the base motions.

The stroke for HM1 starts out with the presence of the LEV from the previous stroke, Figure 6.34a. A starting vortex appears at the trailing edge and a small tip vortex is visible at $t^* = 0.09$. The formation of an LEV is estimated to start at $t^* = 0.2$, at this point the tip vortex is clearly visible. From the side view it is deduced that the average spanwise flow from the tip to the three quarter span position is of the order of U_{ref} from $t^* = 0.09$ to 0.3. Spanwise flow was observed at the three quarter span position and the half span position as well.

Figure 6.34c depicts a sketch of the flow at $t^* = 0.46$. The leading edge vortex has grown somewhat larger at this point and the trailing edge dye at half span is further downstream than at the three quarter span position. The tip vortex seems to remain strong up to the very end of the stroke. The TEV formed was formed at approximately $t^* = 0.38$. At stroke reversal, the tip vortex fades out.

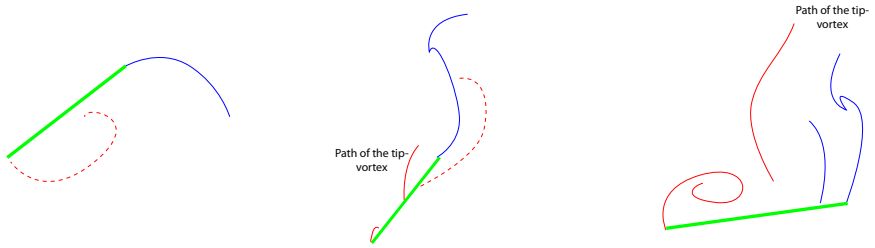

(a) $0.05\,t^*$ (b) $0.2\,t^*$ (c) $0.46\,t^*$

Figure 6.34: Sketches of the flow visualization features HM1 with a reduced frequency of 0.7

HM2 starts with a similar flow picture as its base motion, Figure 6.35c; the presence of a LEV from the previous stroke during the supination is clearly visible. The same holds for the trailing edge vortex originating from the early supination phase, approximately $t^* = -0.12$. The trailing edge vortex is located further downstream at the half span position. A diffusive cloud of red dye is seen between the LEV and TEV, this cloud is the burst LEV formed earlier during the stroke. The wing starts translating faster and a starting vortex forms at the trailing edge. As the stroke progresses a small LEV is formed roughly at $t^* = 0.16$, sketched in Figure 6.35a, and seems to detach at $t^* = 0.3$. At the

start of the supination a trailing edge vortex is formed as the LEV breaks down further. A new LEV is formed at $t^* = 0.45$ due to the rotation of the airfoil.

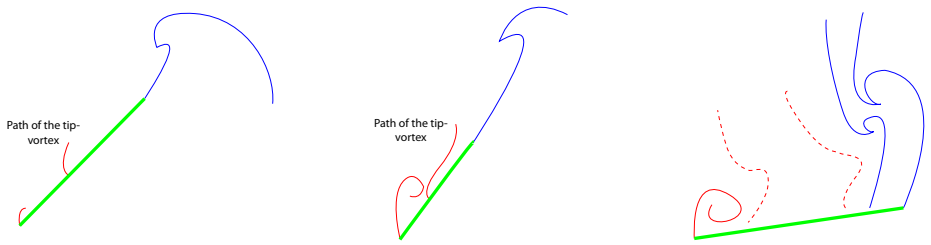

(a) $0.16\,t^*$ (b) $0.26\,t^*$ (c) $0.5\,t^*$

Figure 6.35: Sketches of the flow visualization features HM2 with a reduced frequency of 0.7

The sinusoidal motion has the simplest flow topology with its main features sketched in Figure 6.36. The LEV from the previous stroke is still present at the beginning of the stroke and gets convected downstream as the stroke progresses. A streak line from the tip is visible at $t^* = 0.15$, this could potentially be a tip vortex. Spanwise flow was observed originating at the tip of the airfoil and spreading to a region over half of the span by the end of the stroke. The average spanwise flow from the tip to the quarter span position between $t^* = 0.12$ and 0.38 was measured to be $0.82\,U_{ref}$. The first indications of a LEV in the flow become visible at $t^* = 0.3$. The LEV develops further till end of the stroke, at which point it gets convected downstream.

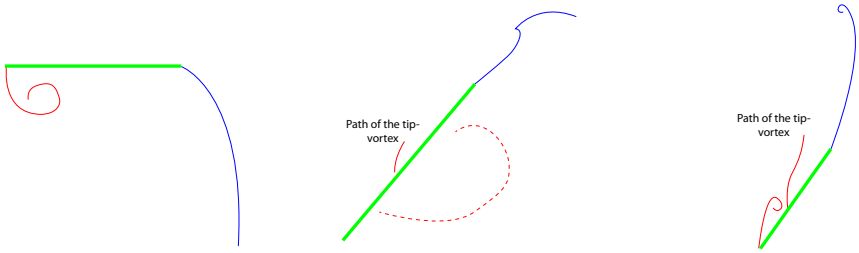

(a) $0.0\,t^*$ (b) $0.15\,t^*$ (c) $0.3\,t^*$

Figure 6.36: Sketches of the flow visualization features sine with a reduced frequency of 0.7

The structure of the wake is fairly simple compared to HM1 and HM2, and can be described as a vortex street with one shed vortex per stroke. As seen from the side view, there seems to be a large contraction of the wake in spanwise direction, it is estimated that the wake is about one chord length high at about four chord lengths downstream from the trailing edge of the airfoil.

Generally at the higher reduced frequency the LEV seems to be closer to the the airfoil compared to the base motion and the vortices seem stronger in strength. In the base motion no distinct tip vortex is observed using the flow visualization technique. Conversely

for the higher reduced frequency cases there are some streak lines originating from the tip that are strong indications of a tip vortex. At stroke reversal the flow moves into its own wake, in these cases, $k = 0.7$, the leading edge vortex seems to keep rotating longer and perhaps until it joins the TEV, as opposed to the LEV stopping rotation almost instantly at stroke reversal. In the base motions the dye cloud originating from the LEV of the previous stroke seems to be stationary.

The spanwise flow is higher, and remains in the same order of magnitude compared to the base motions. The contraction of the wake in spanwise direction is larger compared to the base motions, an indication that higher thrust forces are produced.

The flow field is comparable to that of the base motion. The differences are mainly that the motions are more aggressive and vortices in the flow field interact more with one another since they are around for a longer portion of the period.

Chapter 7

Conclusions and Recommendations

There are a number of ways to convert a flapping motion to a pitch and plunge motion. In this thesis two ways of converting the flapping motion of the Agrius Convolvuli to a pitch-plunge motion are presented and tested. The first motion, HM1, ignores the loss of elevation angle and simply translates the flapping angle into a plunge motion by using a reference speed at 75% of the span and the feathering angle as the pitch angle. The second motion is similar but incorporates a correction for the elevation angle by adding the elevation angle to the feathering angle as an of effective angle of attack. A third motion is a pure sinusoidal motion with the same Reynolds number and reduced frequency, i.e. $4,800$ and 0.38 respectively (cf. Agrius Convolvuli).

7.1 Baseline Bio-Inspired Kinematics

The thrust production and the efficiency of the motion have been measured. For HM1, HM2 and Sine the average thrust coefficients are 2.79, 2.64 and 2.39 respectively. For all motions the force coefficients needed for hover on average are larger than the thrust coefficient of a real moth, but they are of the same order of magnitude. There are several factors increasing the thrust coefficient of the pitch-plunge motion compared to the flapping motion. The speed of the root is non-zero, which leads to a big contribution since here the chord is at its largest. The average speed over the airfoil is larger since it moves in its entirety, rather than just flapping. And last the swept area is larger for the pitch-plunging motion compared to the flapping motion.
7 Hover motion one produces more thrust than hover motion two and the pure sinusoidal motion. The difference between HM1 and HM2 is small, the pure sinusoidal motion produces roughly 14 % less thrust. The force history plots differ strongly from one another, indicating a unique vortical flow evolution for the three cases. Hover motion one produces a more constant thrust coefficient, i.e. compared to the other motions it has a less steep gradient overall. The force history of hover motion two shows two peaks where the force

coefficient is approximately 4. The distinct difference between motion uncorrected for elevation angle, HM1, and the corrected motion, HM2, shows that relatively small changes in the kinematics have a significant influence on the time history of the forces. For the purely sinusoidal motion the force coefficient has a very small peak in the beginning of the stroke and a large peak near $0.3\,t^*$ where the force coefficient is approximately 6. The propulsion efficiencies are all of the same order of magnitude, approximately 0.48, and hence the thrust production of the tested kinematics scales with the energy input.

Using dye flow visualization a general overview of the three dimensional flow topology was recorded. The findings are generally consistent with the detailed account of the PIV data. The dye flow visualization did reveal inboard spanwise flow of the same order of magnitude as the reference velocity.

The PIV data reveals detailed information about the flow evolution. For HM1 there is one leading edge vortex formed during the entire stroke. Per half cycle two TEV's are created, one at the beginning and one right before stroke reversal. The second hover motion, HM2, has a slightly different flow topology. Two LEV's are formed, one at the beginning of the stroke that detaches as the pitching angle increases further, the second one is formed when the pitch angles starts to increase again. Similarly as for HM1 there are two TEV's per half cycle. The sine motion starts out stalled and then forms one large LEV. There is only one TEV, starting vortex, at the beginning of the stroke. Clearly, the vortical flow evolution is unique to all three cases, as is the case for the force history.

The strength of the LEV and TEV correlates strongly with the forces indicating their importance to the force production. The highest correlation factor was found for the purely sinusoidal motion. This is likely related to the lower acceleration terms in the kinematic and thus non circulatory terms become less dominant.

At the three quarter span position, tip effects are more prominent. However at this position there is still a reasonable correlation between vortex strength and the generated forces.

Evidence from comparison with the unsteady aerodynamic vortex model suggests that the wake does not play a dominant role in the force generation for the present kinematics, supported by the fact that the results are insensitive to the vortex core size below a certain threshold value. The relatively good agreement of the forces indicates that spanwise flow, although present, does not affect the magnitude and shape of the force history.

The forces calculated with the high fidelity computation fluid dynamics code are between 82 and 87 % of the force coefficients measured experimentally for the base line kinematics. The shape of the time history of the forces is consistent with the experiment and the differences are small. The origin of the discrepancy can be related to a number of factors. First, the presence of wall and blockage effects in the water channel might increase the forces measured. Second, the resolution of the grid near the LE, TE, and the tip might be insufficient to capture all small scale flow phenomena. Finally, the code treats the flow

as being fully laminar, therefore turbulence effects are not included but may be present in the experiments.

Experiments of the same kinematics for a flapping wing compare well with the pitch-plunge kinematics. The shape of the time history of the forces is in near unison when comparing pitch-plunging and flapping. Conversely the magnitude of the force coefficients for flapping are a factor of two smaller. Since the shape of the time history is similar it is likely that the flow topology will be similar. However, at the moment, it remains to be determined how the flow topology of the flapping experiment compares to the flow topology of the pitch-plunging kinematics.

7.2 Expansion of the Parameter Space

As an expansion of the parameter space, phase lag of plus and minus 10 % of the period is introduced. In the delayed rotation cases there were no high lift vortex mechanisms observed in the flow and the peaks in the force did not occur at a favorable direction for thrust generation. The thrust produced was 60 % less compared to the base line kinematics. Therefore the efficiency of the delayed rotation cases dropped dramatically. The introduction of advanced rotation yields an increase in thrust of 34 to 47 % with a reduction of up to 20 % in efficiency. The flow topology was remarkably similar to the base line kinematics with a slight shift in phase. The application of both advanced and delayed rotation can potentially provide a mechanism to create large differences in forces for maneuverability of flapping wing flyers.

Further expansion of the parameter space was done by increasing the reduced frequency from 0.38 to 0.70. Increasing the reduced frequency yields an increase in thrust of 12 to 18 % with a change in efficiency of -11, -4, and $+4$ % for HM1, HM2 and the sine motion respectively. Note that for the purely harmonic case the efficiency increases with increasing reduced frequency. It might be favorable for roboflyers to design kinematics at higher reduced frequencies for certain kinematics to attain a higher thrust and effciency in hover. Overall similar flow structures to the base line cases were observed in the higher reduced frequency cases.

7.3 Recommendations

The current research serves as an initial attempt to gain a better understanding of the unsteady aerodynamics in flapping hovering flight for bio-inspired motions. The research can be further extended; a number of directions is proposed:

- The difference in time history of the force coefficients between HM1 and HM2 reveals that the elevation angle is a non-negligible variable in the kinematics. The

data gathered in this experimental campaign is not sufficient to make conclusive remarks regarding the extent of the influence of the elevation angle. Further research should thus introduce an extra degree of freedom in the kinematics, incorporating the elevation angle in both flapping and pitch-plunge motions, to gain a better understanding of the implications of the elevation angle.

- The agreement of the shape of the time history of the force coefficients for all motions during the flapping and pitch-plunging experiments leads us to speculate that the underlying lift mechanisms might be similar and the flow might have a similar flow topology on a significant part of the airfoil. Furthermore it is expected that the flapping kinematics will have spanwise flow in the outboard direction. It is highly recommended that the differences and similarities in the flow field are characterized and linked to the force generation.

- The report discusses the expansion of the parameter space in terms of reduced frequency and phase lag. It was found that both affect the forces and the efficiency of the motion. For the expansion of the parameter space vortex strength was not characterized and it remains an open question whether an increase in force generation is linked to the vortex strength or if it is due to an increase in non-circulatory effects, especially in the high reduced frequency case. When clarity is found on this issue it would also be beneficial to investigate the variation of multiple parameters together and characterize the inter-parameter dependency.

- The location of the rotation axis was a constant throughout this experimental campaign. Variations in location of the rotation axis, e.g. from the LE to the quarter chord, can have a high impact on the force generation and the time history of the forces and hence may be interesting for future research.

- Last, for the design of kinematics a thorough understanding of the parameter space is required. In the long term the techniques used in the experiments might be used for rapid testing of a vast number of motions, by reducing the number of cycles for phase averaging and using the similarity between flapping and pitch-plunging. In this way it could be possible to design kinematics that achieve an optimum between generating a large normal force coefficient and orienting the force vector in a favorable orientation to achieve maximum thrust over lateral force.

References

[1] Aquatic insects of central virginia: Flatheaded mayflies (family: Heptageniidae). `http://aquaticinsectsofcentralvirginia.blogspot.com/2011/01/flatheaded-mayflies-family.html`, 2011. Visited on March 3, 2012.

[2] Programmable microfluidics syringe pump, ne-1002x. http://www.syringepump.com/Micro.php, April 2012.

[3] S. A. Ansari, R. Zbikowski, and K. Knowles. Non-linear unsteady aerodynamic model for insect-like flapping wing in hover. part 1: Methodology and analysis. *Proceedings of the I MECH E Part G Journal of Aerospace Engineering*, 220(2):61–83, 2006.

[4] S. A. Ansari, R. Zbikowski, and K. Knowles. Non-linear unsteady aerodynamic model for insect-like flapping wing in hover. part 2: implimentation and validation. *Proceedings of the I MECH E Part G Journal of Aerospace Engineering*, 220(2):169–186, 2006.

[5] S.A. Ansari, R. Zbikowski, and K. Knowles. Aerodynamic modelling of insect-like flapping flight for micro air vehicles. *Progress in Aerospace Sciences*, 42:129–172, September 2006.

[6] Hikaru Aono, Wei Shyy, and Hao Liu. Near wake vortex dynamics of a hovering hawkmoth. *Acta Mech Sin*, 25:23–26, 2009.

[7] Akira Azuma. *Biokinetics of lfying and swimming.* Springer-Verlag, 1992.

[8] Yeon Sik Baik, Jonathan M. Rausch, Luis P. Bernal, and Michael V. Ol. Experimental investigation of pitching and plunging airfoils at reynolds number between 1×10^4 and 6×10^4. *AIAA 2009-4030*, 2009.

[9] Adrian Bejan and James H. Marden. Unifying constructal theory for scaling effects in running, swimming and flying. *The Journal of Experimental Biology*, 209:238–248, 2006.

[10] James M. Birch and Michael H. Dickinson. The influence of wing-wake interaction on the production of aerodynamic forces in flapping flight. *The Journal of Experimental Biology*, 206:2257–2272, 2003.

[11] Richard J. Bomphrey, Nicholas J. Lawson adn Graham K. Taylor, and Adrian L. R. Thomas. Application of digital partical imaga velocimetry to insect aerodynamics: measurement of the leading-edge vortex and near wake of a hawkmoth. *Experiments in Fuids*, 40:546–554, 2006.

[12] Peter K. Burian and Robert Caputo. *Photography Field Guide*. National Geographic, 1999.

[13] Charles P. Ellingtion, Coen van den Berg, Alexander P. Willmott, and Adrian L.R. Thomas. Leading-edge vortices in insect flight. *Nature*, 384:626–630, 1996.

[14] Michael S. Engel and David A. Grimaldi. New light shed on the oldest insect. *Nature*, 427:627–630, 2004.

[15] A. Gogulapati and P. Friedmann. Approximate aerodynamic and aeroelastic modeling of flapping wings in hover and forward flight. *52^{nd} AIAA/ASME/ASCE/AHS/ASC Structures, Structural Dynamics, and Materials Conference*, AIAA 2011-2008, April 2011.

[16] A. Gogulapati, P. Friedmann, and W. Shyy. Non-linear aeroelastic effects in flapping wing micro air vehicles. *49^{th} AIAA/ASME/ASCE/AHS/ASC Structures, Structural Dynamics, and Materials conference*, AIAA 2008-1817, April 2008.

[17] A. Gogulapati, P. Friedmann, and W. Shyy. Approximate aeroelastic analysis of flapping wings in hover. *International Forum for Aeroelasticity and Structural Dynamics*, IFASD 2009-143, June 2009.

[18] Abhijit Gogulapati. *Non-Linear Approximate Aeroelastic Analysis of Flapping Wings in Hover and Forward Flight*. PhD thesis, University of Michigan, 2011.

[19] Kenneth Granlund, Michael Ol, Luis Bernal, and Steve Kast. Experiments on free-to-pivot hover motions of flat plates. *AIAA 2010-4456*, 2010.

[20] David A. Grimaldi and Michael S. Engel. *Evolution of the Insects*. Cambridge University Press, 2005.

[21] S.J. Hulshoff. Ae4-930 aeroelasticity. Faculty of Aerospace Engineering, Delft University of Technology, S.J.Hulshofi.@TUDelft.nl, 2010.

[22] Jr. John D. Anderson. *Fundamentals of Aerodynamics*. McGraw-Hill, fourth edition, 2007.

[23] Barbara Joos. Carbohydrate use in the flight muscles of manduca sexta during pre-flight warm-up. *Journal of Experimental Biology*, 133:317–327, 1987.

[24] Ramji Kamakoti, Siddharth Thakur, Jeffrey Wright, and Wei Shyy. Validation of a new parallel all-speed cfd code in a rule-based framework for multidisciplinary applications. *AIAA 2006-3063*, 2006.

[25] Chang kwon Kang. Chang-kwon kang, postdoctoral research fellow. http://shyylab.engin.umich.edu/people/kang/, April 2012.

[26] H. Liu and H. Aono. Size effects on insect hovering aerodynamics: an integrated computational study. *Bioinspiration & Biomimetics*, 4:015002, 2009.

[27] Hao Liu, Charles P. Ellington, Keiji Kawachi, Coen van den Berg, and Alexander P. Wellmott. A computational fluid dynamic study of hawkmoth hovering. *The Journal of Experimental Biology*, 201:461–477, 1998.

[28] F.J. McClung and R.W. Hellwarth. Giant optical pulsation from ruby. *Journal of Applied Physics*, 33(3):828–829, March 1962.

[29] Barnes W. McCormick. *Aerodynamics, Aeronautics, and Flight Mechanics*. Wiley, 1994.

[30] C. Morrison, C.E.S. Cesnik, Luis P. Bernal, R. Vandenheede, and D. Kumar. Force measurements of a flapping wing with two angular degrees of freedom and bio-inspired kinematics. *AIAA, Submitted for publishing*, 2012.

[31] ERIK J. VAN NIEUKERKEN, LAURI KAILA, IAN J. KITCHING, NIELS P. KRISTENSEN, DAVID C. LEES, JOËL MINET, CHARLES MITTER, MARKO MUTANEN, JEROME C. REGIER, THOMAS J. SIMONSEN, NIKLAS WAHLBERG, SHEN-HORN YEN, and more. Order lepidoptera linnaeus, 1758. in: Zhang, z.-q. (ed.) animal biodiversity: An outline of higher-level classification and survey of taxonomic richness. *Zootaxa*, 3148:212–221, December 2011.

[32] Markus Raffel, Christian E. Willert, Steve T. Wereley, and Jürgen Kompenhans. *Particle Image Velocimetry, A Practical Guide*. Springer, 2007.

[33] Jonathan M. Rausch, Yeon Sik Baik, Luis P. Bernal, Carlos E.S. Cesnik, Wei Shyy, and Michael V. Ol. Fluid dynamics of flapping rigid and spanwise-flexible elliptical flat plates at low reynolds numbers. *AIAA 2010-4739*, 2010.

[34] D. Raymer. *Aircraft Design: A Conceptual Approach*. AIAA, 4th edition, 2006.

[35] G. I. Roth and J. Katz. Five techniques for increasing the speed and accuracy of piv interrogation. *Measurement Science and Technology*, 12:238–245, 2001.

[36] Sanjay P. Sane. The aerodynamics of insect flight. *The Journal of Experimental Biology*, 206:4191–4208, 2003.

[37] W. Shyy, H. Aono, S.K. Chimakurthi, P. Trizila, C.-K Kang, C.E.S. Cesnik, and H. Liu. Recent progress in flapping wing aerodynamics and aeroelasticity. *Progress in Aerospace Sciences*, 46:284–327, 2010.

[38] W. Shyy, Y. Lian, J. Tang, H. Liu, P. Trizila, B. Sanford, L. Bernal, C. Cesnik, P. Friedmann, and P. Ifju. Computational aerodynamics of low reynolds number plunging, pitching and flexible wings for mav applications. *AIAA 2008-0523*, 2008.

[39] Wei Shyy, Yongsheng Lian, Jian Tang, Dragos Viieru, and Hao Liu. *Aerodynamics of low Reynolds number flyers*. Cambridge University Press, 2008.

[40] Wei Shyy and Hao Liu. Flapping wings and aerodynamic lift: The role of leading-edge vortices. *AIAA Journal*, 45(12):2817–2819, December 2007.

[41] Wei Shyy, Pat Trizila, Chang kwon Kang, and Hikaru Aono. Can tip vortices enhance lift of a flapping wing? *AIAA Journal*, 47(2):289–293, February 2009.

[42] Spectra-Physics Lasers. *Pulsed Nd:YAG Laser for Particle Image Velocimetry: Users Manual*, rev. 1 edition, August 1997.

[43] Spectra-Physics Lasers. *Pulsed Nd:YAG Lasers: User's Manual GCR-100/200 series*, revision d edition, June 1997.

[44] Graham K. Taylor, Robert L. Nudds, and Adrian L.R. Thomas. Flying and swimming animals cruise at a strouhal number tuned for high power efficiency. *Nature*, 425:707–711, October 2003.

[45] Henk Tennekes. *The Simple Science of Flight (From Insects to Jumbo Jets)*. MIT Press, Boston, 1996.

[46] Siddharth Thakur and Jeffrey Wright. Loci-stream, all-speed cfd solver for arbitrary polygonal meshes. 2009.

[47] Egbert. Torenbeek. *Synthesis of Subsonic Airplane Design*. Kluwer Academic Publishers, Delft University Press, 1982.

[48] Pat Trizila, Chang kwon Kang, Hikaru Aono, Wei Shyy, and Miguel Visbal. Low-reynolds-number aerodynamics of a flapping rigid flat plate. *AIAA Journal*, 49(4):806–823, April 2011.

[49] J.W.H. Trueman. Evolution of insect wings: a limb exite plus endite model. *Can. J. Zool.*, 68:1333–1335, 1990.

[50] Eric D. Tytell and Charles P. Ellington. How to perform measurements in hovering animal's wake: physical modelling of the vortex wake of the hawkmoth manduca sexta. *Phil. Trans. R. Soc. Lond.*, 358:1559–1566, 2003.

[51] Coen van den Berg and Charles P. Ellingtion. The vortex wake of a 'hovering' model hawkmoth. *Phil. Trans. R. Soc. Lond.*, 352:317–328, 1997.

[52] Hao Wang, Noriyasu Ando, and Ryohei Kanzaki. Active control of free flight manoeuvres in a hawkmoth, agrius convolvuli. *The Journal of Experimental Biology*, 211:423–432, 2008.

[53] Z. Jane Wang. Dissecting insect flight. *Annu. Rev. Fluid Mech.*, 37:183–210, 2005.

[54] Weis-Fogh. Quick estimates of flight fitness in hovering animals, including novel mechanisms for lift production. *The Journal of Experimental Biology*, 59:169–230, 1973.

[55] C.E. Willert and M. Gharib. Digital particle image velocimetry. *Experiments in Fuids*, 10:181–193, 1991.

[56] Alexander P. Willmott and Charles P. Ellingtion. The mechanics of flight in the hawkmoth manduca sexta. *The Journal of Experimental Biology*, 200:2705–2722, 1997.

[57] Derrick Yeo, Ella M. Atkins, Luis P. Bernal, and Wei Shyy. Experimental investigation of the pressure, force, and torque characteristics of a rigid flapping wing. *AIAA, Submitted for publishing*, 2012.

Appendix A

Flow Visualization

The dye flow visualization produces diffused images that can be hard to interpret therefore sketches of the most prominent flow features have been used in this report. Below a comparison of the original still images and the sketches is provided.

(a) Still image at $t^* = 0.17$ (b) Still image at $t^* = 0.3$ (c) Still image at $t^* = 0.45$

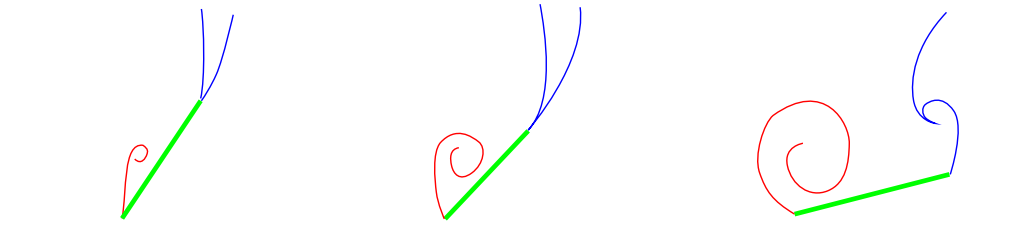

(d) Sketch of the most prominent flow features at $t^* = 0.17$ (e) Sketch of the most prominent flow features at $t^* = 0.3$ (f) Sketch of the most prominent flow features at $t^* = 0.45$

Figure A.1: Comparison of the still images and the sketches of the most prominent features observed in the flow visualization, hover motion 1

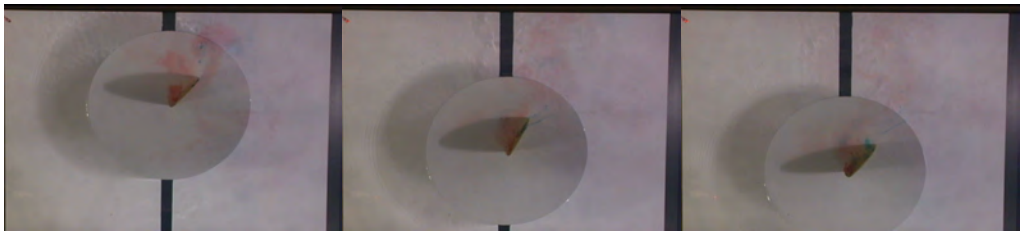

(a) Still image at $t^* = 0.20$ (b) Still image at $t^* = 0.34$ (c) Still image at $t^* = 0.42$

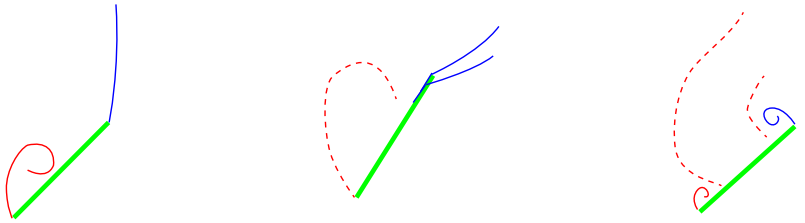

(d) Sketch of the most prominent flow features at $t^* = 0.20$ (e) Sketch of the most prominent flow features at $t^* = 0.34$ (f) Sketch of the most prominent flow features at $t^* = 0.42$

Figure A.2: Comparison of the still images and the sketches of the most prominent features observed in the flow visualization, hover motion 2

(a) Still image at $t^* = 0.14$ (b) Still image at $t^* = 0.3$

(c) Sketch of the most prominent flow features at $t^* = 0.14$ (d) Sketch of the most prominent flow features at $t^* = 0.3$

Figure A.3: Comparison of the still images and the sketches of the most prominent features observed in the flow visualization, pure sinusoidal motion

(a) Still image at $0.14\,t^*$ (b) Still image at $0.42\,t^*$

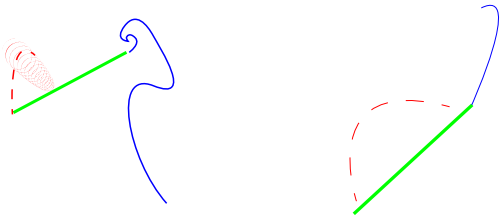

(c) Sketch of the most prominent flow features at $0.14\,t^*$ (d) Sketch of the most prominent flow features at $0.42\,t^*$

Figure A.4: Comparison of the still images and the sketches of the flow visualization features HM1 with a $10\,\%T$ delayed rotation

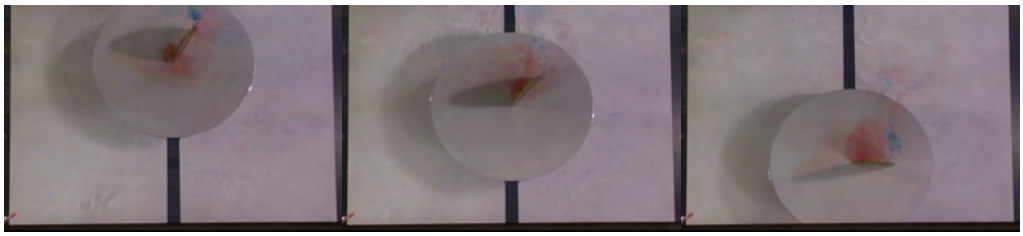

(a) Still image at $0.07\,t^*$ (b) Still image at $0.2\,t^*$ (c) Still image at $0.38\,t^*$

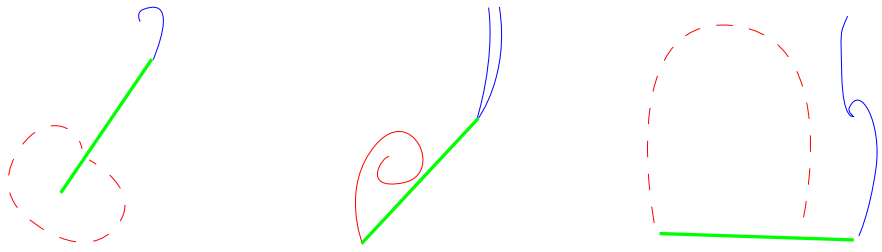

(d) Sketch of the most prominent flow features at $0.07\,t^*$ (e) Sketch of the most prominent flow features at $0.2\,t^*$ (f) Sketch of the most prominent flow features at $0.38\,t^*$

Figure A.5: Comparison of the still images and the sketches of the flow visualization features HM1 with a $10\,\%T$ advanced rotation

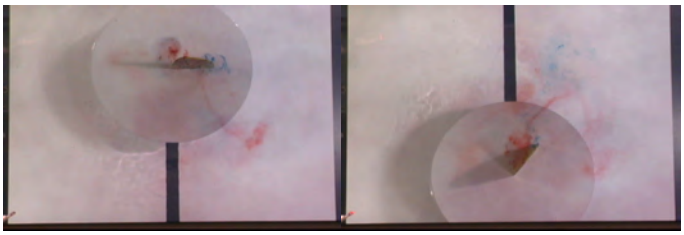

(a) Still image at $0.11\,t^*$ (b) Still image at $0.43\,t^*$

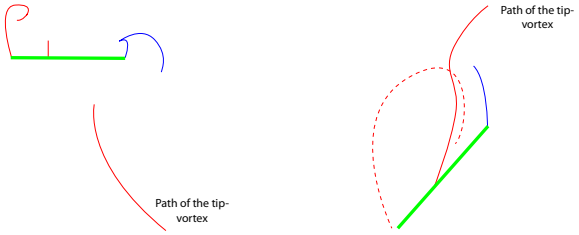

(c) Sketch of the most prominent flow features at $0.11\,t^*$ (d) Sketch of the most prominent flow features at $0.43\,t^*$

Figure A.6: Comparison of the still images and the sketches of the flow visualization features sinusoidal motion with a $10\,\%T$ delayed rotation

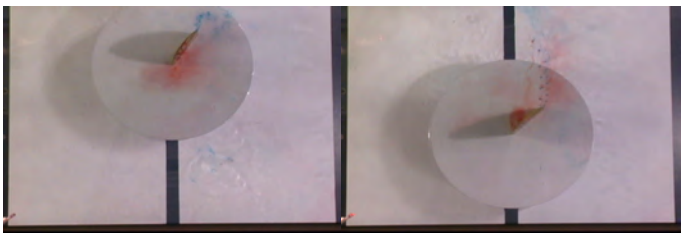

(a) Still image at $0.1\,t^*$ (b) Still image at $0.3\,t^*$

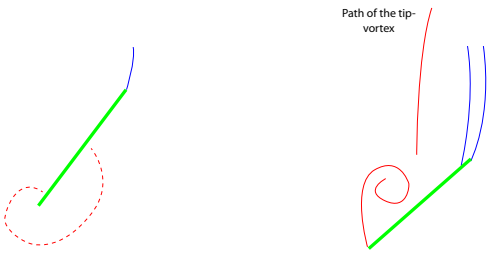

(c) Sketch of the most prominent flow features at $0.1\,t^*$ (d) Sketch of the most prominent flow features at $0.3\,t^*$

Figure A.7: Comparison of the still images and the sketches of the flow visualization features sinusoidal motion with a $10\,\%T$ delayed rotation

(a) Still image at $0.05\,t^*$ (b) Still image at $0.2\,t^*$ (c) Still image at $0.46\,t^*$

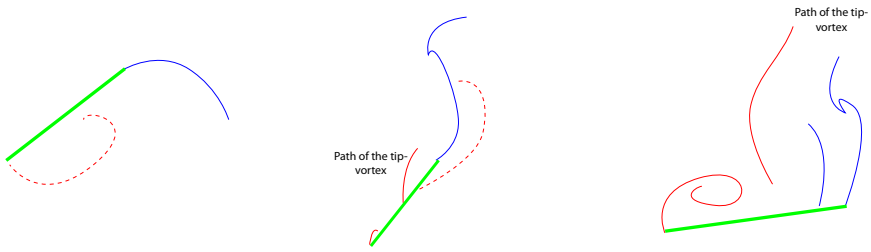

(d) Sketch of the most prominent flow features at $0.05\,t^*$ (e) Sketch of the most prominent flow features at $0.2\,t^*$ (f) Sketch of the most prominent flow features at $0.46\,t^*$

Figure A.8: Comparison of the still images and the sketches of the flow visualization features HM1 with a reduced frequency of 0.7

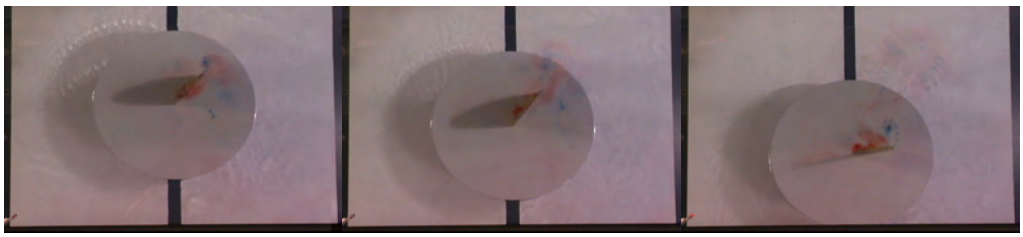

(a) Still image at $0.16\,t^*$ (b) Still image at $0.26\,t^*$ (c) Still image at $0.5\,t^*$

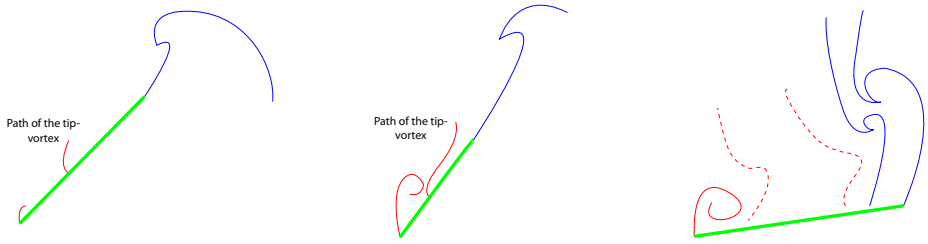

(d) Sketch of the most prominent flow features at $0.16\,t^*$ (e) Sketch of the most prominent flow features at $0.26\,t^*$ (f) Sketch of the most prominent flow features at $0.5\,t^*$

Figure A.9: Comparison of the still images and the sketches of the flow visualization features HM2 with a reduced frequency of 0.7

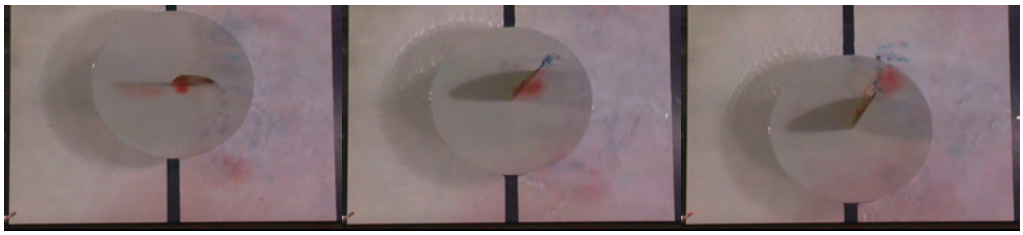

(a) Still image at $0.0\,t^*$ (b) Still image at $0.15\,t^*$ (c) Still image at $0.3\,t^*$

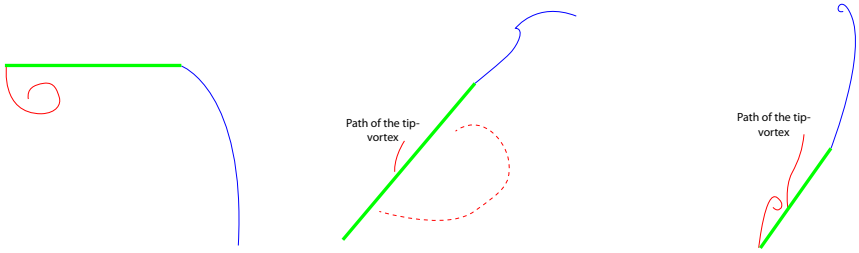

(d) Sketch of the most prominent flow features at $0.0\,t^*$ (e) Sketch of the most prominent flow features at $0.15\,t^*$ (f) Sketch of the most prominent flow features at $0.3\,t^*$

Figure A.10: Comparison of the still images and the sketches of the flow visualization features sine with a reduced frequency of 0.7

Appendix B

Particle Image Velocimetry

Streamlines provide a good representation of the flow structure, but are lacking by not visualizing the magnitude of the flow velocity. In this appendix the flow velocities are depicted on lines parallel to the airfoil motion at multiple locations.

Note that the magnitude of the vectors is only to scale with the other vectors in the same plot. To give an estimate of the magnitude the maximum velocity for each vertical line of vectors is given at the bottom of each plot. The maximum measured velocity is normalized by the reference velocity, as depicted in equation B.1.

$$\bar{v} = \frac{v}{U_{ref}} \tag{B.1}$$

The axes in all plots show the distance in mean chords, with zero being the position of the leading edge at half span and the mid position of the plunge motion. Note that the chord length at half span is larger than the mean chord length. The plots are ordered chronologically from left to right, top to bottom. In all figures the airfoil is plunging downwards or the plunge velocity is zero and the leading edge points to the left side of the figure.

In the plots we observe that the velocity can reach magnitudes up to $2.5\,U_{ref}$. There is clearly a flow created by the airfoil in downstream direction, i.e. thrust is produced.

B.1 Velocity Plots Hover Motion One

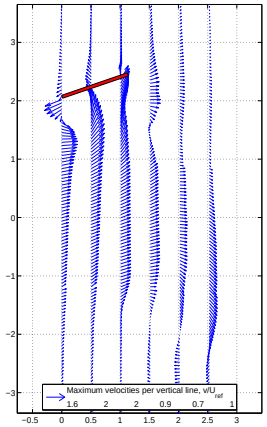

(a) $t^* = 0.0$, $C_T = 0.47$, $C_{Lat} = -1.39$

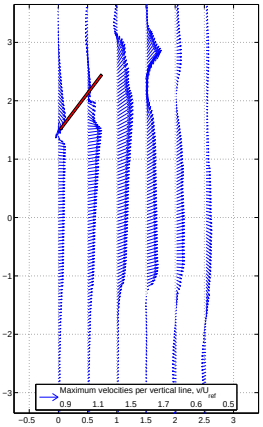

(b) $t^* = 0.1$, $C_T = 2.68$, $C_{Lat} = -2.11$

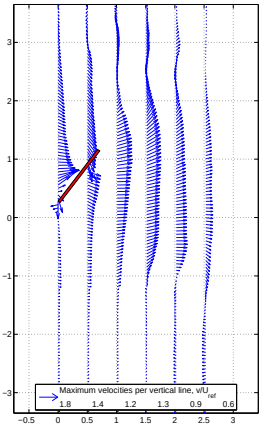

(c) $t^* = 0.2$, $C_T = 4.90$, $C_{Lat} = -3.30$

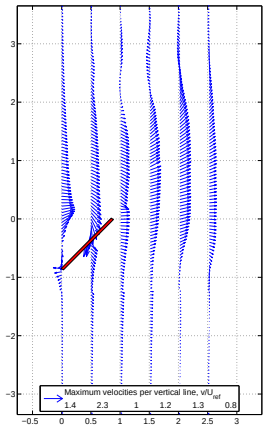

(d) $t^* = 0.3$, $C_T = 3.82$, $C_{Lat} = -3.16$

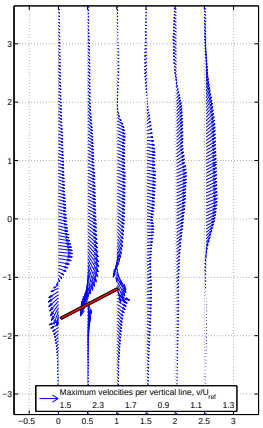

(e) $t^* = 0.4$, $C_T = 3.11$, $C_{Lat} = -4.82$

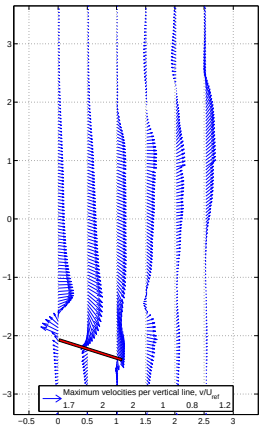

(f) $t^* = 0.5$, $C_T = 0.27$, $C_{Lat} = -1.47$

Figure B.1: Velocity plots HM1 base at half span for various phases, $C_T = 2.79$ and $|C_{Lat}| = 3.00$

B.2 Velocity Plots Hover Motion Two

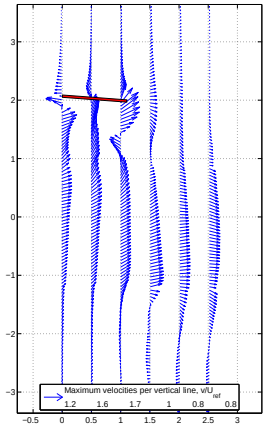

(a) $t^* = 0.0$, $C_T = -0.03$, $C_{Lat} = -1.64$

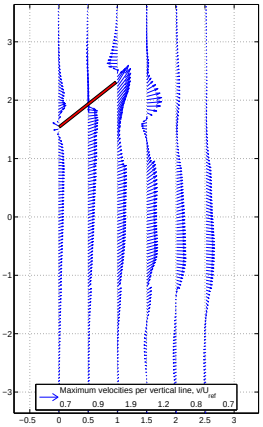

(b) $t^* = 0.1$, $C_T = 3.70$, $C_{Lat} = -4.23$

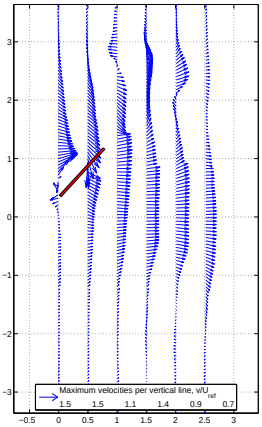

(c) $t^* = 0.2$, $C_T = 3.29$, $C_{Lat} = -2.76$

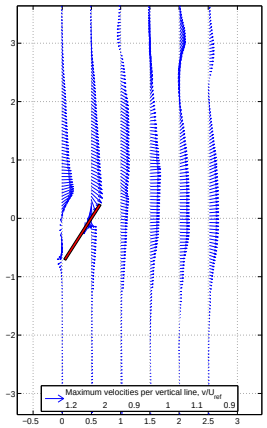

(d) $t^* = 0.3$, $C_T = 2.61$, $C_{Lat} = -1.46$

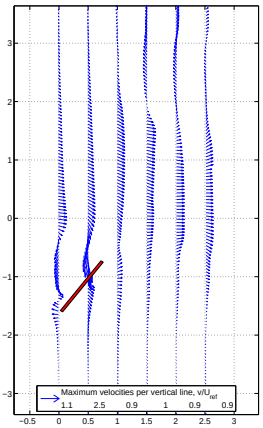

(e) $t^* = 0.4$, $C_T = 4.76$, $C_{Lat} = -3.57$

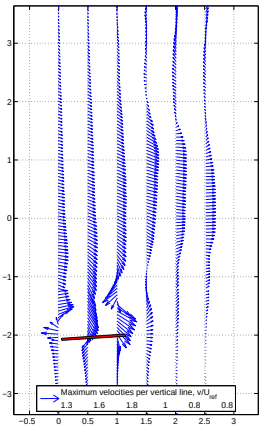

(f) $t^* = 0.5$, $C_T = -0.06$, $C_{Lat} = 1.43$

Figure B.2: Velocity HM2 base at half span for various phases, $C_T = 2.64$ and $|C_{Lat}| = 2.98$

B.3 Velocity Plots Purely Sinusoidal Motion

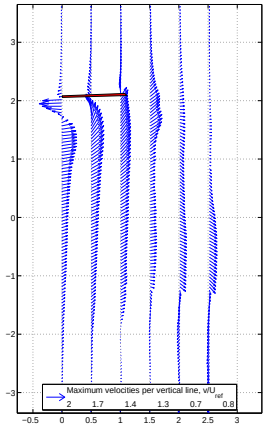

(a) $t^* = 0.0$, $C_T = 0.18$, $C_{Lat} = -1.19$

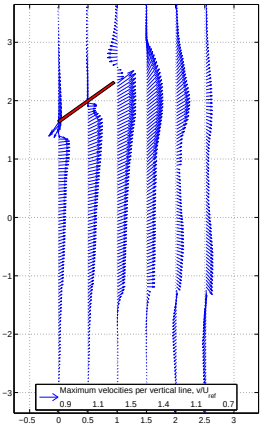

(b) $t^* = 0.1$, $C_T = 1.16$, $C_{Lat} = -1.50$

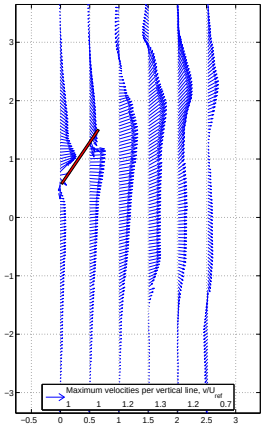

(c) $t^* = 0.2$, $C_T = 2.90$, $C_{Lat} = -1.82$

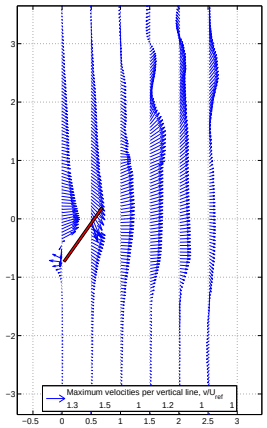

(d) $t^* = 0.3$, $C_T = 6.06$, $C_{Lat} = -3.58$

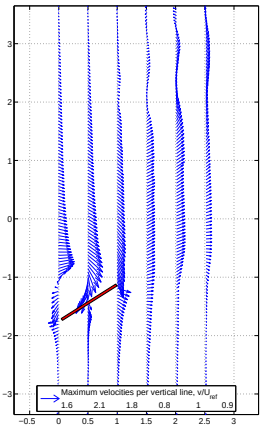

(e) $t^* = 0.4$, $C_T = 2.75$, $C_{Lat} = -3.26$

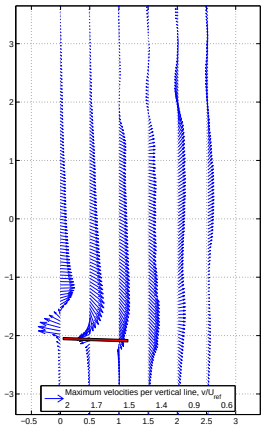

(f) $t^* = 0.5$, $C_T = 0.16$, $C_{Lat} = 1.51$

Figure B.3: Velocity plots Sine base at half span for various phases, $C_T = 2.39$ and $|C_{Lat}| = 2.39$

Appendix C

Hover motions with increased reduced frequency

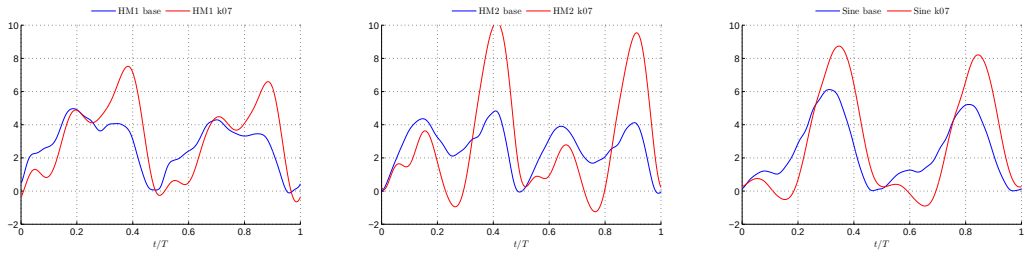

(a) Thrust coefficients HM1 (b) Thrust coefficients HM2 (c) Thrust coefficients Sine

(d) Lateral force coefficients HM1 (e) Lateral force coefficients HM2 (f) Lateral force coefficients Sine

Figure C.1: Hover motion with varying reduced frequency force coefficients